2008

Tribological behavior of hydrogenated and non-hydrogenated diamond-like carbon coatings in dry and lubricated sliding

Ahmed Abougharam
University of Windsor

TRIBOLOGICAL BEHAVIOUR OF HYDROGENATED AND NON-HYDROGENATED DIAMOND-LIKE CARBON COATINGS IN DRY AND LUBRICATED SLIDING

By

AHMED ABOUGHARAM

A Thesis
Submitted to the Faculty of Graduate Studies
through Engineering Materials
in Partial Fulfillment of the Requirements for
the Degree of Master of Applied Science at the
University of Windsor

Windsor, Ontario, Canada

2008

Your file Votre référence
ISBN: 978-0-494-47035-0
Our file Notre référence
ISBN: 978-0-494-47035-0

Author's Declaration of Originality

I hereby certify that I am the sole author of this thesis and that no part of this thesis has been published or submitted for publication.

I certify that, to the best of my knowledge, my thesis does not infringe upon anyone's copyright nor violate any proprietary rights and that any ideas, techniques, quotations, or any other material from the work of other people included in my thesis, published or otherwise, are fully acknowledged in accordance with the standard referencing practices. Furthermore, to the extent that I have included copyrighted material that surpasses the bounds of fair dealing within the meaning of the Canada Copyright Act, I certify that I have obtained a written permission from the copyright owner(s) to include such material(s) in my thesis and have included copies of such copyright clearances to my appendix.

I declare that this is a true copy of my thesis, including any final revisions, as approved by my thesis committee and the Graduate Studies office, and that this thesis has not been submitted for a higher degree to any other University of Institution.

ABSTRACT

Friction and material transfer mechanisms during sliding between 319 Al pin and hydrogenated diamond-like carbon (H-DLC) and non-hydrogenated diamond-like carbon (NH-DLC) coatings were investigated under ambient, humid air and vacuum. The coefficients of friction (COF) of H-DLC and NH-DLC were governed by the formation of carbon rich layers on the counterface.

H-DLC produced a lower COF of 0.05 in dry sliding compared to 0.1 in boundary lubricated sliding, indicating that this coating is more effective without the addition of lubricants. During lubricated sliding testes against AISI 52100 steel NH-DLC produced a lower COF compared to H-DLC and induced an earlier transition from the boundary to the mixed lubrication regime. This early transition was a result of the NH-DLC wearing down the steel counterface and increasing the contact area, prompting a reduction in contact pressure.

DEDICATION

I dedicate this work to my family, specially my father, Abdel Monem, who encouraged me and got me to where I am today. Also my mother, Safaa, who listened to me and gave me the motivation, energy and enthusiasm I needed to do this study. Last but not least my brothers, Mostafa and Ibrahim who stood beside me and supported me in tough times when I needed them the most. Finally, I dedicate this work to my grandparents Abdel Galel and Omo-saed, who passed away before I got the chance to know them, and my other grandparents, Mohy and Zenab, who helped raising me as a child, which brought me to be the man I am today.

ACKNOWLEDGMENTS

I would like to specially thank and acknowledge Dr. Alpas, for giving me the opportunity to do this study under his supervision. Thank you for your support and encouragement throughout my studies at the University of Windsor. In addition, I would like to thank my committee members Dr. Edrisy and Dr. Sid-Ahmed for their valuable suggestions.

I would also like to acknowledge and thank Dr. Lev and Dr. Lukitsch of GM Global Research and Development Center for their support and the share of their expertise and knowledge. I am also grateful to Dr. Perry, Dr. Qi and Dr. Cheng of GM Global Research and Development Center for the valuable discussions and help at various stages of this study. I also would like to thank GM Global Research and Development Center staff for their assistance and support. I thank Bob Kubic and Curtis Wong for their assistance with SEM, Deborah Eckel for conducting infrared analysis, Rick Waldo for conducting electron microprobe analyses and Robert Paluch for his help with the metallography and sample preparation.

I also would like to acknowledge the support and assistance of all faculty and staff of the University of Windsor. Thanks to Mrs. Barbara Denomey and Ms. Rosemarie Gignac for their administrative assistance. I also would like to thank all my fellow graduate students of GM industrial research chair research group, especially Dr. Konca, Dr. Akarca, Mr. Dey, Mrs. Das , Mr. Bhowmick, Mr. Shafiei, Mrs. Chen, Mr. Sen and Mr. Ronholm, my lab partner in my first graduate course for their help and friendship. Finally, I thank my family and friends for their encouragement and support.

TABLE OF CONTENTS

INDEX OF FIGURES

Figure No. **Page**

INDEX OF TABLES

Table No. **Page**

NOMENCLATURE

ATF	Automatic transmission fluid
AISI	American Iron and Steel Institute
BL	Boundary lubrication
COF	Coefficient of friction
CVD	Chemical vapor deposition
DLC	Diamond like carbon
EDM	Electrical discharge machining
EDS	Energy dispersive spectroscopy
EHL	Elasto-hydrodynamic lubrication
ELF	Electron localization function
EMPA	Electron micro probe analyses
EP	Extreme pressure
ERD	Elastic recoil detection
FM	Friction modifiers
FTIR	Fourier transform infrared spectroscopy
H-DLC	Hydrogenated diamond-like carbon
HL	Hydrodynamic lubrication
LFR	Low friction regime
M	Mineral oil
NH-DLC	Non-hydrogenated diamond-like carbon
PSI	Phase shift interference
PVD	Physical vapor deposition

RGA	Residual gas analyzer
RH	Relative humidity
SEM	Scanning electron microscope
ULF	Ultra low friction
VSI	Vertical shift interference
XRD	X-Ray diffraction

LIST OF SYMBOLS

A	Total area at the interface
E	Elastic modulus
E'	Composite elastic modulus
E_{12}^{tot}	Total energy of the interface
E_i^{tot}	Total energy of material i
F	Load applied
G	Dimensionless material parameter
H	Hardness
h_{min}	Oil film thickness
k	Ellipticity parameter
R_x	Radius of curvature of the bearing in the x-direction
R_y	Radius of curvature of the bearing in the y-direction
R_{q1}	Roughness of surface *1*
R_{q2}	Roughness of surface *2*
U	Dimensionless speed parameter
V	Speed
W	Dimensionless load parameter
W_{sep}	Work of separation
α	Pressure viscosity coefficient
β	Wetting angle
γ_{LV}	Surface energy between the liquid (L) vapour (V) interfaces

γ_{SL} Surface energy between the solid (S) liquid (L) interfaces

γ_{SV} Surface energy between the solid (S) vapour (V) interfaces

η Oil viscosity

λ Lambda ratio

ν Poisons ratio

σ^* Root mean squares of the surface roughness

σ_{12} Energy of the interface between material *1* and *2*

σ_{iv} Surface energy of the material *i*

CHAPTER 1

Introduction

Tribology, or the effect of friction and wear on moving components, has been a topic of interest since the dawn of civilization when humans discovered that generating friction between a wooden stick and a wooden plank produced enough heat to start a fire. An understanding of friction phenomena developed with the Sumerians and Egyptians who first used lubricants to move heavy objects efficiently. As civilizations advanced, so did their tools, and in this day and age, difficult tasks like metal forming, machining and drilling have been made possible with the help of tools and machines. Limited resources and high demand have made tool life and machine performance the current issues, and innovative technology has lead to hard surface coatings, such as TiN and CrN, which protect surfaces against wear and corrosion and extend tool life. In some applications, however, (such as the dry machining of aluminum) a low friction, non-stick surface is required to prevent the chip build up that typically leads to failure. Studies prove that aluminum has a low tendency of adhesion towards diamond-like carbon (DLC) coatings, so it follows that their use would prevent chip build up and extend tool life [1] [2].

DLC coatings were first introduced back in 1953 when Schmellenmeier produced the first DLC coating with unusual and unique low friction (reaching 0.001) and low wear rates (below $1x10^{-10}$ mm^3/Nm when hydrogenated DLC coatings are tested in high vacuum) [3], [4], [5]. These characteristics made DLC coatings suitable for addressing a wide range of applications, from space and medical devices to car engine parts and razor blades [3]. Also their mechanical properties (hardness reaching up to 90 GPa) allows the

coating to withstand high loading conditions and protect the substrate, qualifying them for tool and die applications. In addition, DLC's chemical inertness, offers substrate protection against oxidation and corrosion making it ideal for the food processing industry [6].

1.1 DLC in Dry Sliding

Studies have shown that the DLC coatings applied in dry-sliding are very sensitive to the environment, producing a wide range of COF, spanning (from 0.001 to 0.7) [3]. This broad range is due to the combination of DLC mechanical and chemical properties. For instance, 319 Al sliding against NH-DLC in ambient air (25 %RH) found to produce a COF of 0.1 [7], but when humidity in the air increased to 90% RH, the COF of a Al_2O_3 ball sliding against NH-DLC decreases to 0.05 [8]. Conversely, testing NH-DLC in vacuum or inert atmosphere produced a high COF of 0.6, while, Al_2O_2/TiC sliding against H-DLC produced a very low COF of 0.01 when tested in ultra high vacuum [9]. It follows that humidity and hydrogen content play an important role in reducing friction for NH-DLC and H-DLC, and studies have shown that very low friction can be achieved for NH-DLC in vacuum (similar to H-DLC). It was found that running 319 Al against NH-DLC in ambient air initially generated a COF of 0.1. When the chamber was evacuated, a very low COF of 0.01 was produced, unlike the COF of 0.6 when NH-DLC was tested in vacuum, without an initial running-in in ambient air [7]. However, it remains unclear what precisely is happening at the sliding interface, which causes this intriguing tribological behaviour.

1.2 DLC in Lubricated Sliding

Three friction regimes are observed during lubricated sliding: hydrodynamic, elasto-hydrodynamic and boundary lubrication regimes [10]. In hydrodynamic and elasto-hydrodynamic lubrication regimes, the lubricant carries most of the applied load, creating an easily sheared medium that separats the sliding surfaces. As for the boundary regime, high loads and low speeds result in the formation of a very thin lubricating film on the mating surfaces. Consequently, a considerable amount of contact occurs between the asperities, leading to higher COF relative to the values produced at the hydrodynamic and elasto-hydrodynamic lubrication regimes.

Various studies have explored the effects of coating the surface with DLC to lower the friction at the asperity junctions and reduce the total COF under boundary lubrication. Other studies have examined the effect of additives and oil chemistry on the friction of DLC under boundary lubrication. How DLC will behave in a fully formulated oil, specifically automatic transmission fluid (ATF), remains unclear.

1.3 Objective and Scope of the Study

1) Investigate the tribological behaviour of 319 Al sliding against both NH-DLC and H-DLC coatings to improve and optimize the drilling and machining of 319 Al, which is a common aluminum alloy used in the automotive industry for its potential in the development of engine blocks.
2) Examine the friction behaviour of AISI 52100-grade steel sliding against both NH-DLC and H-DLC coatings under boundary lubrication (BL) in the presence of ATF. This part of the study will enhance our understanding of BL in the presence of surface coatings to determine whether it would be beneficial to coat

transmission components made of AISI 52100-grade steel, such as planetary gears to lower the COF under BL.

1.4 Thesis Organization

Chapter 2 provides a literature survey on what is DLC and how it is commonly produced. Chapter 2 also explores previous studies conducted on the tribological behaviour of DLC coatings that investigate the effects of hydrogen content, humidity, inert atmosphere and temperature on DLC friction and wear. The literature survey will cover the different lubrication regimes, oil based lubricants and information about the tribological behaviour of DLC under lubricated conditions that has resulted from other studies.

Chapter 3 describes the materials used in this study, along with the experimental procedures that were carried out to characterize the DLC coatings as well as test friction and wear in dry and lubricated conditions. Chapters 4: Part I and Part II present the experimental results along with discussions of the dry and lubricated sliding of DLC coatings, respectively. Finally, Chapter 5 summarizes and outlines the study's conclusions and recommendations for future work.

CHAPTER 2

Literature Survey

Diamond-like carbon (DLC) is a metastable amorphous form of carbon whose excellent tribological behaviour has attracted many industries and has been incorporated into applications like medical devices, hard discs and automobile engine components [6]. This chapter provides a literature survey of past studies that have contributed to our understanding of the tribological behaviour of DLC coatings under various conditions, such as a hydrogen atmosphere, humidity, vacuum, high temperature and lubricated contacts.

2.1 Diamond-like Carbon Coatings

DLC coatings consist of two main types; the first is amorphous carbon (a-C) with an sp^2 hybridized bonding structure (Figure 2-1) and a hardness ranging between 15 and 50 GPa [6]. The second type is tetrahedral amorphous carbon (ta-C), where the carbon atom is surrounded by four atoms at the corners of the tetrahedron, forming a sp^3 hybridized diamond-like structure with strong σ bonds connecting the neighboring atoms (Figure 2-1). The resulting coating exhibits high hardness ranging from 30 to 80 GPa, due to its strong, diamond-like structure [6].

Both DLC types, ta-C and a-C, can be alloyed with hydrogen, to create a hydrogenated, tetrahedral amorphous carbon (ta-C:H) or a hydrogenated, amorphous carbon (a-C:H). Figure 2-2 is a schematic diagram, representing DLC coatings with respect to sp^3, sp^2 and hydrogen that illustrate where DLC coatings fall compared to

diamond (sp^3) and graphite (sp^2). The typical chemical and mechanical properties of DLC coatings are presented in Table 2-1.

From here on, amorphous carbon and hydrogenated amorphous carbon will be referred to as NH-DLC and H-DLC respectively.

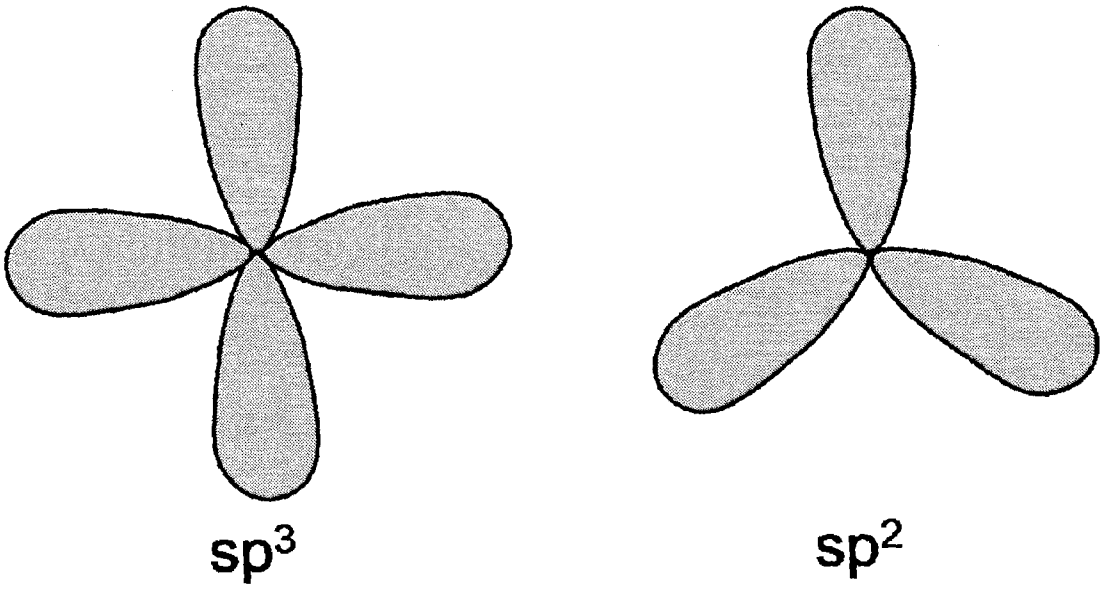

Figure 2-1: Schematic for sp^2 and sp^3 hybridized bonding structures

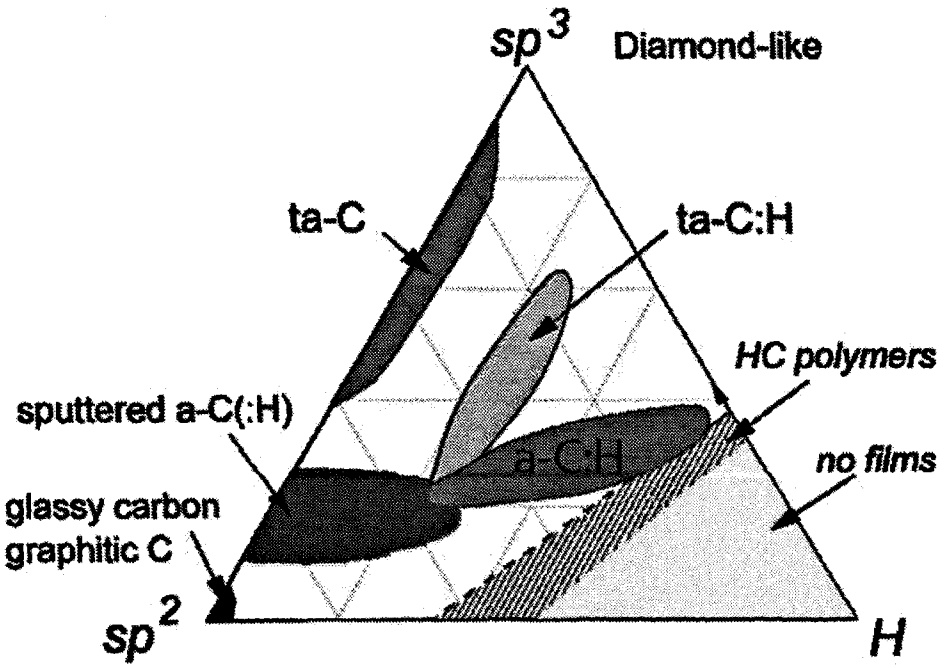

Figure 2-2: Schematic for different forms of amorphous carbon [11]

Table 2-1: Typical mechanical and chemical properties of various types of DLC coatings [3][6]

Property	a-C	a-CH	ta-C
sp^3 content %	5-25	40	80
Hydrogen Content (at%)	0	20-60	<5
Hardness (GPa)	15-50	10-20	<80

2.2 Deposition of DLC

2.2.1 Chemical Vapour Deposition

Chemical vapor deposition (CVD) deposits solid coatings on substrates using chemical reactions with rates ranging from 1 to 40 μm/h. During deposition, the substrate is heated to temperatures up to 850°C, then the precursor gas and a carrier gas, such as hydrogen and argon, are introduced into the reactor as shown schematically in Figure 2-3. The precursor molecules then adsorb or react with the substrate, forming a protective coating on the surface of the substrate. Carrier gases such as nitrogen or argon ensure even mixing of the reactant gases for uniform deposition. They also helps maintain the deposition rate by providing an ample total flow rate through the reactor and by suppressing the nucleation in the gas phase [12].

However, CVD has limitations; high operating temperatures may deform or change substrate properties, so radio-frequency glow discharge or plasma is combined with CVD to allowing the deposition process to operate at lower temperatures (e.g. 150°C). This technique is referred to as plasma assisted (PA) or plasma enhanced (PE) CVD (Figure 2-3). There are two types of plasma sources; direct-current (DC) and alternating-current (AC) or radio-frequency (RF). Plasma is generated by applying a current through electrodes, where the precursor gas is ionized. Since plasma generation by DC depends on the substrate being one of the electrodes, depositing insulating

coatings diminishes the plasma, so insulating coatings utilizes RF, which applies an AC between the electrodes and the conductive walls of the chamber to maintaining the plasma.

DLC coatings are commonly deposited at low temperatures, because DLC coatings have a low tolerance for high temperatures and often require a PACVD technique. A wide range of hydrocarbons can be used as precursor gasses (methane, butane and propane), which are dissociated by the plasma to form radicals that are deposited onto the substrate. The hydrogen content of the DLC coating depends on the ratio of H/C in the hydrocarbon precursor gas [22], which will be described in Section 2.4.2.

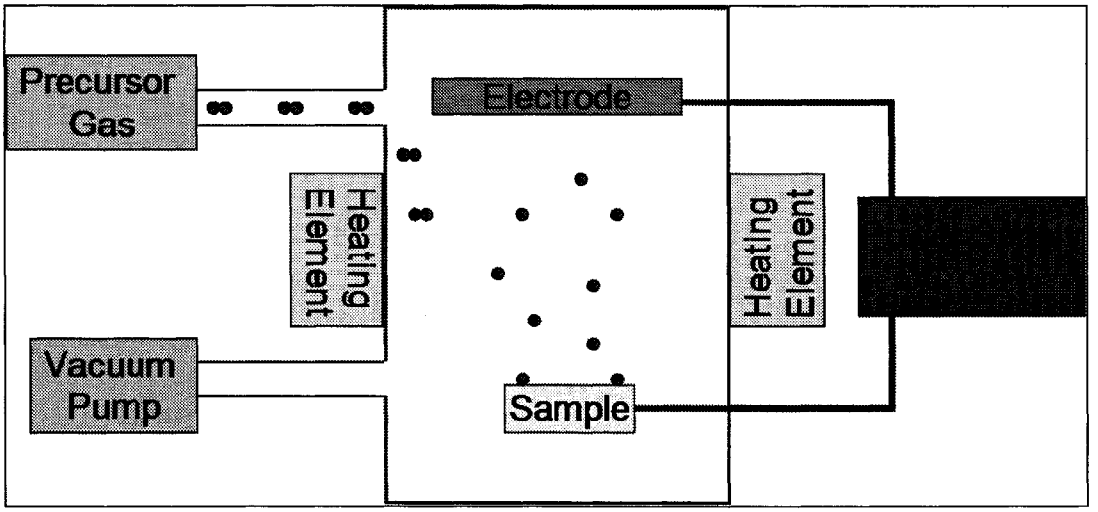

Figure 2-3: Schematic for CVD system

2.2.2 Physical Vapour Deposition

There are three processes that fall under the term physical vapour deposition (PVD); these are i) evaporation, ii) sputtering and iii) ion plating, shown in Figure 2-4. In all these processes, the target/source is evaporated and deposited on the substrate at rates ranging between 0.5 and 5 μm/h. In the evaporation process, coatings are deposited by

condensation of vapour. However, in Sputtering technique, argon glow discharge, in other words, plasma is generated in front of the target, ionized argon collide with the target at 100-1000 eV, ejecting atoms from the target. The ejected atoms then accelerate towards the substrate with a kinetic energy of 10-40 eV, much higher than that of the evaporated atoms (0.2-0.3 eV), forming a stronger adhesion to the surface. As for ion plating, the plasma is formed in front of the substrate, so that it is bombarded by argon. Meanwhile, coating atoms evaporate (by resistance, electron beam heating or arc evaporation) and enter the plasma, which is the deposited on the substrate [12].

A fourth PVD technique called closed field unbalanced magnetron sputtering (Figure 2-5) is utilized by the industry to mainly produce DLC coatings. This technique, magnetrons of opposite polarity are arranged adjacent to each other, producing a closed magnetic flux. In addition, the magnetrons are unbalanced, meaning that one magnetic pole is stronger than the other to expand the plasma. This unique setup traps all electrons, thus increasing ion bombardment of the substrate, which improve deposition efficiency [13]. High internal stresses and poor adhesion remain problematic with DLC coatings, however, and are investigated in the next section.

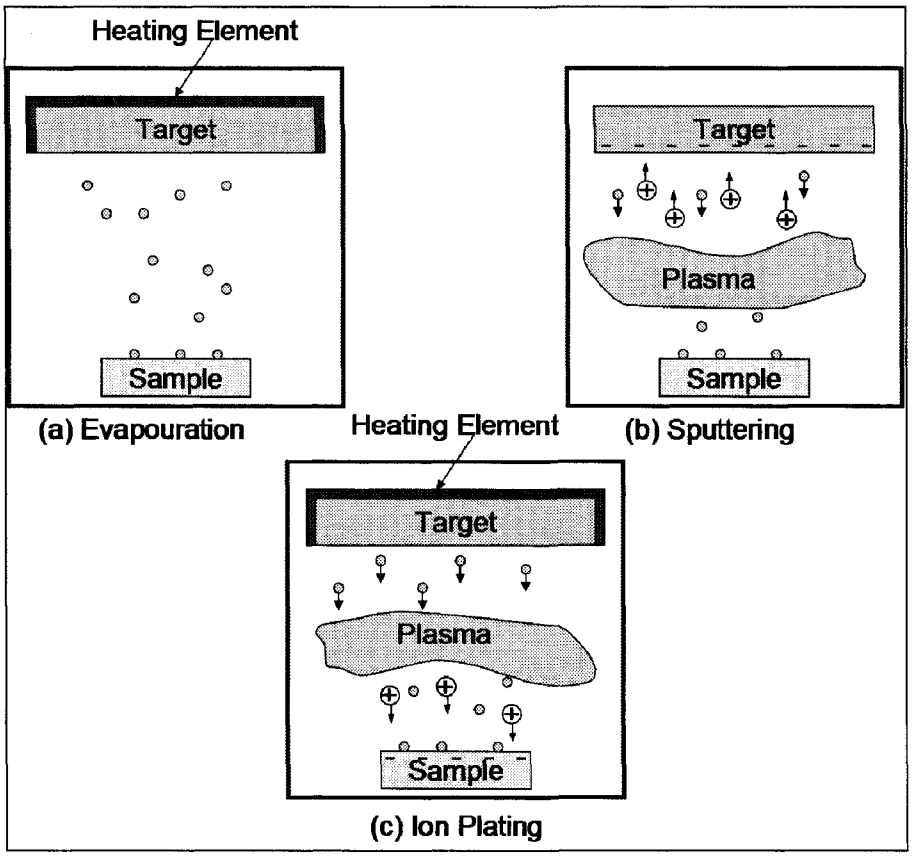

Figure 2-4: Schematics for various PVD systems

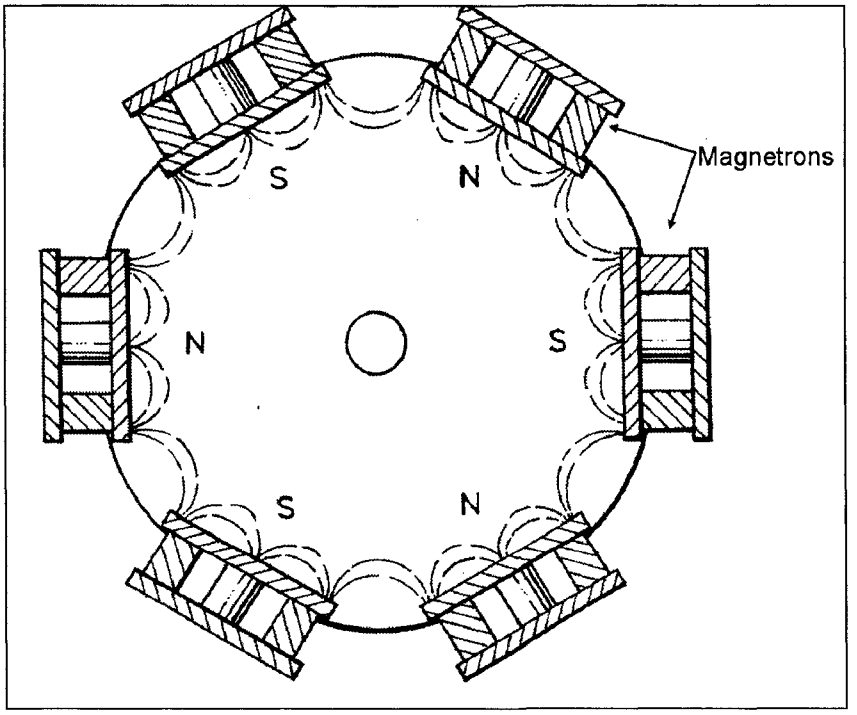

Figure 2-5: Schematic for closed field, unbalanced magnetron sputtering with six magnetrons arranged next to each other with opposite polarity [13]

2.2.3 Adhesion and Internal Stress of DLC

Poor adhesion of DLC coatings on substrates such as steel are commonly observed due to high compressive stresses and difference in elastic modulus, hardness and coefficient of thermal expansion at the interface.

Wei *et al.* [14] studied the stress relief effect of introducing dopants such as Cu, Ti and Si to NH-DLC. The authors deposited NH-DLC by pulsed laser deposition on Si (100) wafer, and the adhesion was assessed by scratching the surface coating. Results revealed that pure non-doped NH-DLC displays poor adhesion due to large compressive stresses. Internal stresses were calculated from the Raman shift of the G peak located at 1500 cm^{-1} wave number, which is related to the internal stress by Equation 2-1. The theory is that if the material is stressed, the interatomic separation change, thus the vibration frequency also change, leading to a shift in the wave number. With this in mind, the larger the shift towards a smaller wave number, the lower the internal compressive stresses [14].

$$\sigma = 2G\frac{1+\nu}{1-\nu}\frac{\Delta\omega}{\omega_o} \qquad \textbf{2-1}$$

Where σ is the internal stress, G is the shear modulus, ν is the Poisson's ratio and, $\Delta\omega$ and ω are the wave number and wave number reference respectively of the coating. The Raman results suggest that Ti was more effective in internal stress reduction than Cu and Si dopants.

Non-metallic dopants like hydrogen have also been reduced internal stresses. For instance, Iyer *et al.* [15] studied the compressive stresses of H-DLC that had been deposited using PACVD on thin Si substrates with a mixture of propane and butane precursor gas. Internal stresses were identified from the curvature deformation of the

substrate caused by the coating. Then the stresses were calculated using the Stoney Equation 2-2 from the substrate curvature;

$$\sigma = \frac{E_s t_s^2}{6(1-v_s)dR} \qquad \textbf{2-2}$$

where σ is the internal stress, E_s is the elastic modulus of the substrate, v_s is the poissons ratio of the elastic modulus, t_s is the thickness of the substrate, d is the thickness of the coating and R is the curvature of the substrate. The authors learned that compressive stresses decreased as the volume percentage of hydrogen increased (Figure 2-6), because hydrogen relives stresses by promoting a medium range order that encourages the formation of sp^2 clusters.

Another study, investigated the effect of Si on the internal stress of H-DLC, which was found to reduce the compressive stresses. Ban and Hasegawa [16] deposited H-DLC on Si (100) wafer using electron beam-excited plasma CVD with CH_4 and SiH_4 precursor gas. Results prove that internal compressive stresses have decreased from 2.5 to 1 GPa as the flow ratio of SiH_4 during deposition increased to 40 % (Figure 2-7). Thus indicating that as Si content increases internal compressive stresses decrease.

The use of Ti was investigated by Wang *et al.* [17], who studied its effects as an interlayer and a dopant on the internal stresses of H-DLC. The H-DLC was deposited on Si (100) and steel substrates using DC PECVD with methane as a precursor gas. Internal stresses were calculated from the substrate curvature after deposition using the Stoney Equation 2-2. Results showed that the Ti was more effective as an interlayer in reducing the internal stresses for steel than for the Si substrate (Figure 2-8). The authors attributed this behaviour to be due to the coefficient of thermal expansion. When Ti was added on

top of the Si wafer, for example, it produced a great mismatch in the coefficient of thermal expansion between the substrate (Si) and the H-DLC coating. Adding a Ti interlayer on the steel, however, substrate brought the coefficients of thermal expansion closer between the steel substrate and the H-DLC coating. As for Ti as a dopant, results have shown that it reduces the internal compressive stresses of H-DLC on both Si and steel substrates, which is attributed to the decrease in sp^3 content and promoting sp^2 type bonds which relive the internal stresses (Figure 2-9).

Other metallic dopants like Cr were investigated as possible internal stress reduction interlayer. Chen and Hong [18] studied the effects of Cr interlayer thickness on the internal stress reduction of H-DLC. The H-DLC was deposited on a steel substrate with CH_4 and Ar precursor gas using a hybrid system of magnetron sputtering and PA CVD. Internal stresses of various the Cr interlayer were calculated using the Stoney Equation 2-2 revealing that a 0.3 μm Cr interlayer produced the lowest internal stress (1.4 GPa). Furthermore, the authors investigated the effects of intermixing Cr with the steel substrate prior to the Cr interlayer. Intermixing was achieved by increasing the substrate bias to 700 V and reducing the Cr target current to 0.25 A, which promoted high energy Ar to bombard the steel surface and thus allowing Cr to diffuse through the steel. Next, a 0.3 μm of Cr interlayer was deposited on the substrate by increasing the current for the Cr target. As a result of intermixing, the internal stress of H-DLC decreased to 0.5 GPa.

Therefore, adhesive carbide formers interlayer or dopants such as Cr, Si and Ti are commonly introduced before depositing the DLC coating on the substrate to insure strong adhesion and prevent spallation.

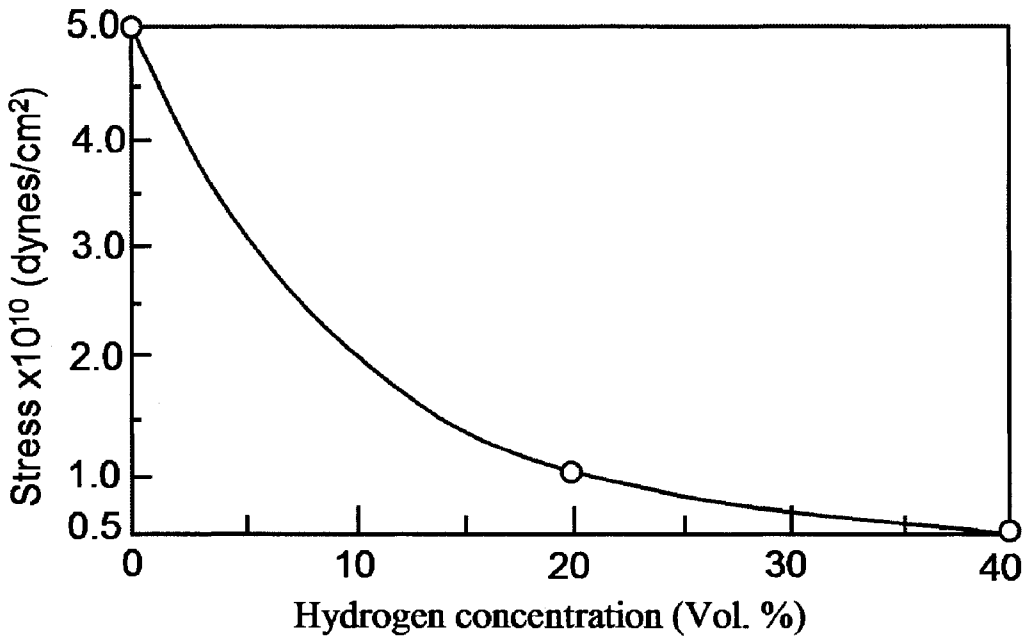

Figure 2-6: Internal compressive stress as a function of hydrogen concentration [15]

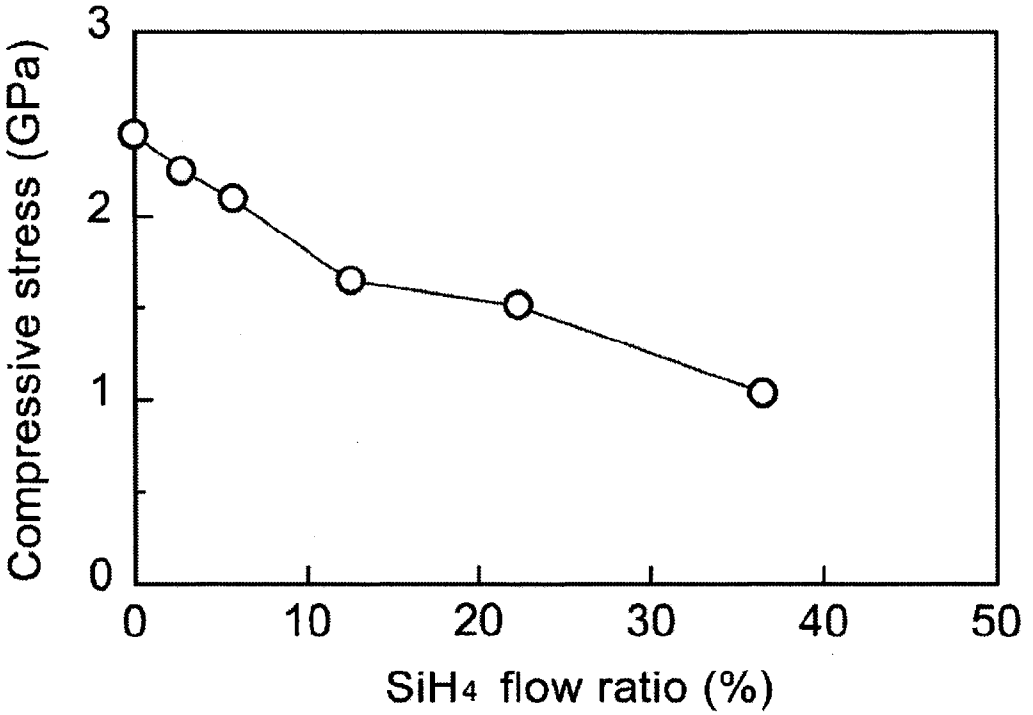

Figure 2-7: Internal stress as a function of precursor gas (SiH) flow ratio [16]

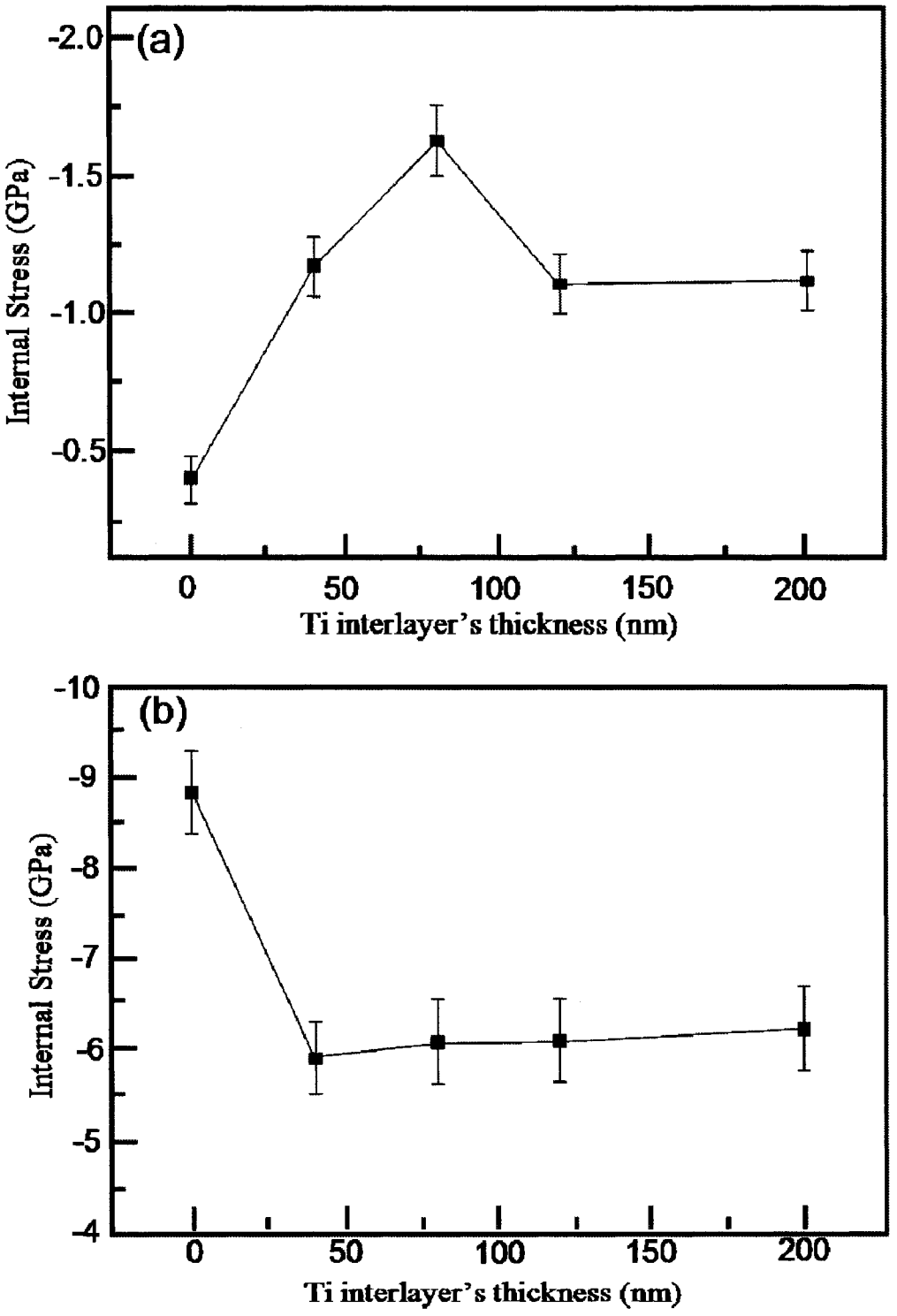

Figure 2-8: Influence of Ti interlayer thickness on H-DLC internal stress when deposited on (a) Si wafer and (b) stainless steel [17]

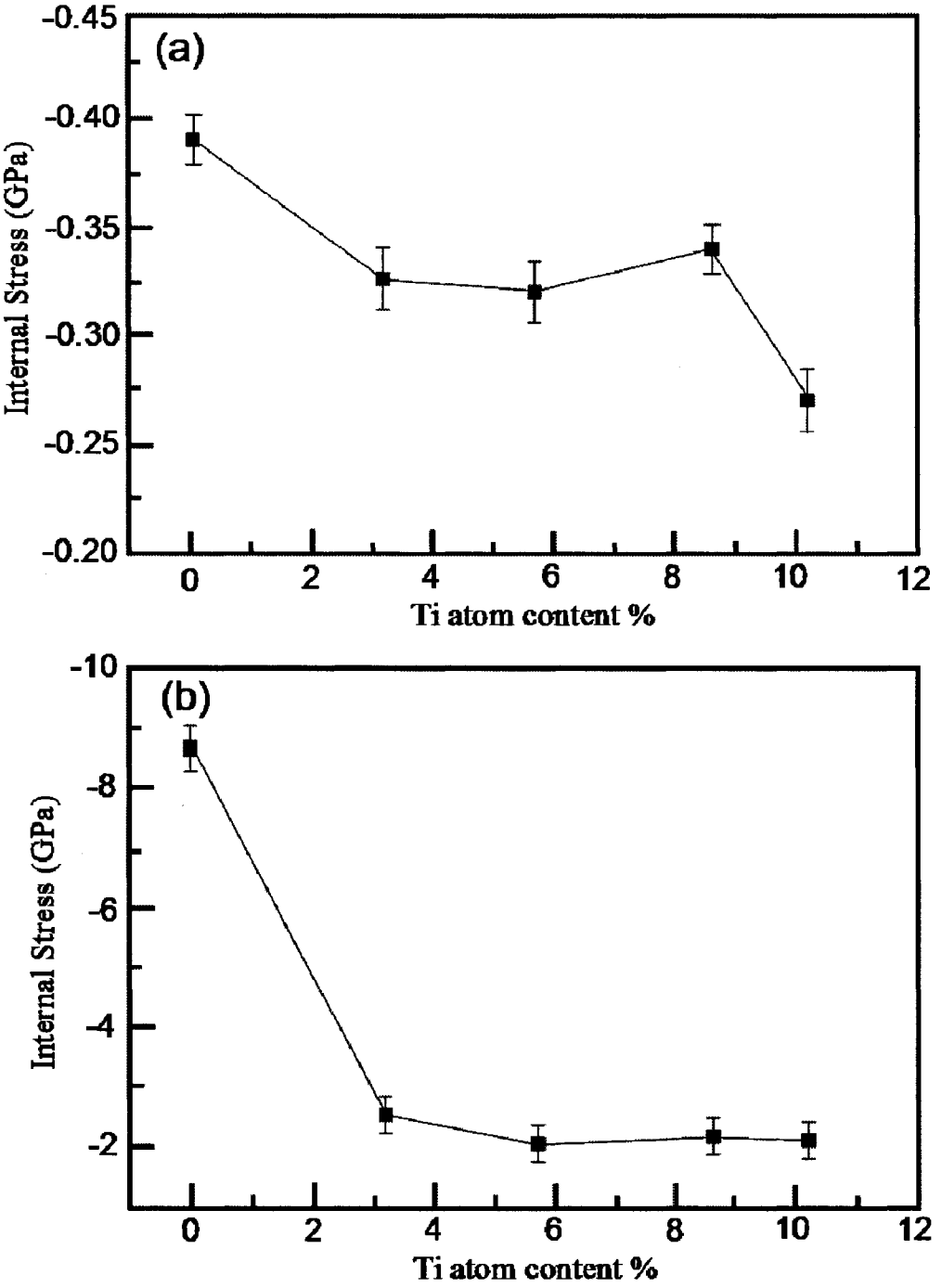

Figure 2-9: Influence of Ti as a dopant on the H-DLC internal stress when deposited on (a) Si wafer and (b) stainless steel [17]

2.3 Tribological Behaviour

The tribological behavior of DLC is greatly influenced by testing conditions and the nature of the surrounding atmosphere, like presence of hydrogen and water vapour.

2.3.1 Effect of Deposition Parameters

Deposition parameters such as substrate bias, precursor gas flow and deposition time affect the chemical and mechanical properties of the DLC coating, which alters the tribological behaviour. Zhang *et al.* [19] studied the effect of substrate bias on the chemical, mechanical and tribological properties of NH-DLC. NH-DLC was deposited on 440C stainless steel substrate using a magnetron sputtering technique. The authors observed that as the substrate bias voltage increased from -20 to -160 V, the COF increased from 0.09 to 0.21, when an alumina ball was tested against NH-DLC at 75% RH for 0.3 km. Furthermore, surface hardness increased up to 30 GPa as bias increase to -150 V. Meanwhile, the surface roughness was observed to decrease as bias voltage increase. In addition, Raman spectrum showed that the intensity ratio of the disorder peak to the graphitic peak (I_D/I_G) decreased as the bias voltage increased, which indicates an increase in the sp^3 fraction. Higher sp^3 fraction, however, lead to higher residual stress in the coating.

Another study by Zhang and Tanaka [20], investigated the effects of high substrate bias voltage on the tribological behaviour of H-DLC. H-DLC was produced by PA-CVD with benzene as a precursor gas. Three coatings were produced at different substrate bias, -1 kV, -2 kV and -3 kV. A 6 mm SiC ball was tested against H-DLC for 10000 cycles, with a 1 N load, a RH ranging from 4-6% and 0.1 m/s sliding speed in dry air, N_2, O_2 and vacuum atmospheres. The COF was observed to be insensitive to high

bias voltage changes. In dry air, for example, the COF was 0.05 and 0.04 for H-DLC produced with -2 and -3 kV, respectively. Similarly, in N_2, O_2 and vacuum atmospheres experiments the COF was 0.06, 0.1 and 0.15, respectively, at both -2 and -3 kV.

Deposition parameters like bias voltage significantly influence the chemistry of the NH-DLC coating. Increasing the bias to -150 V lead to an increase in the sp^3 fraction. As a result, the hardness increased to 30 GPa and the COF reached 0.21. A high bias voltage, in the order of thousands, however, does not seem to affect the tribological behaviour of H-DLC.

2.3.2 Effect of Dopants

Based on DLC's chemical composition, their tribological behaviour varies significantly. For instance, Donnet and Grill [21] explored the influence of hydrogen content on the friction of DLC coatings. H-DLC coatings were deposited using a DC PACVD on 440C steel with 5 nm Si interlayer. The authors examined the influence of hydrogen that was being induced in the coating from acetylene and cyclohexane precursor gases. The study concluded that cyclohexane is a more efficient gas than acetylene for producing higher hydrogen content in the DLC coating, because cyclohexane has a higher hydrogen-to-carbon ratio compared to acetylene. The study also explored the effect of hydrogen content on the friction behaviour of DLC coatings in vacuum ($1x10^{-8}$ Pa) and ambient air (40-60 %RH). Results showed that in vacuum the COF was approximately 0.5 or higher, when hydrogen content reached up to 34 at%. The DLC containing 42 at% hydrogen lead to a very low COF of 0.02 when sliding in vacuum. As for ambient air results, hydrogen content did not influence the COF in ambient air fluctuating from 0.1 to 0.2, as shown in Figure 2-10.

Another study conducted by Erdemir [22] investigated the influence of hydrogen content in the DLC coating deposited by PE CVD as a function of source gas and tribological performance. The author concluded that the higher the hydrogen content in the gas mixture or the higher the H/C ratio, the higher the hydrogen content in the DLC coating, resulting in lower friction. For instance, DLC produced by C_2H_2, CH_4, 75%CH_4+25%H_2, 50%CH_4+50%H_2 and 25%CH_4+75%H_2, generated a COFs of 0.3, 0.014, 0.01, 0.004 and 0.001, respectively, when tested against itself at 10 N load and 0.5 m/s speed, in dry nitrogen atmosphere.

Other dopants have different effects on the tribological behaviour and the mechanical properties of the coating. For example, metallic dopants such as Ti, Nb, Ta, Cr, Mo, W, Ru, Fe, Co, Ni, Al, Cu, Au and Ag, increase hardness and improve wear resistance [23]. Non-metallic dopants such as N, F, O, P and Si influence the surface energy. For instance, F and Si increase the contact angle on the surface, resulting in a lower surface energy while N, P and O increase the surface energy [24].

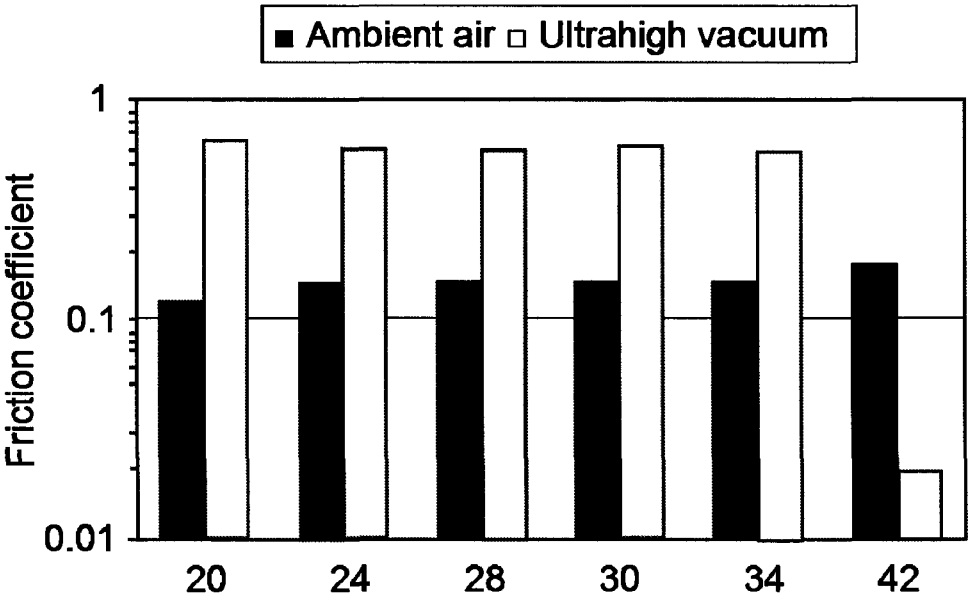

Figure 2-10: Effect of hydrogen content on the COF in ambient air and vacuum [21]

2.3.3 Effect of Hydrogen Atmosphere

The presence of hydrogen inside the DLC coating, as previously discussed reduced the COF significantly under inert and vacuum atmospheres. Other studies explored the effect of hydrogen gas on the friction behaviour of DLC in testing atmospheres. Fontaine *et al.* [25] studied the healing effect of hydrogen gas on the tribological performance of H-DLC. The authors tested a 52100 steel pin against H-DLC with 34 at% of hydrogen deposited on a Si (100) substrate with a 5 N load and 0.5 m/s sliding speed. When H-DLC was tested in vacuum ($1x10^{-6}$ Pa), the COF reached a very low value of 0.01. After 100-200 cycles, the COF increased, reaching a value of 0.1. This sudden increase in the COF is attributed to the strong adhesion between the steel sliding pin and the H-DLC coating due to the depletion of the carbon transfer layers. On the contrary, when hydrogen partial pressure was increased inside the test chamber to 500 and 1000 Pa, the very low COF of 0.01 was maintained, lasting for 1000 cycles. As observed by the authors, the increase in hydrogen pressure preserved the carbon transfer layers, which prevented adhesion and leading to a weak, van der Waals type of interactions.

Konca *et al.* [26], conducted another study on this topic that explored the role of hydrogen atmosphere on the friction behaviour of NH-DLC. A 319 Al pin was tested against NH-DLC coating in a 60% He - 40% H_2 atmosphere. The reported COF was as low as 0.01 (Figure 2-11), meaning that the H_2 efficiently passivate the unoccupied carbon bonds on the NH-DLC surface, minimizing surface interactions that produce a very low COF. To confirm whether the low friction was a result of H_2 passivation rather than He, the 319 Al was tested against NH-DLC in a pure He atmosphere. The test

produced a COF of 0.74 (Figure 2-12), indicating that He does not lower the COF and supporting the claim that H_2 passivates the unoccupied carbon bonds on the surface.

The literature confirms that hydrogen is the key element for maintaining a low COF in H-DLC, and the solution for the high COFs produced by NH-DLC in vacuum.

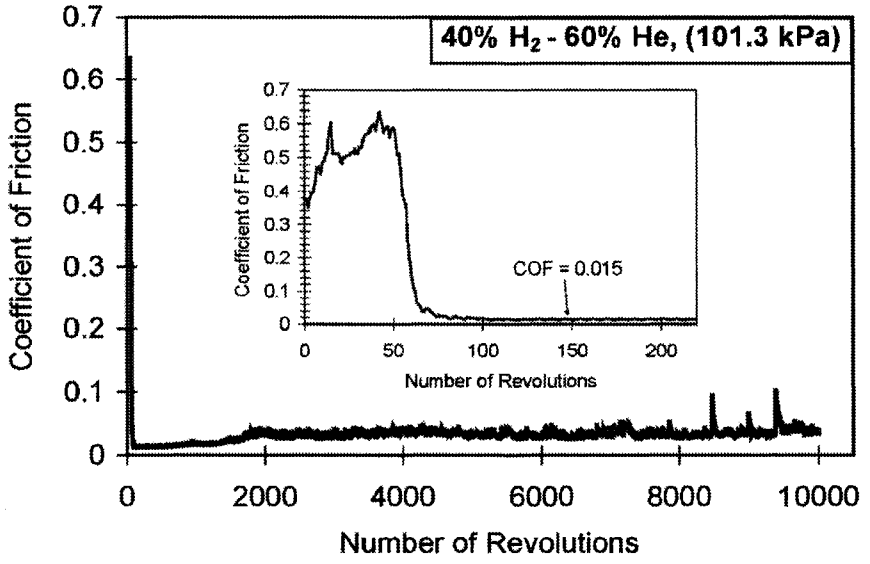

Figure 2-11: Influence of 40%H2 -60%He gas mixture in the atmosphere on the COF of 319 Al against NH-DLC at 5 N load and 0.12 m/s speed [26]

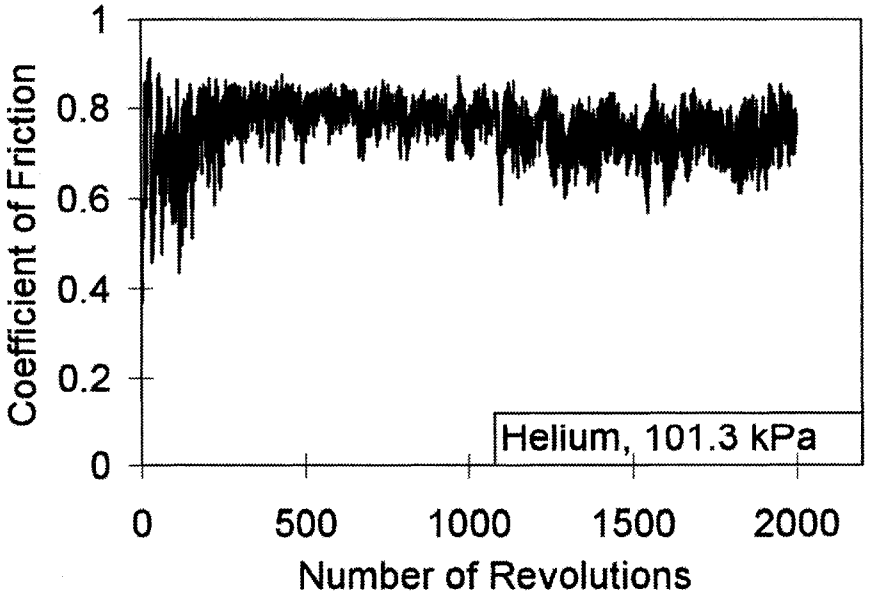

Figure 2-12: Influence of He atmosphere on the COF of 319 Al against NH-DLC at 5 N load and 0.12 m/s speed [26]

2.3.4 Effect of Humidity

Relative humidity (RH) has been found to be a major contributor to the changes observed in the tribological behavior of DLC coatings. For instance, Donnet *et al.* [27] explored the role of oxygen and water vapor on H-DLC, deposited with DC PACVD on Si wafer using cyclohexane precursor gas and producing 42 at% of hydrogen. The authors tested 52100 steel against the H-DLC coating at 1 m/s speed and 1 GPa maximum Hertzian contact pressure. Oxygen tests were conducted by evacuating the chamber and increasing the partial pressure of oxygen. Results showed that varying the oxygen partial pressure from 10^{-10} hPa and 60 hPa (lower than an atmospheric pressure of 210 hPa) had no influence on the friction behaviour, producing a low COF of 0.01, as observed in vacuum. On the other hand, water vapor clearly affected the COF, where as the water vapor pressure increased from 0% to 100% RH, the COF increased (Figure 2-13). Likewise, the COF decreased as the water vapour pressure decreased (Figure 2-14) confirming the relationship between the COF and RH. The analyses of the steel ball shown in Figure 2-15, illustrate that rich, thick carbon transfer layers formed on the 52100 steel ball in vacuum (0% RH), while at a higher vapour pressure, less pronounced carbon transfer layers were observed. The study concluded that a low RH induces H-DLC to form carbon transfer layers on the counter surface, reducing the COF while at high water vapour pressure, carbon transfer layers are suppressed, causing the COF of H-DLC to increase.

Other studies investigated the influence of humidity on the NH-DLC coating. Konca *et al.* [28], conducted a pin-on-disc wear test with a 319 Al pin and WC ball against a NH-DLC coating with a 5 N load and a 0.12 m/s linear speed. The results

revealed a great COF dependency on the RH, for instance as RH increased the COF decreased (Figure 2-16). The authors concluded that the NH-DLC adsorb water and together with carbon transfer layer formation, the COF drop to 0.07 in humid air from 0.55 in dry air.

This relationship was confirmed by Qi *et al.* [29] when they simulated gas molecule adsorption at the surface level of a (111) diamond surface and work of separation. The simulation compared the adsorption of N_2 and H_2O gases and results proved that water molecules dissociated to H and OH as they approached the surface, passivating the unoccupied carbon bonds. The calculated work of separation between C-OH and C-OH surfaces is 0.02 J/m^2. In the case of an inert gas like N_2, no dissociation occurred because N_2 did not passivate the C surface and the calculated work of separation between Al and C surfaces was much higher than the passivate surface with a carbon transfer (4.5 J/m^2). This indicates that the presence of carbon transfer on the mating surface reduces the work of separation, which reduces the COF.

A more recent study by Liu *et al.* [8] compared the friction behaviour of diamond to H-DLC and NH-DLC. The authors conducted a linear reciprocating wear test of a aluminum oxide ball against diamond, H-DLC and NH-DLC coatings at a 2 N load with a 100 um stroke at 8 Hz frequency for 100,000 cycles. The resulting COF decreased from 0.09 to 0.03 as the RH increased from 10% to 85% respectively, for the diamond surface. Similar behavior was observed for NH-DLC. As the RH increased from 5% to 90%, the COF decreased from 0.1 to 0.04 (Figure 2-17). H-DLC, however, behaved contrarily to diamond and NH-DLC, with the COF increasing from 0.07 to 0.13 (Figure 2-18) as the RH increased from 5% to 85%. From the study, it was concluded that water was adsorbed

by diamond and NH-DLC, decreasing the shear stress at the interface, while the interactions between hydrogen and oxygen played an important role in the tribological behaviour of the H-DLC.

Therefore, it was observed that humidity has a negative effect on the COF of H-DLC and prevent carbon transfer from forming on the counterface. While higher humidity levels terminate the unoccupied carbon bonds by dissociating to H and OH and forming easily sheared carbon transfer, the work of separation between the sliding surfaces is reduced, promoting a low COF.

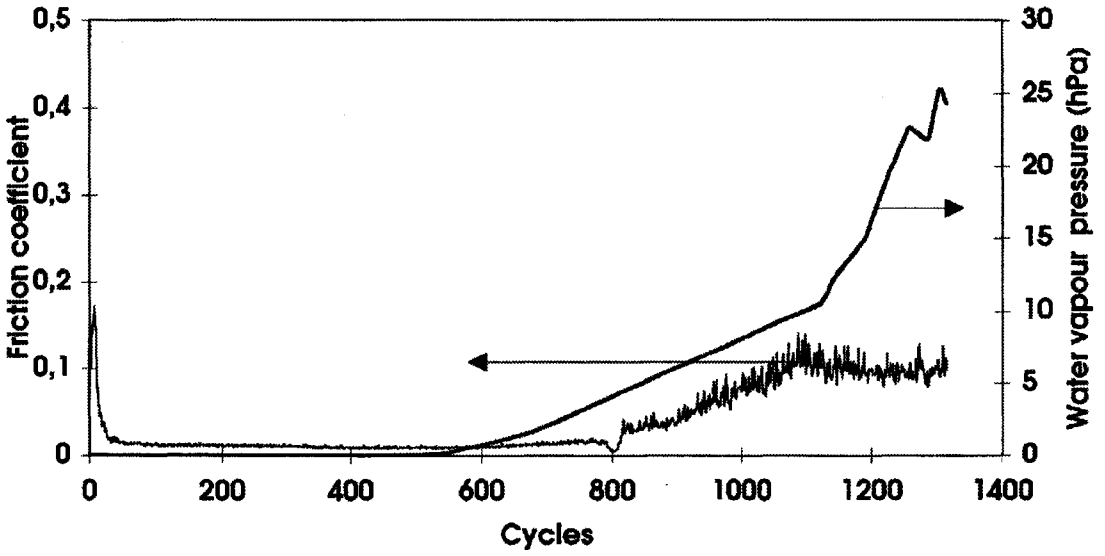

Figure 2-13: Effect of water vapor pressure increase on the COF of 52100 steel ball sliding against H-DLC with 0.1 m/s speed and 1 GPa contact pressure [27]

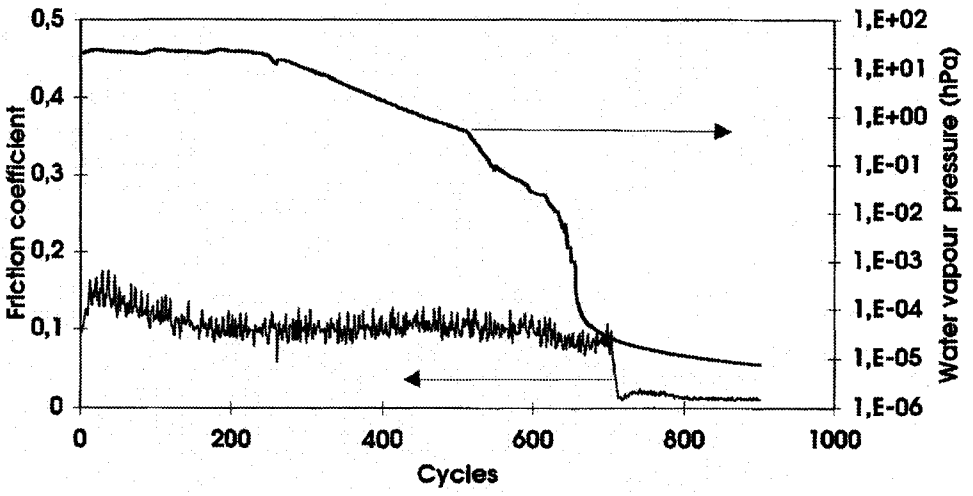

Figure 2-14: Effect of water vapor pressure decrease on the COF of 52100 steel ball sliding against H-DLC with 0.1 m/s speed and 1 GPa contact pressure [27].

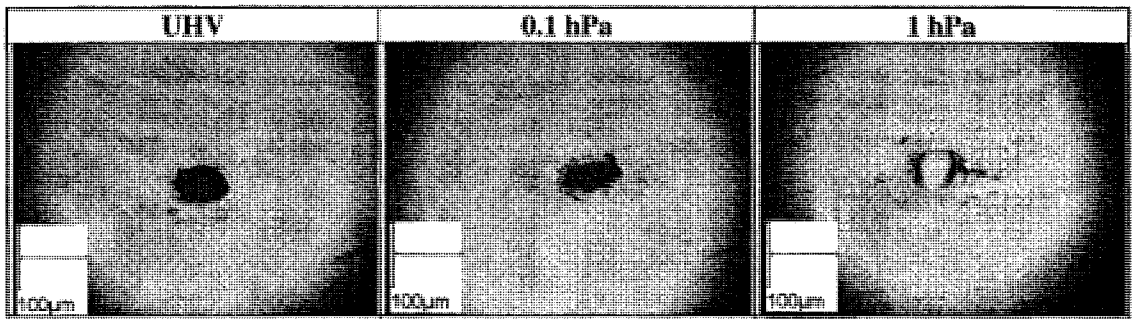

Figure 2-15: Transfer layers on 52100 steel from H-DLC coating [27].

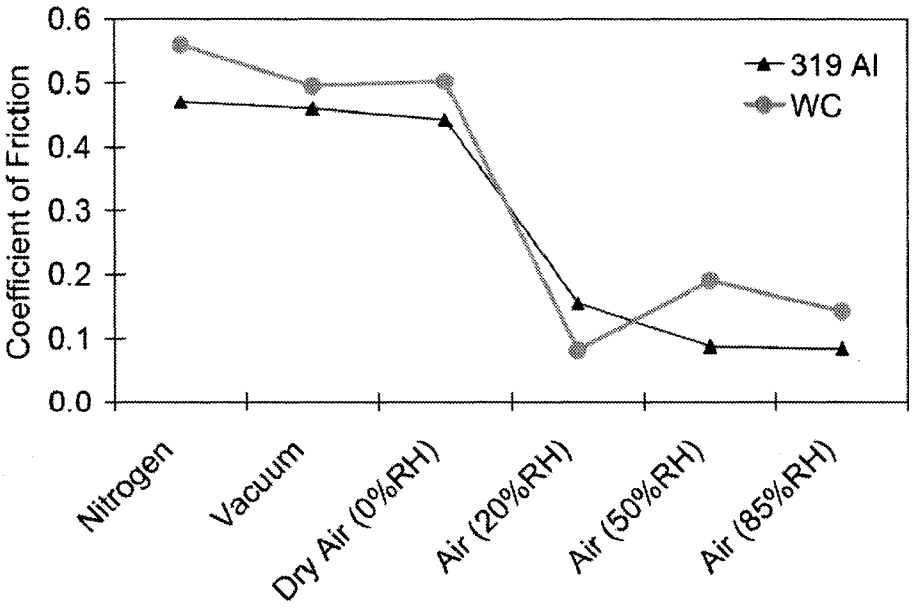

Figure 2-16: Environmental effect on NH-DLC at 5 N load and 0.12 m/s speed [28].

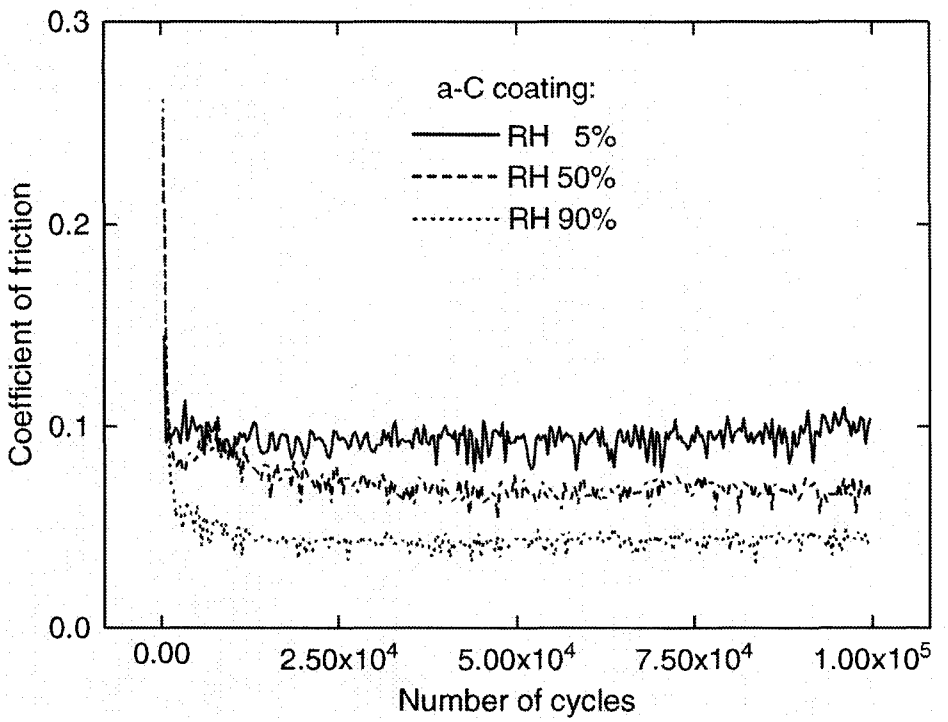

Figure 2-17: Influence of humidity on the friction behaviour of a corundum ball sliding against NH-DLC in air with 2 N load and 100 μm stroke at 8 Hz [8].

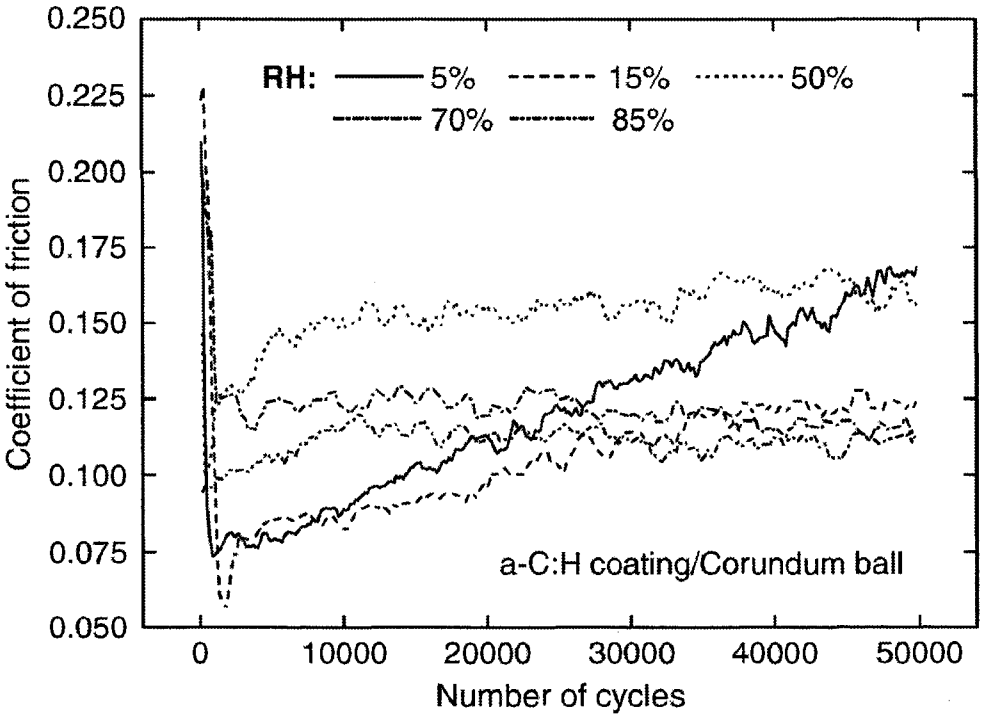

Figure 2-18: Influence of humidity on the friction behaviour of a corundum ball sliding against H-DLC in air with 2 N load and 100 μm stroke at 8 Hz [8].

2.3.5 Vacuum and Inert Atmosphere

The tribological behavior of H-DLC and NH-DLC coatings differs significantly under vacuum or inert atmosphere (i.e. N_2 or Ar). Erdemir [22] tested H-DLC and NH-DLC in dry nitrogen atmosphere. The H-DLC coatings were tested against a H13 steel disc with a 10 N load and a 0.3 m/s speed. The results showed that the H-DLC produced a COF of 0.005, while NH-DLC produced a COF of 0.75 (Figure 2-19). The author attributed the difference to be due to the hydrogen content inside the coating, which prevented cross-linking or double bonds between the carbon atoms. Hydrogen was also seen to eliminate π-π interactions in the graphite phase and passivate free σ-carbon bonds.

Konca *et al.* [7], noted similar NH-DLC results while testing a 319 Al pin against NH-DLC under vacuum with a 5 N load and a 0.12 m/s linear speed to produce a COF of 0.52. The relatively high COF (Figure 2-20) was explained by a lack of passivants such as hydrogen or water under vacuum. In this enviroment, free σ-carbon bonds on the NH-DLC surface interact with the aluminum counterface, which cause aluminum to transfer on the NH-DLC track. Aluminum transfer prompts the sliding behaviour to change to metal/metal contact, leading to the observed high COF.

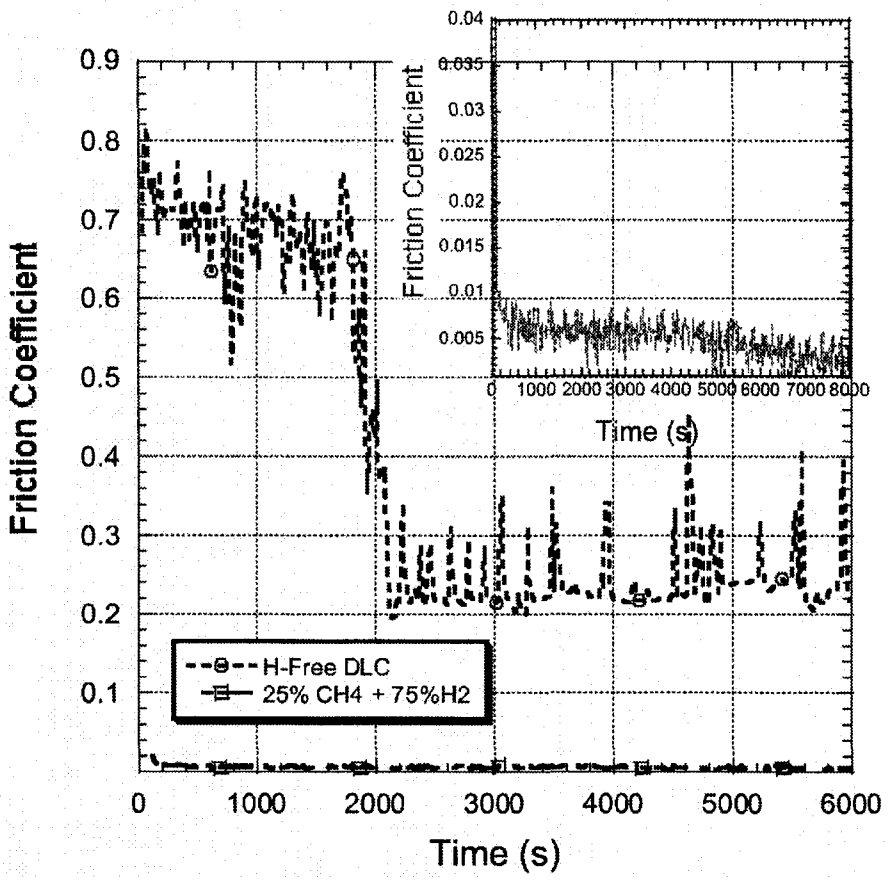

Figure 2-19: COF of H13 steel sliding against hydrogenated and non-hydrogenated DLC in dry nitrogen with 10 N load and 0.3 m/s speed [22].

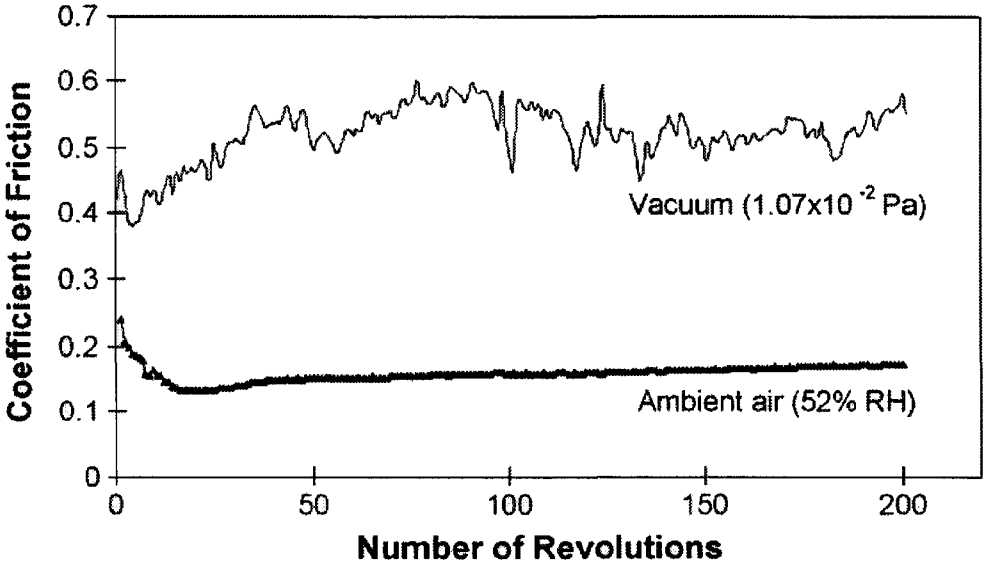

Figure 2-20: 319 Al pin against NH-DLC under vacuum and ambient air with 5 N applied load and 0.12 m/s linear speed [7].

2.3.6 Why does Aluminum Adhere to Carbon?

Tribological studies of aluminum sliding against NH-DLC coatings [28] have revealed that aluminum adheres to the non-terminated carbon surface. Qi and Hector [30] explained this observation with a study that computed and compared the work required to separate aluminum/carbon (Al/C) at the interface (W_{sep}). Three different Al/C interfaces were investigated, Al(111)/C(111)-1x1, Al(111)/C(111)-2x1 and Al(111)/C(111)-1x1:H, where the bonds are terminated with hydrogen (Figure 2-21). The adhesive strength was then investigated using tensile strain calculations where the interface was stretched to failure.

W_{sep} was calculated using Equation 2-3, where σ_{iV} is the surface energy of the material i and σ_{12} is the energy of the interface. E_i^{tot} is the total energy of the material, E_{12}^{tot} is the total energy of the interface and A is the total area at the interface. The computed value of W_{sep} for the Al(111)/C(111)-1x1, Al(111)/C(111)-2x1 and Al(111)/C(111)-1x1:H interfaces were 4.08 J/m^2, 0.33 J/m^2 and 0.02 J/m^2 respectively. The calculation indicate that the Al(111)/C(111)-1x1 interface is much stronger than the interface with hydrogen termination.

$$W_{sep} = \sigma_{1V} + \sigma_{2V} - \sigma_{12} = (E_1^{tot} + E_2^{tot} - E_{12}^{tot})/A \qquad \textbf{2-3}$$

The study used an electron localization function (ELF) was utilized to characterize the bonding type, for example ELF = 1, corresponds to covalent bond and ELF = 0.5 corresponds to metallic bond. ELF simulation indicate that the bonding between Al(111)/C(111)-1x1 is covalent, while for Al(111)/C(111)-2x1 interface, the bonding is a mix between covalent/metallic and for Al(111)/C(111)-1x1:H interface the ELF indicate that it is dispersion interactions.

The work of decohesion at the interface, was defined as the energy difference per unit area (E/A) between the fractured system and the interface structure. The calculated decohesion work for Al(111)/C(111)-1x1 (covalently bonded) was 1.56 J/m^2 (Figure 2-22) about 2.5 times higher than the work required to separate at the interface (W_{sep} = 4.08 J/m^2). It became clear that fracture would occur at the Al bulk before reaching the Al/C(111)-1x1 interface (Figure 2-23 (a)). The calculated E/A for Al(111)/C(111)-2x1 was 0.49 J/m^2, more than the computed W_{sep} of 0.33 J/m^2, indicating that fracture will occur at the interface first (Figure 2-23 (b)). Finally the E/A for Al(111)/C(111)-1x1:H was computed to be close to zero confirming that there is no adhesion between the surfaces (Figure 2-23 (c)).

To summarize, the aluminum transfers to the carbon surface due to lack of terminating species that occupying the σ-carbon bonds. Computer simulations confirmed that as the aluminum surface approaches the non-terminated carbon surface, strong covalent bonds are formed between the carbon and aluminum. When the surfaces were pulled perpendicular to the interface, the aluminum separated at the bulk before the carbon-aluminum would separate at the interface, due to the fact that metallic bonds (Al bulk) are weaker than covalent bonds (Al/C interface), which confirms the presence of aluminum adhesion to the NH-DLC surface.

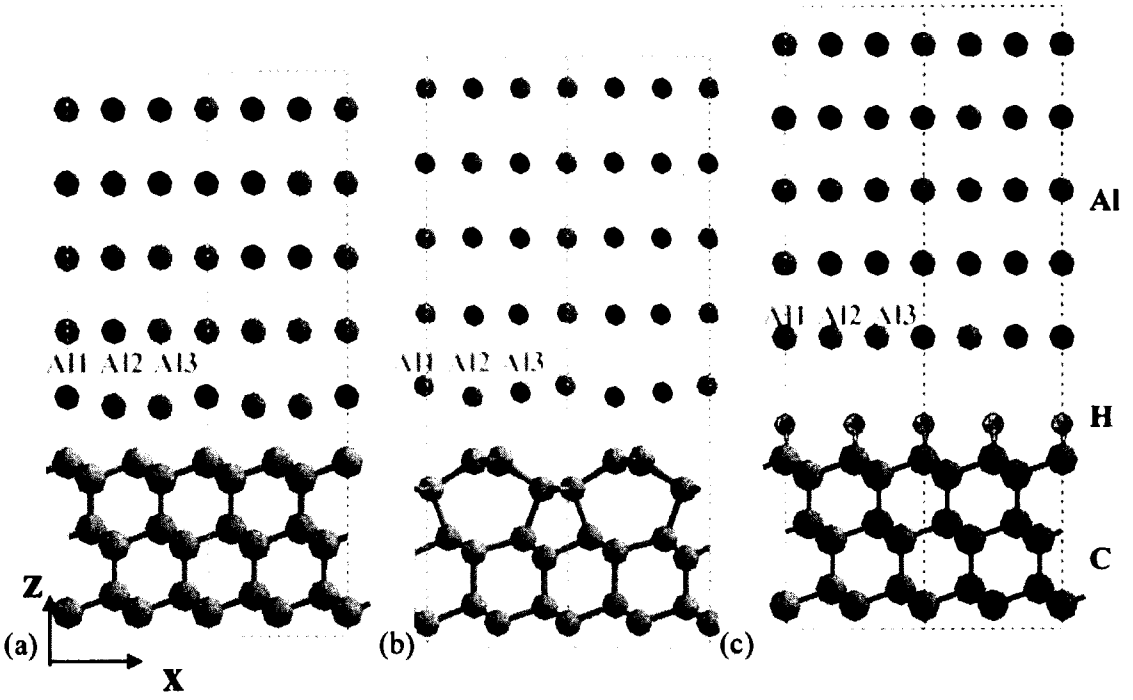

Figure 2-21: Schematics for (a) Al(111)/C(111)-1x1, (b) Al(111)/C(111)-2x1 and (c) Al(111)/C(111)-1x1:H interfaces [30]

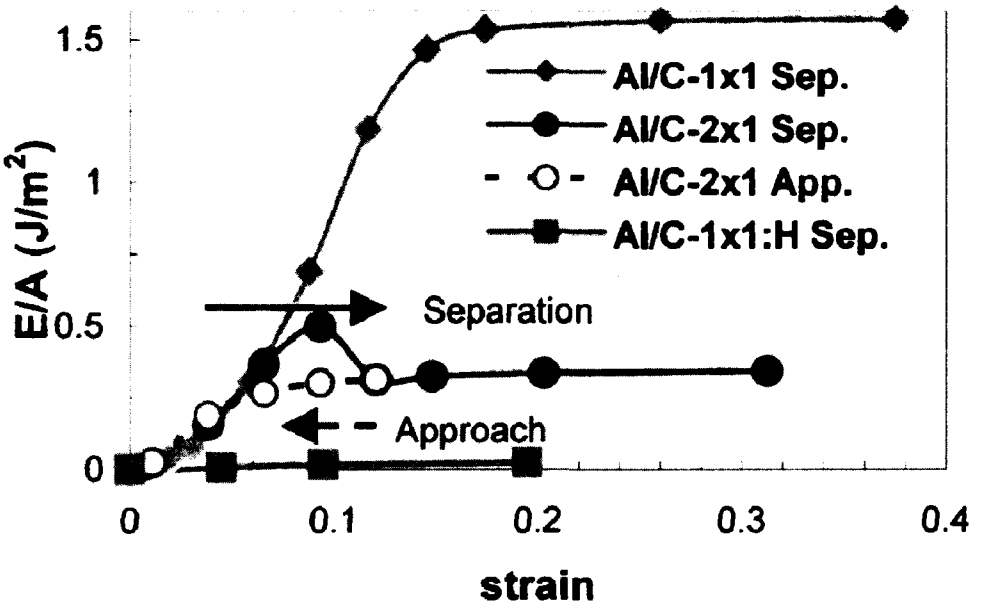

Figure 2-22: Energy per area (E/A) of Al(111)/C(111)-1x1, Al(111)/C(111)-2x1 and Al(111)/C(111)-1x1:H interfaces [30]

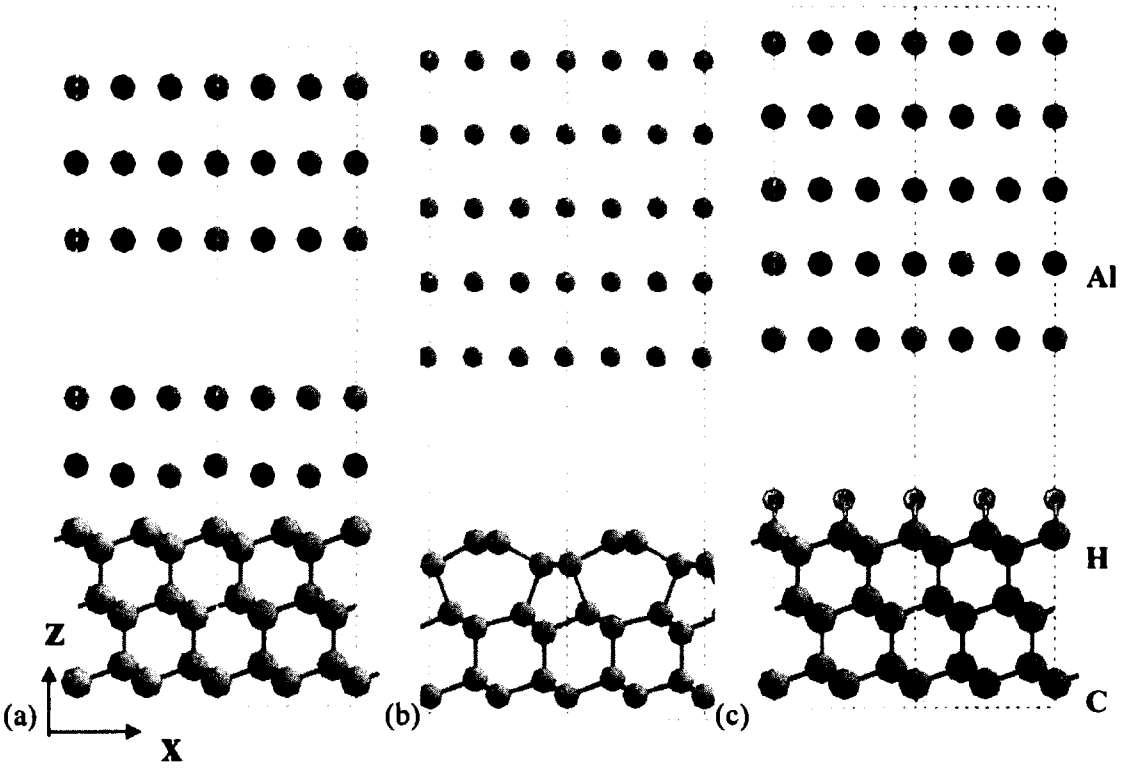

Figure 2-23: Schematics for (a) Al(111)/C(111)-1x1, (b) Al(111)/C(111)-2x1 and (c) Al(111)/C(111)-1x1:H interfaces after applying strain perpendicular to the interface [30]

2.3.7 Friction during Transition from Air to Vacuum

As seen in the previous section the COF for H-DLC and NH-DLC can be manipulated by altering the testing atmosphere. Konca *et al.* [7] studied the tribological behaviour of 319 Al on NH-DLC and the effect of initial running-in period in ambient air, on the COF in vacuum. The authors observed that when the chamber evacuation started, the COF dropped from a steady state COF regime of 0.1 (in ambient air) to a low COF regime (LFR) under vacuum, producing a COF ranging from 0.006 to 0.02. The drop in the COF was believed to be a result of the formation of a carbonaceous layer on the aluminum surface, in addition to an increase in water vapour concentration inside the test chamber as the pressure decreased, which promoted an effective passivation of the unoccupied carbon sigma bonds. In the same study, Konca *et al* [7] also noted that as the duration of initial sliding in the steady state regime increased the duration of the LFR regime increasesed as well (Figure 2-24 and 2-25). In Figure 2-24, 319 Al slid against NH-DLC initially for 850 revolutions (rev) in the steady state regime, initially and produced a LFR regime that lasted 2000 rev. Figure 2-25 illustrates how, 319 Al slid against NH-DLC for 2900 rev in the steady state COF regime while maintaining a similar speed and load as in the previous test Figure 2-24, resulting in a LFR regime that lasted for 4000 rev.

Test speed also has an affects the LFR regime. As the speed increases, the LFR regime's duration decreases. In experiments where 319 Al is sliding against NH-DLC at a speed of 0.04m/s speed for 850 rev in the steady state regime, a LFR regime was produced that lasted for 2000 rev (Figure 2-24). However, when the test was repeated at

a higher speed of 0.15 m/s (Figure 2-26) the LFR regime only lasted for 300 rev, despite a longer initial steady state COF regime of 1200 rev.

The duration of the LFR regime is also influenced by the counterface material [28] and [31]. When Ti was tested against NH-DLC for a 2000 rev initial steady state in ambient air, for example it produced a 300 rev of LFR was produced. When the Al counterface was used with a shorter initial steady state in ambient air (1200 rev), it produced the same LFR duration of 300 rev was produced, even though speed and load were the same. This observation contradicts claims made by previous studies that the longer the steady state COF duration, the longer the LFR regime. It follows that the LFR duration must also depend on the counterface material. This conclusion was confirmed when Al (Figure 2-25) was compared to WC (Figure 2-27) while sliding against NH-DLC. Both counterface materials had similar initial steady state COF regime durations of 2900 rev and 3000 rev for Al and WC respectively. However, WC produced a much shorter LFR duration of 2200 rev compared to Al's 4000 rev, which was almost half and verified that the counterface material played an important role in LFR duration.

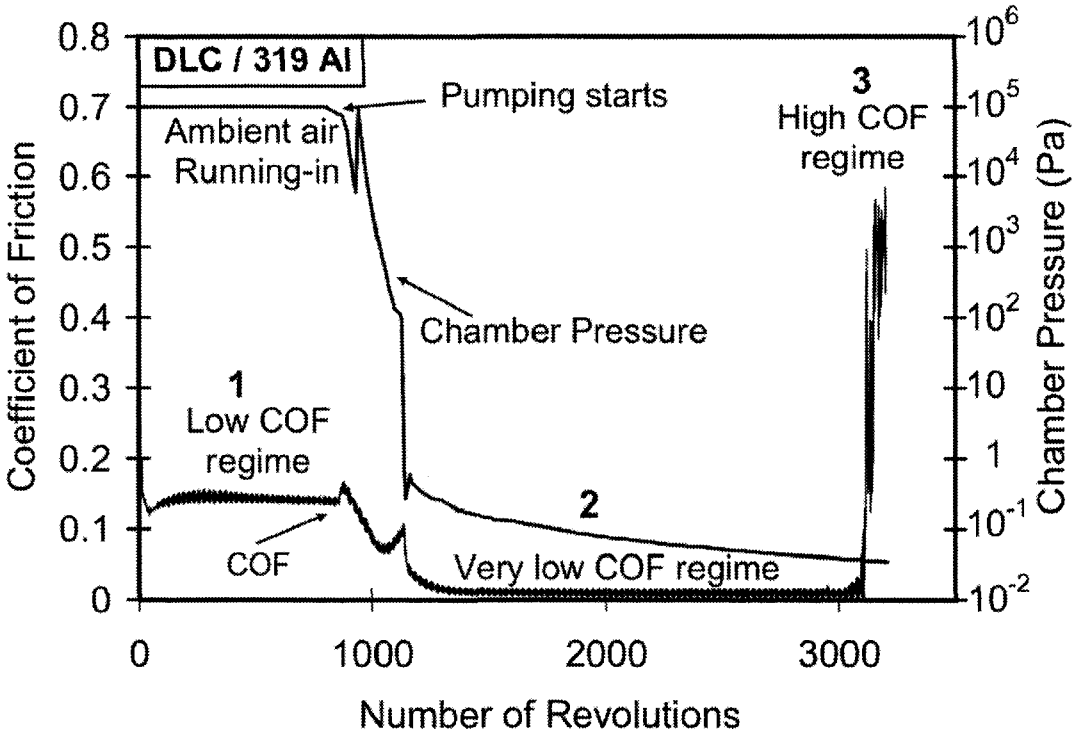

Figure 2-24: 319 Al sliding against NH-DLC at 0.04 m/s and 5 N load: 850 rev in air and 2000 rev of ultra low COF regime [7]

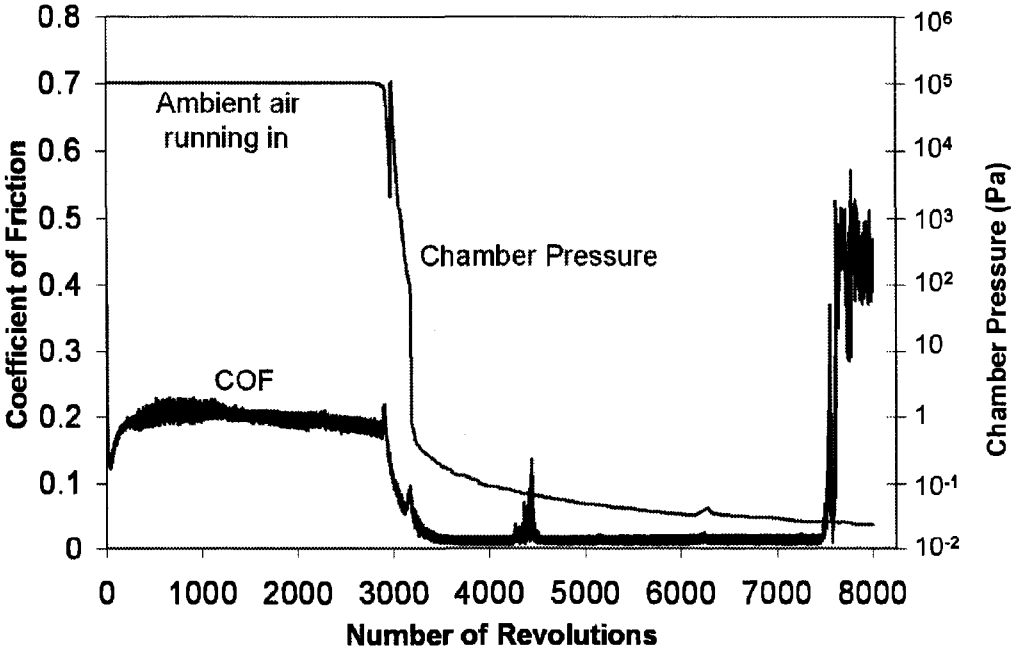

Figure 2-25: 319 Al sliding against NH-DLC at 0.04 m/s and 5 N load: 2900 rev in air and 4000 rev of ultra low COF regime [7]

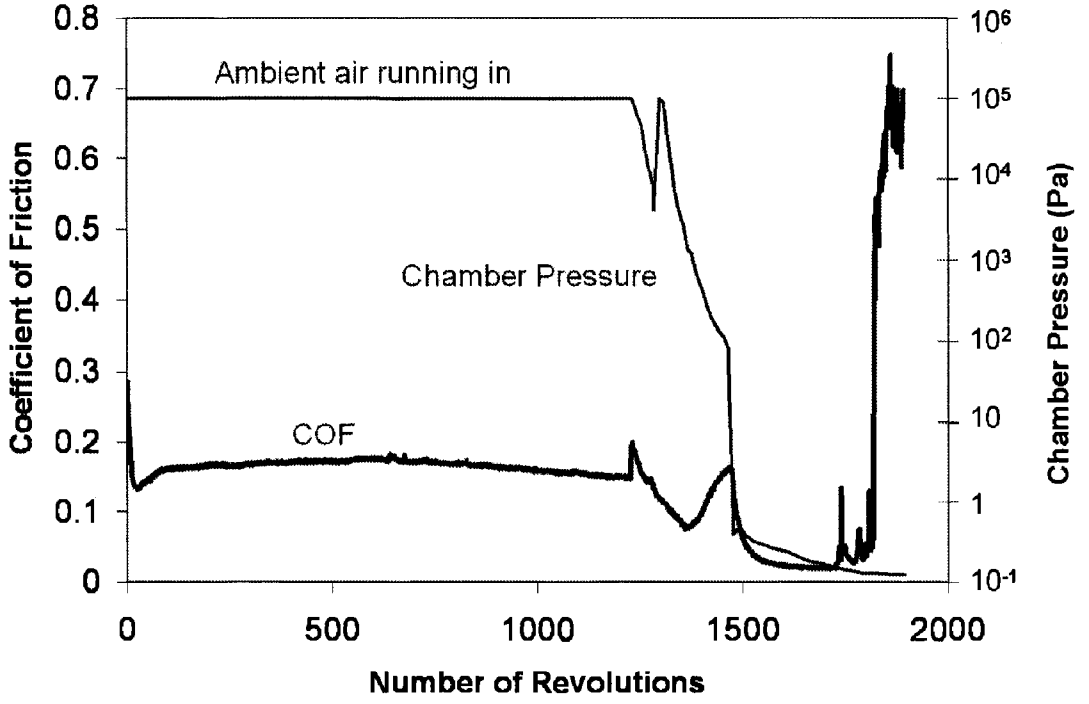

Figure 2-26: 319 Al sliding against NH-DLC at 0.15 m/s and 5 N load: 1200 rev in air and 300 rev of ultra low COF regime [7]

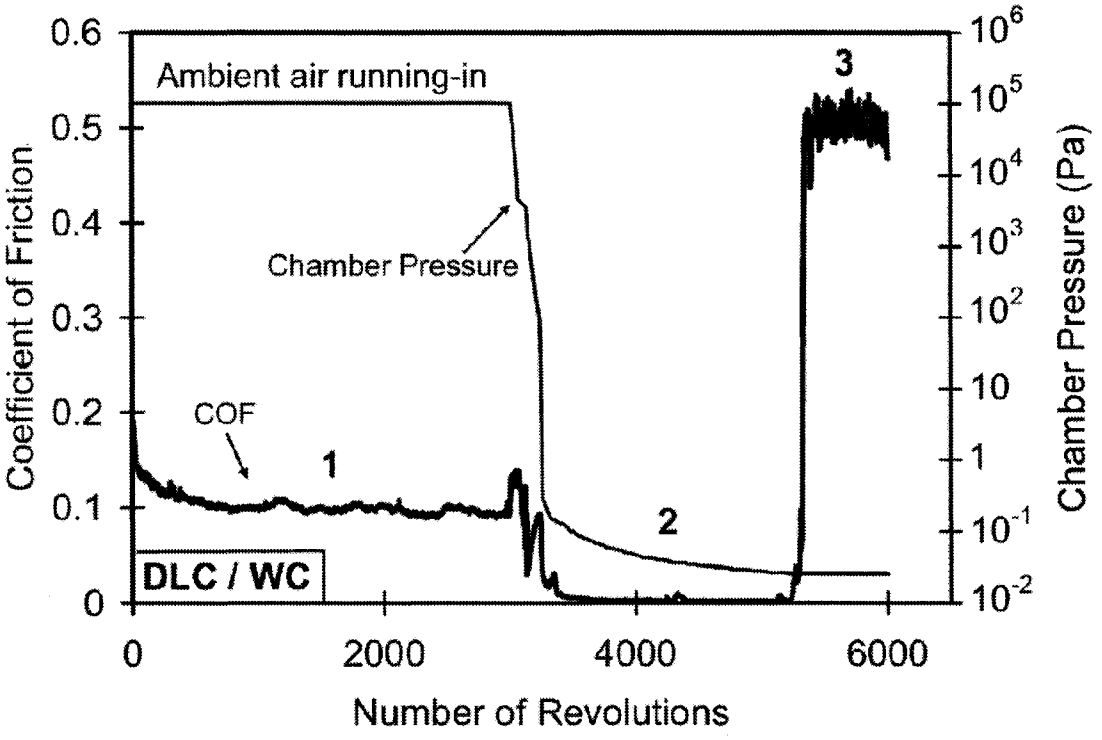

Figure 2-27: WC sliding against NH-DLC at 0.05 m/s and 5 N load: 3000 rev in air and 2200 rev of ultra low COF regime [31]

2.3.8 Lubricated Sliding of DLC Coatings

Previous sections have provided insights into how DLC coatings behave during dry-sliding, and how the friction behaviour can be manipulated by altering the testing atmosphere. DLC coatings are not limited to dry applications; they are also used in lubricated contacts, such as engine components and artificial joints. DLC coatings are usually introduced in areas that experience severe conditions or encounter boundary lubrication (Appendix A) as a way to minimize wear and friction at the metal/metal junctions. Ronkainen *et al.*[32] studied 52100 steel sliding against uncoated steel, NH-DLC, H-DLC and Ti-doped H-DLC. The experiments were conducted at a 10 N load and a 0.004 m/s speed for 300 m, with mineral base oil and an extreme pressure (EP) additive under boundary lubrication. The NH-DLC coating produced a lower friction under BL (0.08) compared to the 0.12 produced by the uncoated steel, H-DLC and Ti-doped H-DLC when in the presence of a mineral base oil and EP additive. NH-DLC and Ti-doped H-DLC produced a lower COF of 0.13 when sliding in a mineral base oil, compared to H-DLC which displayed a COF of 0.2. The authors concluded that Ti improves the friction behaviour of H-DLC in BL, while NH-DLC significantly improves friction in the presence of an EP additive under BL.

Bouchet *et al.* [33] investigated the influence of lubricants (with and without additives) on the tribological behavior of DLC. Results revealed a significant difference between coating one of the mating surfaces and coating both surfaces under lubricated conditions. The author preformed a reciprocating cylinder-on-flat test to observe mild and severe tribological conditions. Three types of DLC coatings were used, H-DLC (50 at% hydrogen), Ti doped H-DLC (35 at% hydrogen) and NH-DLC. The coatings where

deposited on 52100 steel flat and cylinder with diameter and length of 6 and 5 mm respectively. Tests were conducted for 1 hour at 100 °C at a sliding speed of 0.2 m/s and a load that increased gradually to 50 N, where it was maintained for 5 min (run in period) then increased to 350 N. Three types of lubricants were used; PAO, PAO + MoDTC and PAO + MoDTC + ZnDTP. Figure 2-28 and 2-29 illustrate the differences between oil interactions and COF when just one of the mating surfaces is coated with DLC, and when both are coated. Test results indicated that coating one of the mating surfaces with H-DLC, produced a COF of 0.1, while coating both surfaces with H-DLC reduced the COF under the BL regime to produce a COF that was less than 0.1 in the presence of PAO oil. Furthermore, the presence of MoDTC and ZnDTP reduced the friction even more to 0.05 for H-DLC sliding against H-DLC. The addition of a Ti dopant to the H-DLC coating only appeared beneficial in the presence of PAO oil, leading the authors to conclud that MoDTC and ZnDTP additives react with the carbon surface to form easily sheared layers that lower the COF.

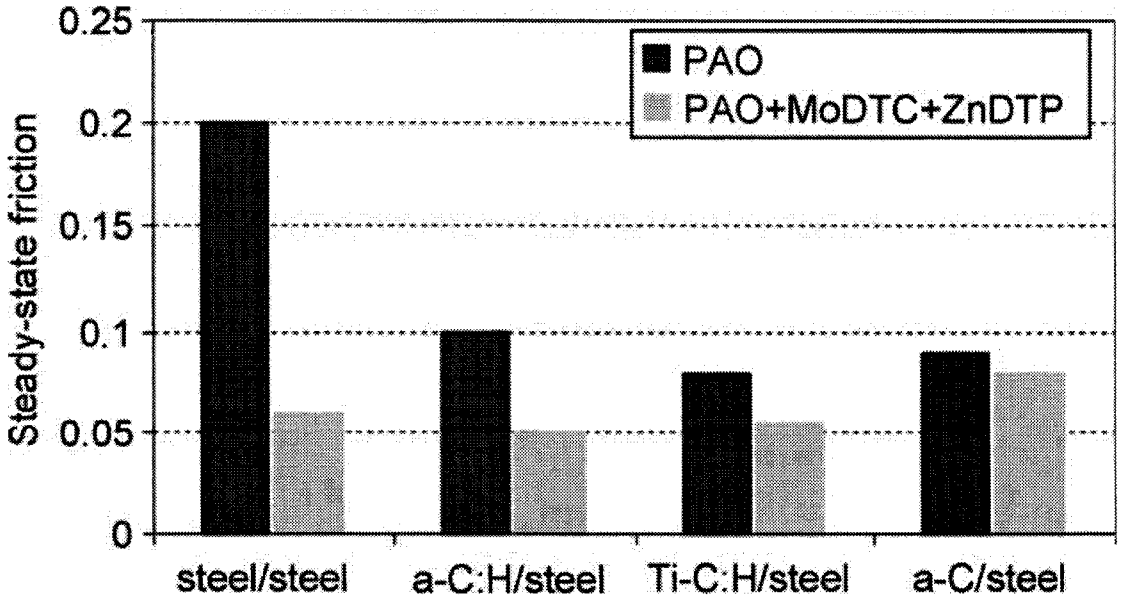

Figure 2-28: Steady state COF for DLC coated flat against 52100 steel cylinder tested under boundary lubrication [33]

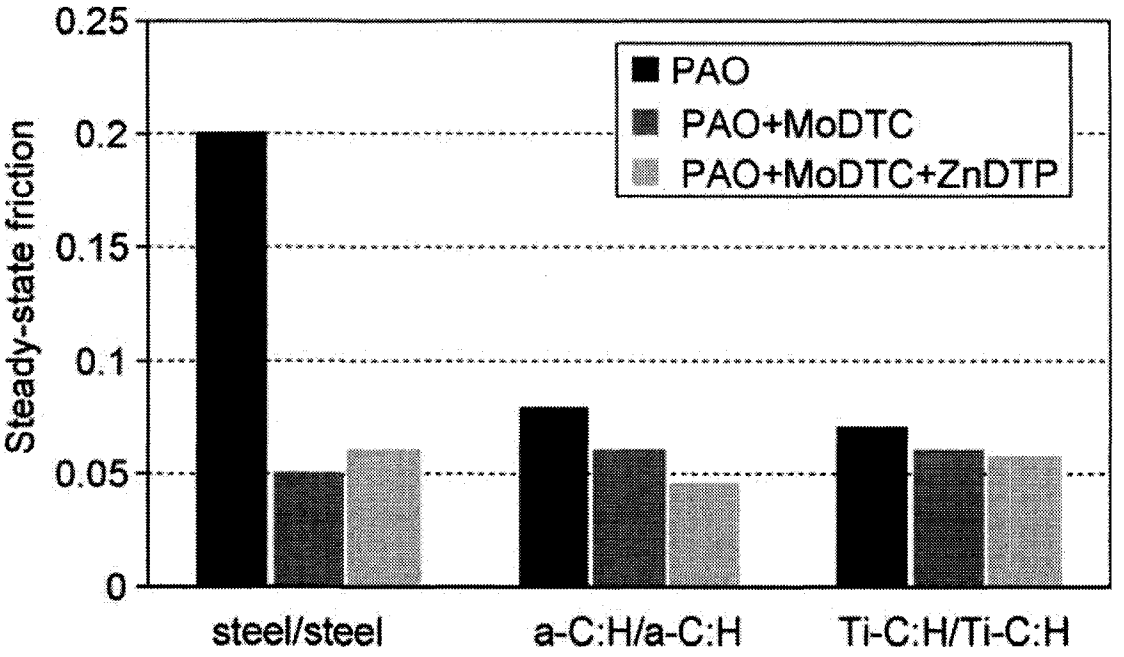

Figure 2-29: Steady state COF for DLC sliding against DLC tested under boundary lubrication [33].

Kalin *et al.* [34] conducted another study on the influence of dopants have on the tribological behavior of DLC under boundary lubrication. In this study, a 10 mm ball slid on a coated stationary DIN 100Cr6 steel disk. Tests were performed at a 0.1 m/s speed, 10 N load for 100 m sliding distance corresponding to lambda ratio of 0.06. DLC coatings are listed in Table 2-2. Results (Figure 2-30) proved that the behavior was independent of the dopant, but the COF behavior was linked to the additives, with mineral (M) oil + AW and EP additives producing the highest COF, and M oil and a EP additive generated the least amount of friction, regardless of the DLC type.

Kalin *et al.* [35] also compared the influence of mineral oil and biodegradable oils on the tribological behavior of steel against steel, steel against DLC and DLC against DLC. Tests were performed using a ball-on-flat machine with a 0.1 m/s speed, a 10 N load at a 100 m distance, with contacts preheated to 80°C. The ball and flat are made of

DIN 100Cr6 steel and two types of coatings were used; H-DLC with Si interlayer, and W-DLC with multilayer WC, carbon and a Cr interlayer. Test results appear in Figure 2-31 and 2-32 for mineral and biodegradable oils respectively. Comparing Figure 2-31 and 2-32, sunflower oil promotes a significant drop of 30 % in the COF compared to mineral oil, because the sunflower oil features large amounts of unsaturated molecules and polar components or Fatty Acids, as described in Appendix B.

As for lubricated sliding under the BL regime, friction is governed by temperature, surface morphology, surface chemistry, the presence of polar groups and chain length in the oil. The authors discovered that coating the sliding surfaces with a lubricious coating, such as DLC, reduced the COF in the BL regime. The literature has not clarified what mechanism is dominating the tribological behavior of DLC coatings under BL conditions during sliding , but studies have shown that friction modifiers and additives like ZnDTP and MoDTC work well with H-DLC to produce a COF of 0.05 under BL. In addition, dopants such as Ti and W seem to decrease the COF even further.

This thesis investigates the tribological behaviour of 319 Al sliding against both NH-DLC and H-DLC coatings in an effort to improve and optimize the drilling and machining of the common automotive alloy, 319 Al, by identifying the friction mechanisms. The study examines the friction behaviour of AISI 52100 grade steel sliding against both NH-DLC and H-DLC coatings under BL in the presence of ATF. The following section of this dissertation will provide a comprehensive understanding of BL in the presence of surface coatings to illustrate whether or not it is beneficial to coat transmission components made of AISI 52100-grade steel, such as planetary gears, when aiming to lower the COF under BL.

Table 2-2: DLC types [34]

Coating type	Deposition method	Layer structure	Thickness (μm)	Adhesion-promoting interlayer
DLC-1	RF PACVD (13.56 MHz)	a-C:H single layer	1.78± 0.09	Si-based interlayer
DLC-2	Hybrid process PVD/CVD	a-C:H single layer	2.67± 0.04	TiN interlayer
Ti-DLC	Hybrid process: reactive magnetron sputtering + PACVD	Ti-C:H single layer	2.38± 0.29	Gradual Ti-interlayer
W-DLC	Reactive magnetron sputtering	a-C:H/a-C:H-W multilayer	2.61± 0.05	Cr-interlayer/ WC-layer
Si-DLC	Low-frequency PACVD	a-C:H/a-Si:O single layer	2.36± 0.08	Si-based interlayer

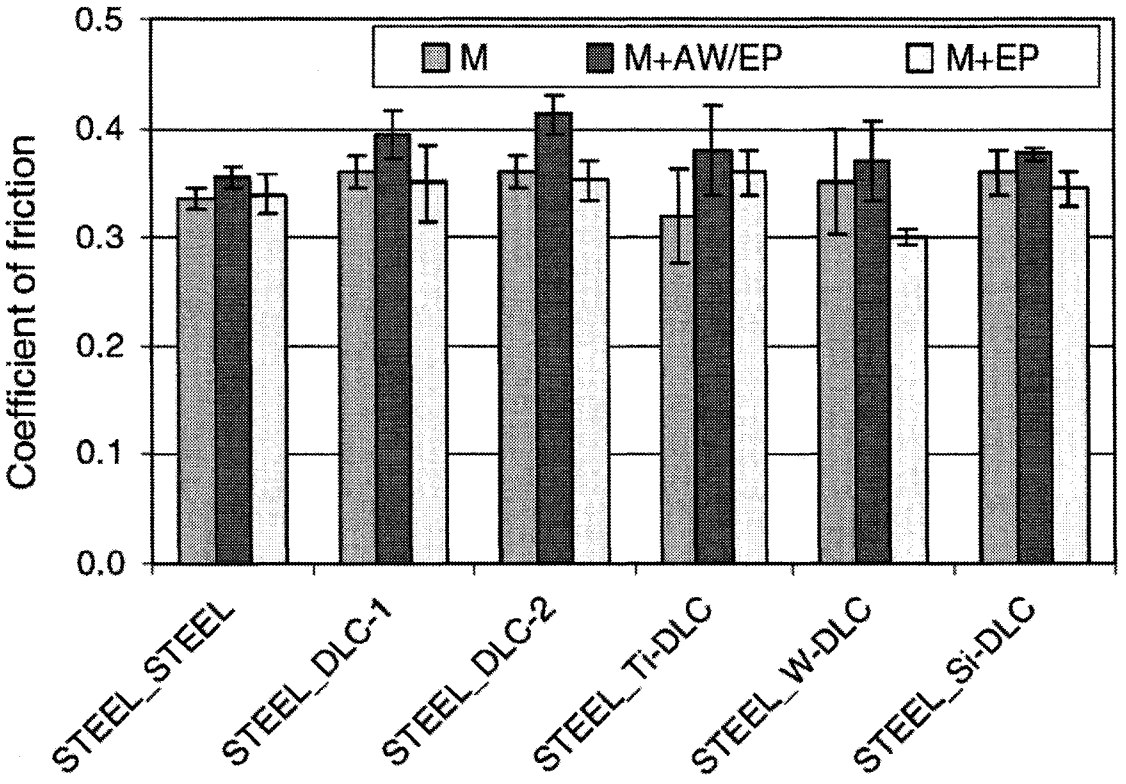

Figure 2-30: COF of 52100 steel sliding against DLC coatings under boundary lubrication with 10 n load and 0.1 m/s [34].

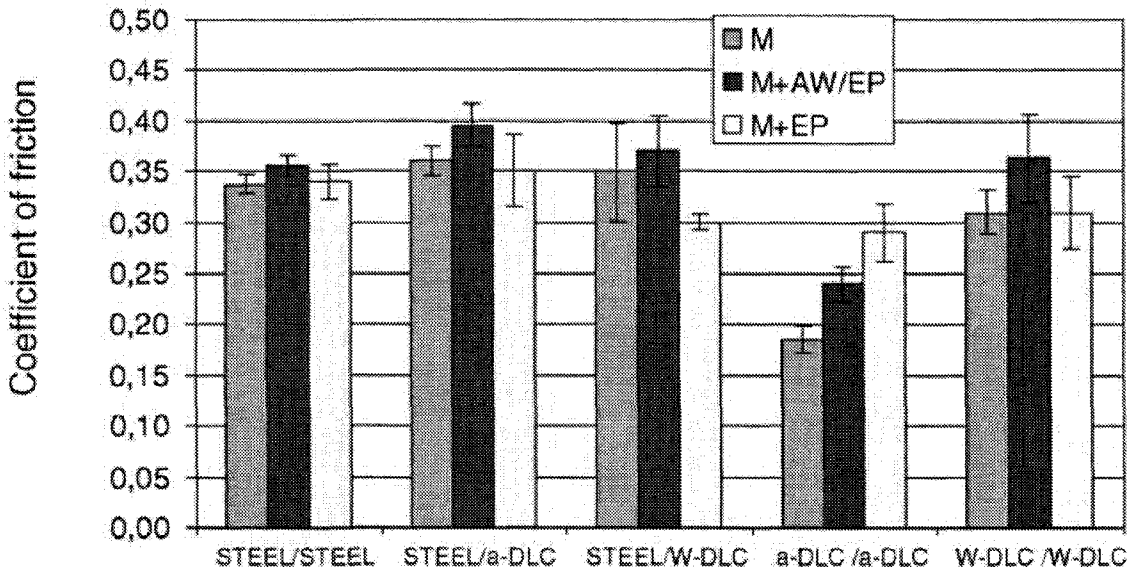

Figure 2-31: COF for (Steel/steel, Steel/a-DLC, Steel/W-DLC, a-DLC/a-DLC and W-DLC/W-DLC) with various oils, Mineral Oil (M) , Mineral Oil+ Anti wear /Extreme pressure (M+ AW+EP) and Mineral Oil+ Extreme Pressure (M+EP) at 10 n load and 0.1 m/s [35].

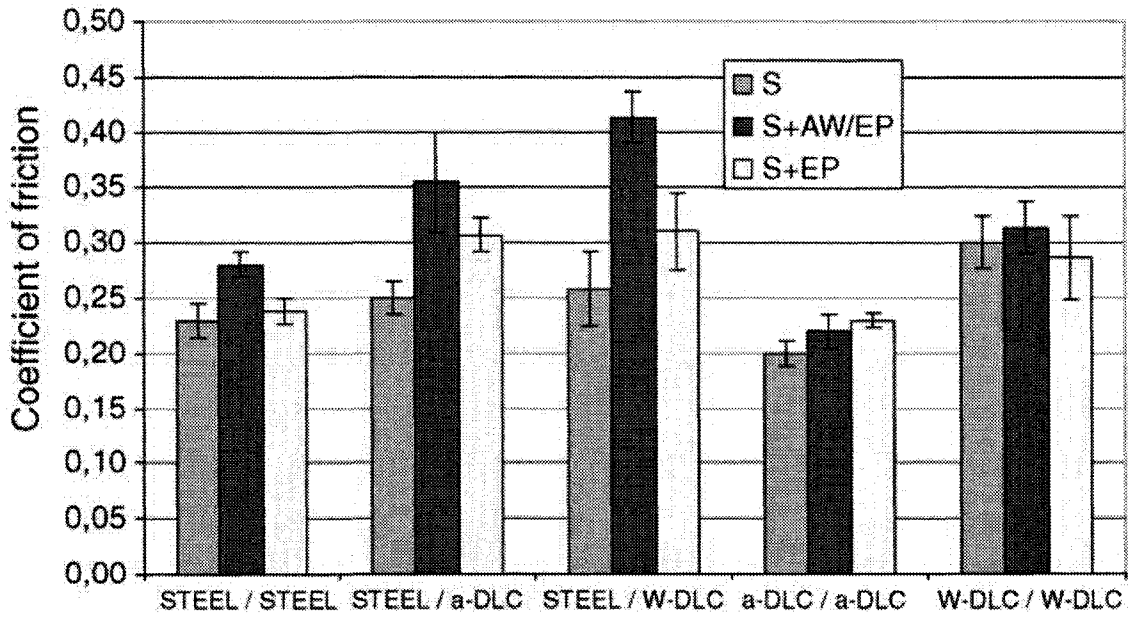

Figure 2-32: COF for (Steel/steel, Steel/a-DLC, Steel/W-DLC, a-DLC/a-DLC and W-DLC/W-DLC) with various oils, Sunflower Oil (S) , Sunflower Oil+ Anti wear /Extreme pressure (S+ AW+EP) and Sunflower Oil+ Extreme Pressure (S+EP) at 10 n load and 0.1 m/s [35].

CHAPTER 3

Experimental Procedures

This chapter describes the materials used, as well as the analyses techniques and testing equipment applied in this study.

3.1 Materials

3.1.1 DLC Coatings

H-DLC and NH-DLC were picked for this study because they are commonly used by industry as protective coatings for drill bits and to identify the benefits of hydrogen on DLC coatings. Both coatings were deposited on M2 steel discs (Ø 25 mm) by Teer Coatings Ltd. by a closed-field, unbalanced magnetron PVD sputtering system described in Section 2.1.2. The PVD system had two chromium target and two graphite targets (Figure 3-1), and approximately 0.6 μm of Cr interlayer was deposited before the NH-DLC coating to promote adhesion to the steel substrate [36]. The power to the Cr target was then decreased gradually while increasing the power to graphite targets to obtain the desired 1 to 1.5 μm thick layer of NH-DLC coating as shown in Figure 3-2 (a). As for the H-DLC coating, a 0.8 to 1 μm Cr interlayer, was followed by a gradual decrease in power to the Cr target during an increase in power to the graphite targets. The process was similar to the NH-DLC deposition procedure, but with the addition of a butane precursor gas to achieve 40 at% of hydrogen content, which resulted in a 0.8-1 μm-thick H-DLC (Figure 3-2 (b)).

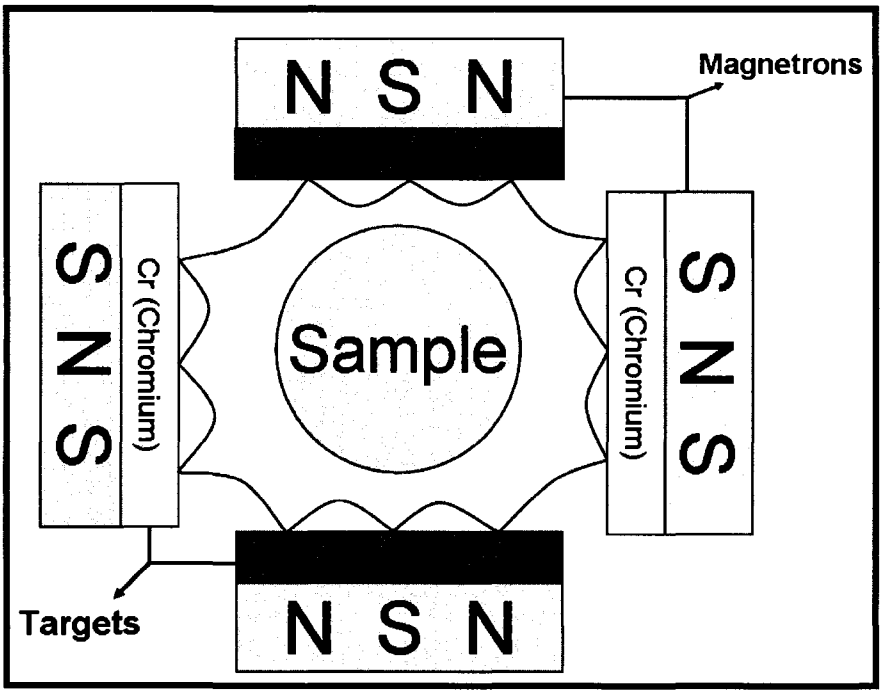

Figure 3-1: Schematics for a closed field, unbalanced magnetron sputtering system [36]

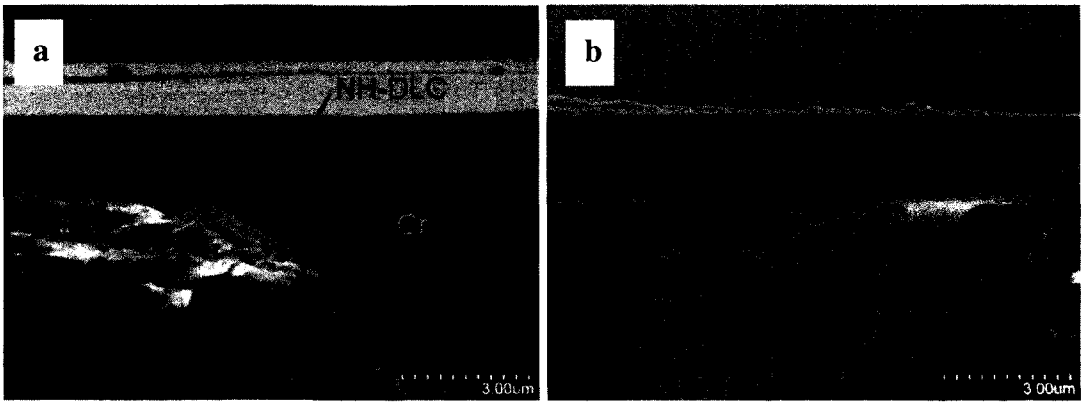

Figure 3-2: Cross section of the (a) NH-DLC and (b) H-DLC coatings after cryogenic fracture

3.1.2 Counterface Materials

Two counterface materials, 319 Al and AISI 52100 were used in this study. 319 Al was chosen for it is widely used in automotive applications due to its lightweight and relatively high hardness of 80 HB [37] compared to pure aluminum. The alloy mainly consists of 6 wt% Si, 4wt% Cu and aluminum, the actual composition of the alloy is presented in (Table 3-1). 319 Al was drawn into a 4 to 5 mm rods at 700 °C and was T5 (200 °C for 8h) heat treated. The rods were then cut to a 15 mm length and one end of the pin was rounded to a 4 mm Ø. 319 Al pins were run as a counterface material against the DLC coatings to study the friction behaviour under dry sliding.

The second counterface was AISI 52100 steel, with a hardness of 197 HB [38]. This type of steel is commonly used for ball bearings and transmission gears for its good machinability. AISI 52100 steel was purchased in the form of 6 mm Ø balls, which were also run as counterface materials against the DLC coating. The chemical composition of AISI 52100 steel is presented in Table 3-2.

Table 3-1: Chemical composition of SAE 319 Al [37]

319 Al										
Element	**Cu**	**Mg**	**Mn**	**Si**	**Fe**	**Zn**	**Ti**	**Ni**	**Others**	**Al**
Composition [wt%]	3.00-4.00	0.1	0.5	5.50-6.50	1	1	0.25	0.35	0.5	Balance

Table 3-2: Chemical composition of AISI 52100 steel and AISI M2 steel [38]

	Composition [wt%]										
Element	**C**	**Mn**	**P**	**S**	**Si**	**Cr**	**Ni**	**Mo**	**W**	**V**	**Fe**
52100 steel	0.98-1.10	0.25-0.45	0.025	0.025	0.15-0.35	1.30-1.60	-----	-----	-----	-----	Balance
M2 steel	0.78-0.88	0.15-0.40	-----	-----	0.20-0.50	3.50-4.00	0.30 max	8.20-9.20	1.40-2.10	1.00-1.25	Balance

3.2 Material Characterization

3.2.1 Light Microscope

This study used a VHX-600 digital microscope with a large depth of field that proved useful for analyzing surfaces with large height differences. This digital microscope was used to analyze the pin/ball contact area, as well as the wear track after testing, to clearly identify surface features.

3.2.2 Coating Thickness

3.2.2.1 Radial Sectioning

A CALOTEST machine, made by CSM, measured the coating thickness using a radial sectioning method. The surface coating was pressed against a rotating steel ball with a known radius, creating a crater Figure 3-3. The thickness was then determined using the following calculation. The crater depth is represented by *"P"*, which is calculated from the chord of a circle using Equation 3-1. The crater depth, minus the coating thickness, is *"p"*, which was calculated in a way that was similar to the manner shown in Equation 3-2. R is the rotating ball radius, D_{outer} and D_{inner} are the outer and inner diameters of the two concentric circles and T is the coating thickness (calculated using Equation 3-3).

$$P = R - \left(\sqrt{\left(\frac{D_{outer}}{2} \right)^2 - R^2} \right) \qquad \textbf{3-1}$$

$$p = R - \left(\sqrt{\left(\frac{D_{inner}}{2} \right)^2 - R^2} \right) \qquad \textbf{3-2}$$

$$T = P - p \qquad \textbf{3-3}$$

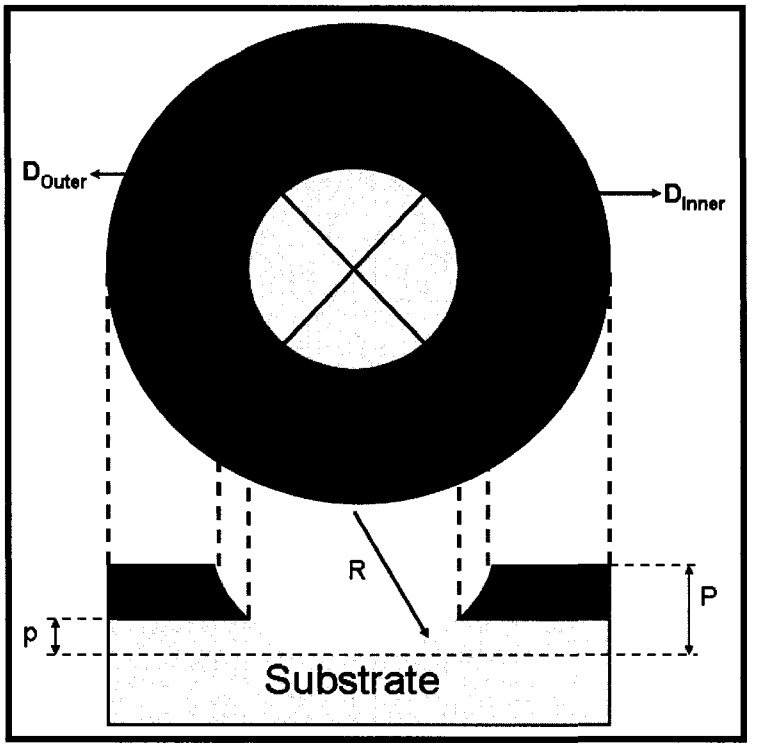

Figure 3-3: Schematics for coating thickness measurement using a CALOTEST

3.2.2.2 Cryogenic Fracture

Another way that coating thickness was measured was by fracturing the coating cryogenically and investigating the cross section of the fractured surface using a scanning electron microscope (SEM). Prior to cryogenic fracture, the specimen was cut from the uncoated side using an electrical discharge machine (EDM) that created a narrow cut (0.6 mm width). The EDM cut did not travel all the way through the disc, but left about 0.5 mm of material from the coated side. The sample was then submerged into liquid nitrogen and fractured by holding the bottom half of the disc with a vice and tapping the coated side with a hammer, which broke the specimen in half.

3.2.3 Mechanical Properties

The TI 900 TriboIndentor, made by Hysitron and equipped with a Berkovich (three sided pyramid) nano-indenter, performed 40 indents on H-DLC and NH-DLC. These indents were less than 200 nm deep from the surface in an effort to eliminate substrate effect on the measurement. Nano-hardness and elastic modulus were calculated from the loading and unloading curves, according to the Oliver and Pharr method [39] described in Appendix C.

3.2.4 Surface Energy

The surface energy of the DLC coatings was determined by the wetability of the surface (Figure 3-4). A water droplet of a 10 μl volume was dropped on the surface coatings (H-DLC and NH-DLC) using a sessile drop machine made by KRUSS. The surface energy (γ) is defined by the following equation:

$$\gamma_{SV} = \gamma_{SL} + \gamma_{LV} \cos\beta \qquad \textbf{3-4}$$

Where γ_{SL} is the surface energy of the solid (S) liquid (L) interface, γ_{LV} is the surface energy of the liquid (L) vapour (V) interface and γ_{SV} is the surface energy of the solid (S) vapour (V) interface. From Equation 3-4, it is understood that as β decreases the γ_{SV} increases.

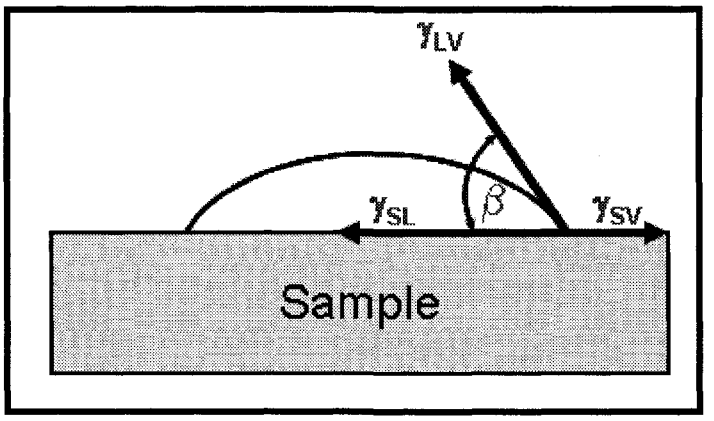

Figure 3-4: Contact angle measurement schematics for water droplet applied to the surface

3.2.5 Chemical Composition

3.2.5.1 X-Ray Diffraction

The composition of the H-DLC and NH-DLC coatings was measured using a Siemens D5000 X-Ray diffraction (XRD) machine. The source incident angle was set to 4° to minimize the X-Ray's penetration depth, and the detector was set to gather the reflected rays from 10° to 100° in 0.04° increments every 2 seconds.

3.2.5.2 Electron Microprobe (EMPA)

The chemical composition of the surface coating was determined by Electron microprobe (EMPA), a non-destructive analytical tool that works like an SEM. Electrons bombard the sample surface to generate X-Rays and elements that are present on the surface are determined from their wave length, while the concentration is calculated from the intensity level.

3.2.5.3 Energy Dispersive X-ray Spectroscopy (EDS)

Energy dispersive X-ray spectroscopy (EDS) is a non-destructive analytical technique used to determine the elemental composition of the sample surface. EDS analyses in this study were obtained while taking SEM micrographs to identify the elemental composition of the transfer layers on the 319 Al pin and the wear debris observed inside the DLC coating's wear track. EDS uses the electron gun present in the SEM that bombards the surface atoms, to excite and eject the inner electrons of the atoms essentially creating a hole. The outer-most electrons then jump down and fill the hole, releasing energy in the form of X-rays as shown in Figure 3-5. The X-rays are then analyzed by the spectrometer to identify which element each atom belongs to.

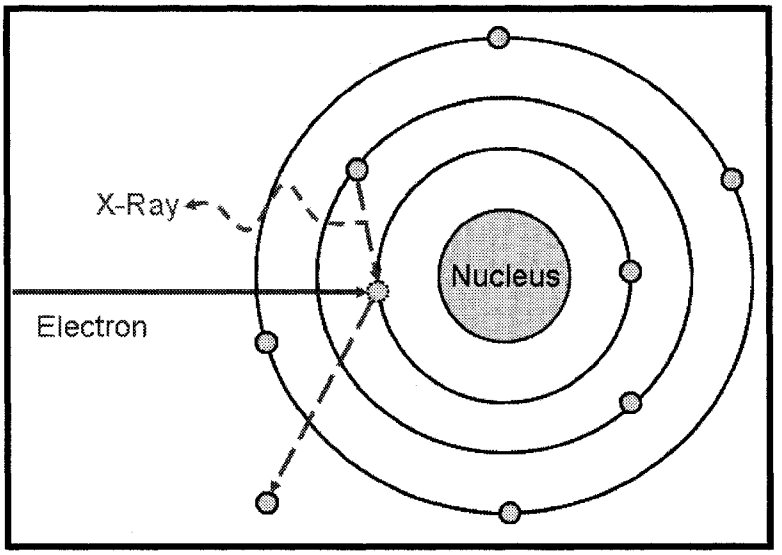

Figure 3-5: Schematics for X-ray generation by electron excitation

3.2.5.4 Elastic Recoil Detection [ERD]

Hydrogen content in the DLC coatings was measured using Elastic Recoil Detection [ERD], which is a nuclear particle accelerator. ERD technique uses He ions, which are accelerated towards the sample, as a result surface molecules are recoiled towards the mass spectrometer, which identifies the recoiled atoms from their atomic weight (Section 3.2.7). The theory behind this technique is based on the conservation of the kinetic energy (Equation 3.5). Where the energy of the He ions (E_o) is equal to the sum of the deflected He ions (E_d) and the recoiled atoms from the surface (E_r). Therefore, the energy of the recoiled atom from the surface is calculated by Equation 3.6, where M_1 and M_2 are the masses of the projectile atom (He) and reflected atoms from the surface respectively, while θ is the recoil angel. The recoil angel can be calculated from Equation 3.7, where ϕ is the deflection angel of He ions as shown in Figure 3-6 [40], [42].

$$E_0 = E_d + E_r \qquad \textbf{3-5}$$

$$E_r = E_0 \frac{4M_1M_2}{(M_1+M_2)} Cos^2\theta \qquad \textbf{3-6}$$

$$Cos^2\theta = \frac{(M_1+M_2)-(M_1Cos\phi \pm \sqrt{(M_2^2 - M_1^2 Sin^2\phi)})^2}{4M_1M_2} \qquad \textbf{3-7}$$

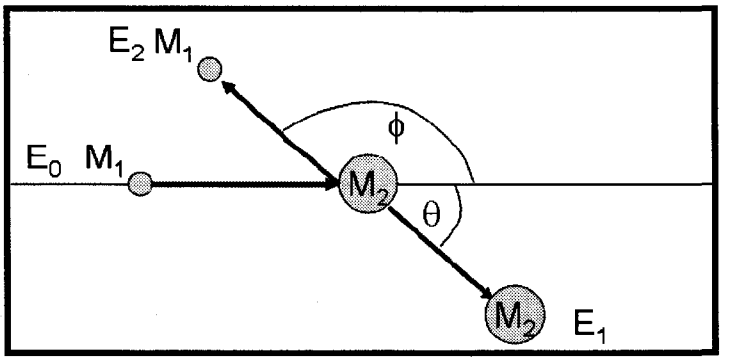

Figure 3-6: Schematics for elastic recoil detection technique

3.2.5.5 Fourier-Transform Infrared Spectroscopy (FTIR)

Infrared (IR) light is divided into three regions according to their wave frequency, i.e. far-IR (5-500 cm^{-1}), mid-IR (500-4000 cm^{-1}) and near-IR (4000-14000 cm^{-1}). Fourier-Transform Infrared (FTIR) spectroscopy uses mid-IR light because most molecular vibration levels fall within 500 and 4000 cm^{-1} frequency. This technique relies on the fact that all molecules absorb IR waves that corresponds to their natural vibration frequency and what is not absorbed is reflected to the detector. Absorbance is then calculated from the reflected frequencies, using Beer-Lambert Law (Equation 3.8), which correlate absorbance to reflectance. The reason it is called Fourier transform IR, because data are gathered in the form of absorption vs time. Therefore, Fourier transform operation is applied to transform the data to absorption vs frequency plot, so that the type of bond and species can be identified by the infrared frequency, which is absorption upon exposure to the IR (Figure 3-7) [41]. In this study, FTIR was utilized to identify the chemistry of the transfer layers found on the 319 Al after sliding against NH-DLC.

$$Absorbance = 1/\log[\mathrm{Re}\, flec \tan ce] \qquad \textbf{3-8}$$

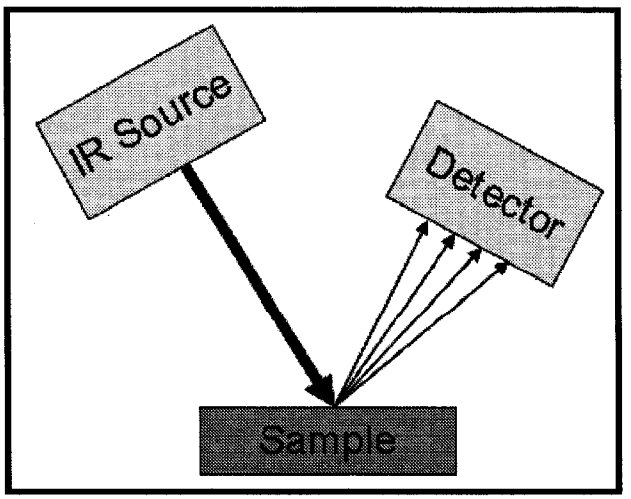

Figure 3-7: Schematics for FTIR spectroscopy

3.2.6 Surface Profilometry

Surface topography of the samples was measured with an optical surface profilometer, which was also used for wear rate calculations. Optical surface profilometry provides non-destructive measurements of surface roughness, width and depth of the wear track, that was later used in wear rate calculations. The profilometer operates in two modes; VSI (Vertical Scanning Interference) used for rough surfaces up to 1mm and PSI (Phase Shift Interference) used on smooth surfaces up to 150 nm.

The machine operates by reflecting beams of white light off the sample surface that intercept each other, forming fringes (altering light and dark bands) when the image is focused on a plane (Figure 3-8). In VSI mode, the machine measure fringe consistency, but in PSI mode, a piezoelectric transducer (PZT) moves the objective downwards, leading to a shift in the fringes when the focus moves to other planes. Data is then recorded and compiled, producing an image [43].

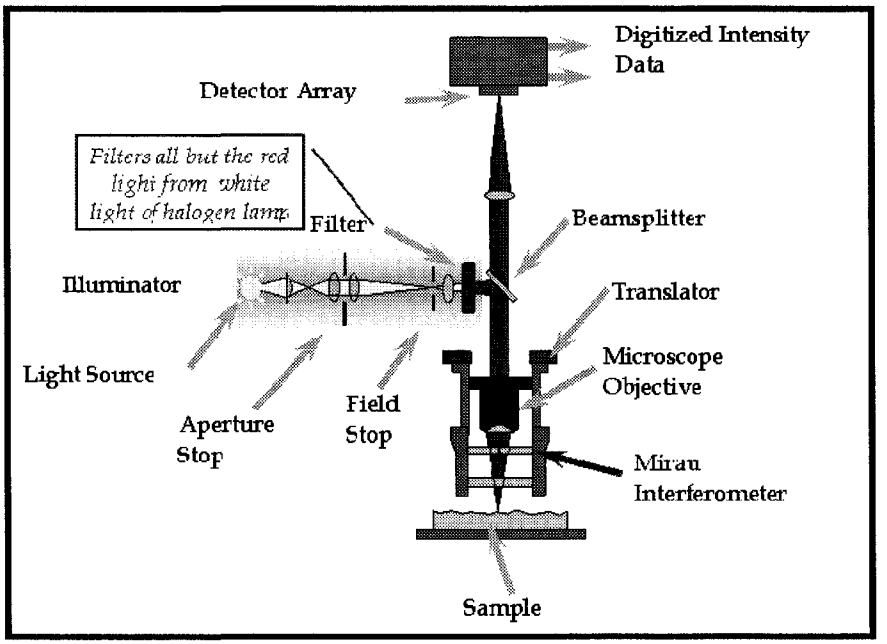

Figure 3-8: Schematics for optical surface profilometer [43]

3.2.7 Residual Gas Analyzer (RGA)

In this study, RGA produced by Hiden was used to measure the residual gases present inside the vacuum chamber. The RGA consist of an electron gun, which produce an electron beam and ionizes gas molecules inside the chamber. Because the electron beam is produced by a hot filament, the RGA can only operate at low pressures (0.05 Pa or $4x10^{-4}$ Torr), since reactive species such as oxygen would destroy the filament.

The ionized gas species are then analyzed by a quadruple mass spectrometer, which identifies the species from their atomic mass. The quadruple mass spectrometer consists of four conductive rods with direct current (DC) and alternating current (AC) running through them. The ions then oscillate between the rods due to the electric field between the rods, the mass of the ions is then determined from their oscillation by an ion sensor (Figure 3-9) [44].

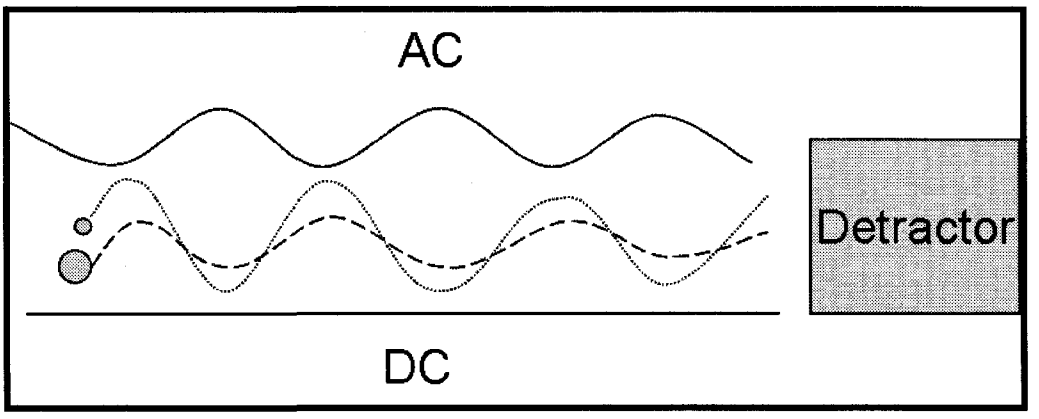

Figure 3-9: Schematics for ion oscillation between the four rods of the Quadruple mass spectrometer

3.3 Tribological Tests

3.3.1 Dry Sliding Tests

A high vacuum/high temperature CSM pin-on-disc tribometer (Figure 3-10) measured the friction force between the mating surfaces (319 Al and DLC surface coatings). The tribometer is equipped with mechanical and turbo pumps, allowing the system to reach vacuum levels as low as 7.5×10^{-8} torr (1×10^{-7} Pa). The machine is also equipped with a residual gas analyzer (RGA described in Section 3.2.7) that identifies gas species inside the chamber during high vacuum experiments (Figure 3-11). All tests were conducted at 5 N load and a 0.1 m/s linear speed.

This study compared the tribological behaviour of 319 Al sliding against H-DLC and NH-DLC in ambient air (40% RH) and in vacuum (0.04 Pa or 3×10^{-4} torr, where RGA is operational) for 5000 sliding cycles was compared. The effect of humidity on NH-DLC was also explored by running three separate tests of 319 Al against a NH-DLC coating for 5000 sliding cycles at 25%, 40% and 77% RH.

The effect of the initial atmosphere on the COF in vacuum was also investigated, when 319 Al slid against NH-DLC for 1500 sliding cycles in ambient air (25% RH), dry air, dry nitrogen and dry oxygen environments. Then chamber was then evacuated while the test was running to observe the COF changes during the transition from the initial atmosphere to vacuum.

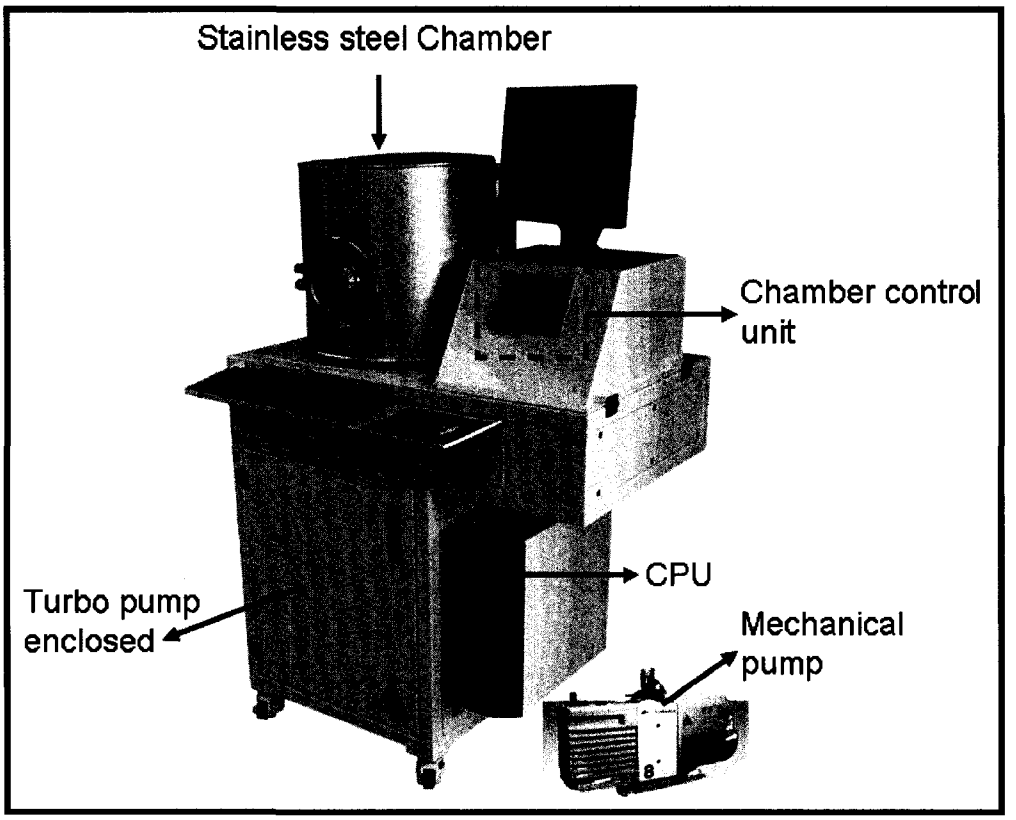

Figure 3-10: CSM high temperature/vacuum tribometer

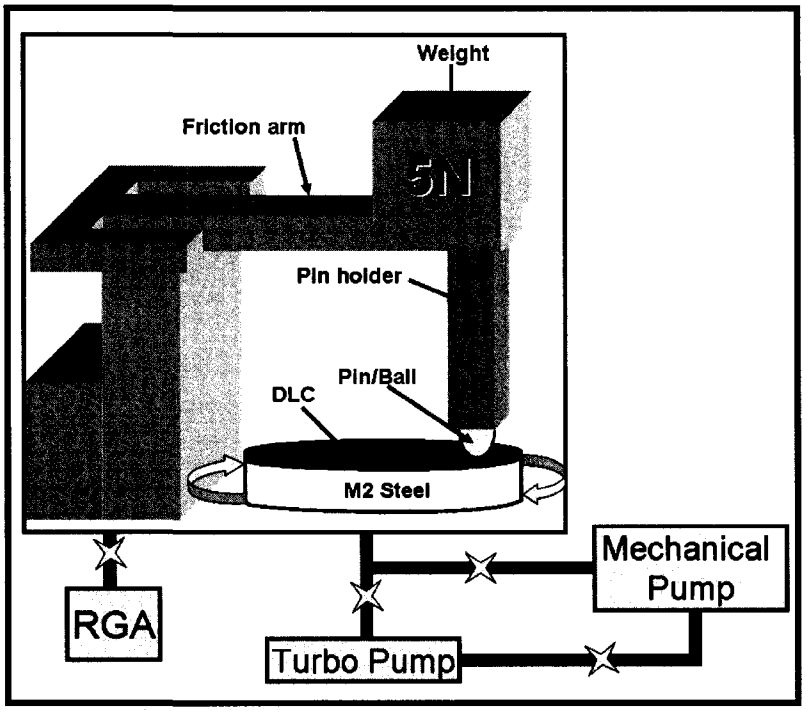

Figure 3-11: Schematic for CSM high vacuum/temperature tribometer with a residual gas analyzer (RGA)

3.3.1 Lubricated Sliding Tests

Lubricated sliding tests were conducted using a CSM bench tribometer (Figure 3-12) that measured the COF of AISI 52100 steel ball sliding against uncoated AISI 52100 steel, H-DLC and NH-DLC surface coatings.

An automatic transmission fluid (ATF), specifically Mobil 1 Dexron III fluid (34 cSt @ 40°C) [45] was used as a lubricant in this study to mimic transmission operation. ATF is a mixture of natural and synthetic oils with 10-20% additive content. Natural oils could be vegetable oils or lard oil, while synthetic oils would include hydrocarbon oils such as oligomerized, polymerized and interpolymerized olfines. As for the additives, they are broken into 8 groups such as viscosity modifiers, dispersants, detergents, anti-wear, oxidation inhibitors, corrosion inhibitors, anti foam and friction modifiers described in Appendix B.

First, the Stribeck curves were generated for three couples; 52100 steel against 52100 steel, 52100 steel against H-DLC and 52100 steel against NH-DLC couples to identify the lubrication regimes. The curves were generated by testing each couples at various speeds (0.5, 1.0, 10.0, 100.0, 200.0, 500.0 and 600.0 mm/s) while maintaining the constant 5 N load for only 150 sliding cycles at each speed. The average COF value for each speed was used to plot the Stribeck curve.

Two of the couples, 52100 steel against H-DLC and 52100 steel against NH-DLC were tested at 10 cm/s, 5 N load in dry ambient conditions for 4000 sliding cycles, at which point Dexron III was added. The tests were performed to compare the friction behavior of DLC in dry and lubricated sliding and observe the effect of initial run in period in ambient air of lubricated sliding, specifically boundary lubrication.

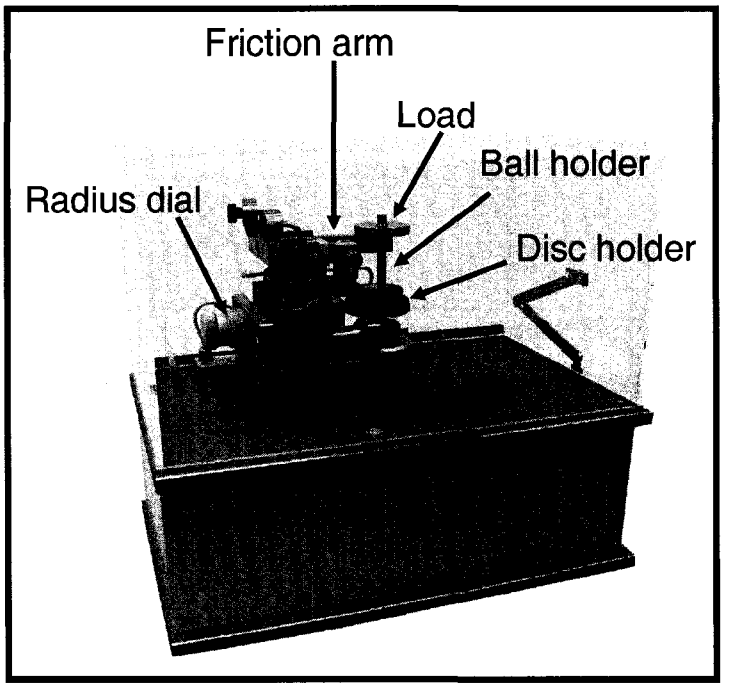

Figure 3-12: Pin on disc bench tribometer

3.3.2 Wear Rate

The wear rate of was calculated according to Archard in 1953, where he introduced the concept of wear rate (W) from a relationship between volume loss (V), sliding distance (d) and load (F).

$$W = \frac{V}{dF} \qquad 3\text{-}9$$

The volume loss of the wear track was calculated by measuring the cross sectional area of the wear track using surface profilometer and multiplying the area with the parameter of the track.

$$V = 2\pi r.(area) \qquad 3\text{-}10$$

As for the ball, the volume was calculated by measuring the wear scar radius (r) and the ball radius (R).

$$V = \frac{1}{6}\pi h[3r^2 + h^2] \qquad 3\text{-}11$$

Where h is the material loss height, as shown in Figure 3-13

$$h = R - \sqrt{R^2 - r^2} \qquad 3\text{-}12$$

In Stribeck curve experiments, the sliding speed was varied and in this case, the wear rate cannot be used compared. Therefore, the wear rate was normalized for speed by dividing the wear rate by sliding speed (v) for comparison.

$$W = \frac{V}{dFv} \qquad 3\text{-}13$$

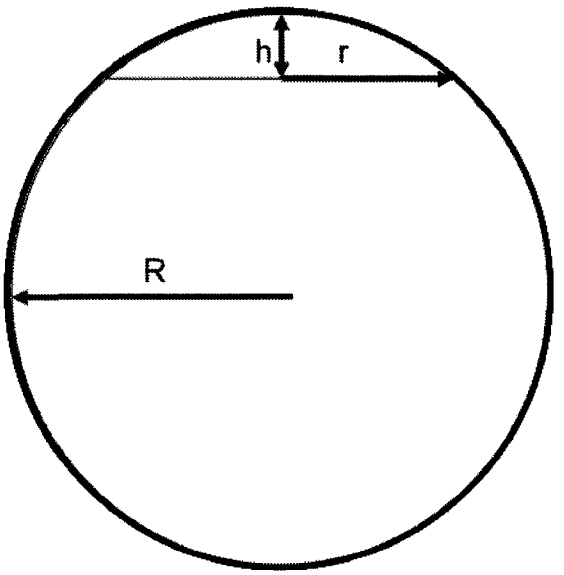

Figure 3-13: Schematic for ball parameters used in wear rate calculation

CHAPTER 4: PART I

Dry Sliding

This chapter presents material characterization results and explore dry-sliding behaviour of H-DLC and NH-DLC coatings in ambient air, vacuum and initial running-in in dry air, oxygen and nitrogen prior to sliding in vacuum.

4.1 Coating Characterization

4.1.1 Coating Thickness

Thickness of both H-DLC and NH-DLC coatings thickness were measured in two ways, radial sectioning (CALOTEST) and the conventional cross-sectioning of the coating. In radial sectioning, a 20 mm Ø ball was rotated against the H-DLC and NH-DLC coatings for 20 and 80 seconds respectively at 800 rpm. Two measurements resulted; the thickness of H-DLC was 1.164 ± 0.177 μm, and the thickness of NH-DLC was 1.485 ± 0.134 μm.

Coating thickness was also measured using SEM after cryogenically fracturing the DLC coatings. Figure 4-1 (a) and Figure 4-2 (a) provide micrographs of the fractured H-DLC and NH-DLC surfaces respectively. Figure 4-1 (b), illustrates how the H-DLC coating reaches 0.12 μm with a 0.60 μm chromium interlayer, confirming with the CALOTEST measurement. As for the NH-DLC coating, Figure 4-2 (b) indicates that the chromium interlayer is about 0.30 μm, with a total thickness of 1.30 μm, remaining within one standard deviation of the CALOTEST measurement.

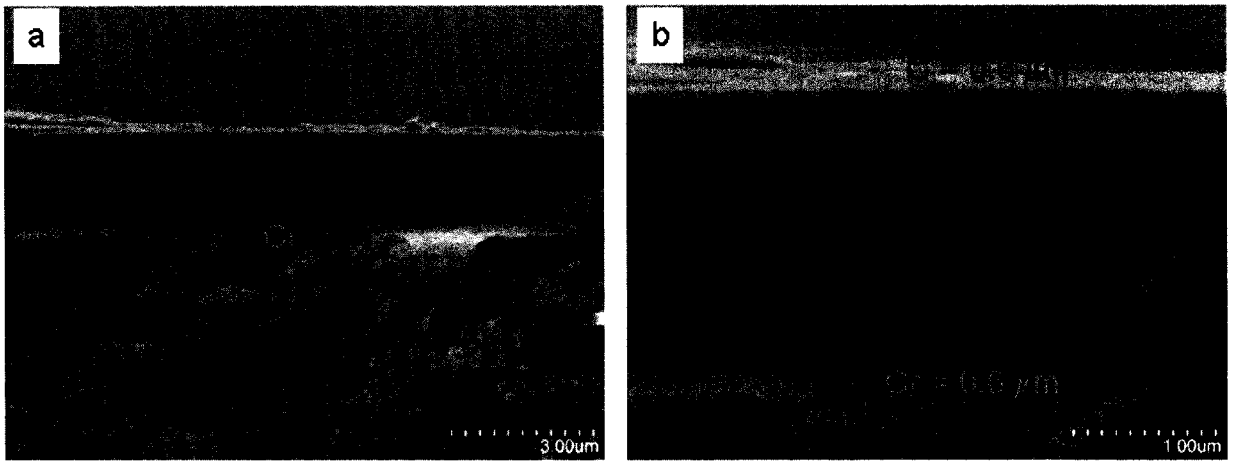

Figure 4-1: Micrographs of the H-DLC cross section (a) illustrates the presence of Cr interlayer (b) indicate that Cr is about as thick as the C coating

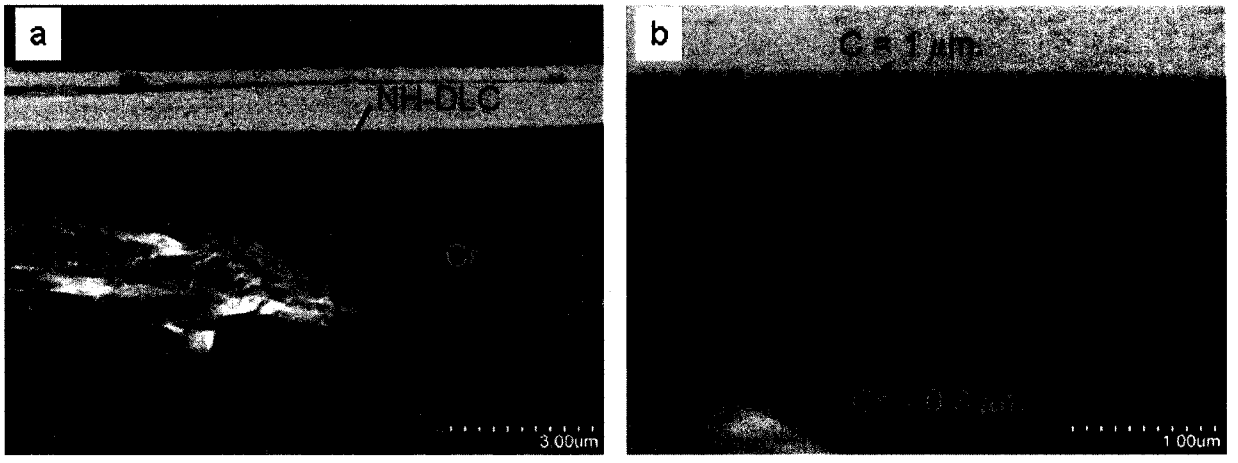

Figure 4-2: Micrographs of the NH-DLC cross section (a) illustrates the presence of Cr interlayer (b) indicate that Cr is liess than half of the C coating

4.1.2 Chemical Composition

4.1.2.1 X-Ray Diffraction

The crystal structure of the surface coating was analyzed by XRD. Figure 4-3 shows the XRD spectra of H-DLC and NH-DLC coatings, both spectras observed to over lap each other. Thus, NH-DLC intensity was offset by 150 counts to compare peak positions with H-DLC. The diffraction patterns for H-DLC and NH-DLC coatings are clearly similar, with no evidence of carbon (Graphite or Diamond) and only Cr peaks observed, indicating that the carbon-based coating was too thin for XRD analysis.

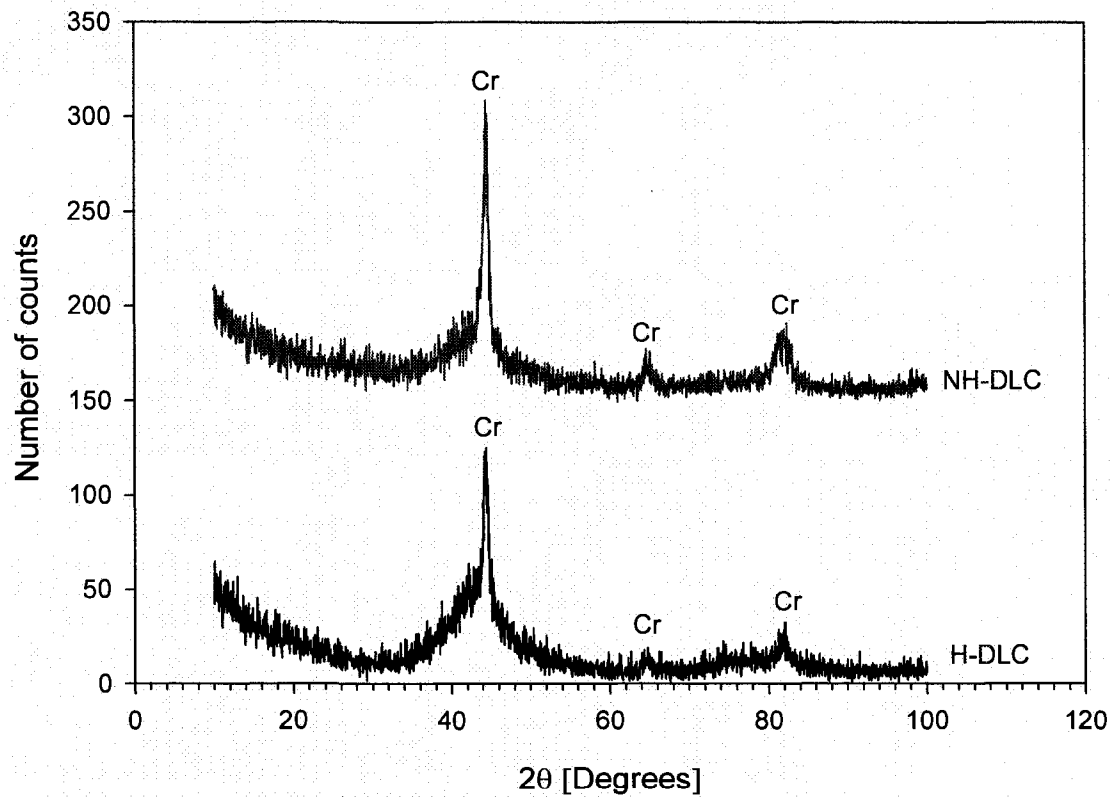

Figure 4-3: XRD spectra of H-DLC and NH-DLC. NH-DLC spectra was offset by 150 counts to compare with the H-DLC spectra

4.1.2.2 Electron Microprobe Analysis

The chemical composition of the DLC coatings was measured using Electron probe microanalysis (EPMA). The microanalysis was conducted on the crater in the H-DLC coating, created by the CALOTEST, producing a backscattered image of the crater (Figure 4-4 (a)). Carbon concentration was 95.5 wt% and Figure 4-4 (b) illustrates how that the concentration decrease from the edge of the crater (top surface) to the bottom of the crater. While Cr concentration is observed to be localized below the carbon coating Figure 4-4 (c), confirming the presence of Cr interlayer with concentration of 4 wt%. As for Fe, Figure 4-4 (d) demonstrates that the concentration is localized at the bottom of the crater, which is the M2 steel substrate. H-DLC EPMA analyses shown in Figure 4-4 (e), illustrate an insignificant Ar concentration, less than 0.5 wt%.

Similarly Figure 4-5 (a) displays the backscattered image of the NH-DLC crater, while Figure 4-5 (b), (c), (d) and (e) provides maps of the C, Cr, Fe and Ar respectively. Carbon concentration (80 wt%) and intensity shown in Figure 4-5 (b) however, was found to be less than the 95.5 wt% observed in H-DLC (Figure 4-4 (b)). While the chromium and argon concentrations in the NH-DLC coating found to be 11 wt% and 9 wt% respectively, which is significantly higher that 4 wt% of Cr and 0.9 wt% of Ar, observed in the H-DLC coating.

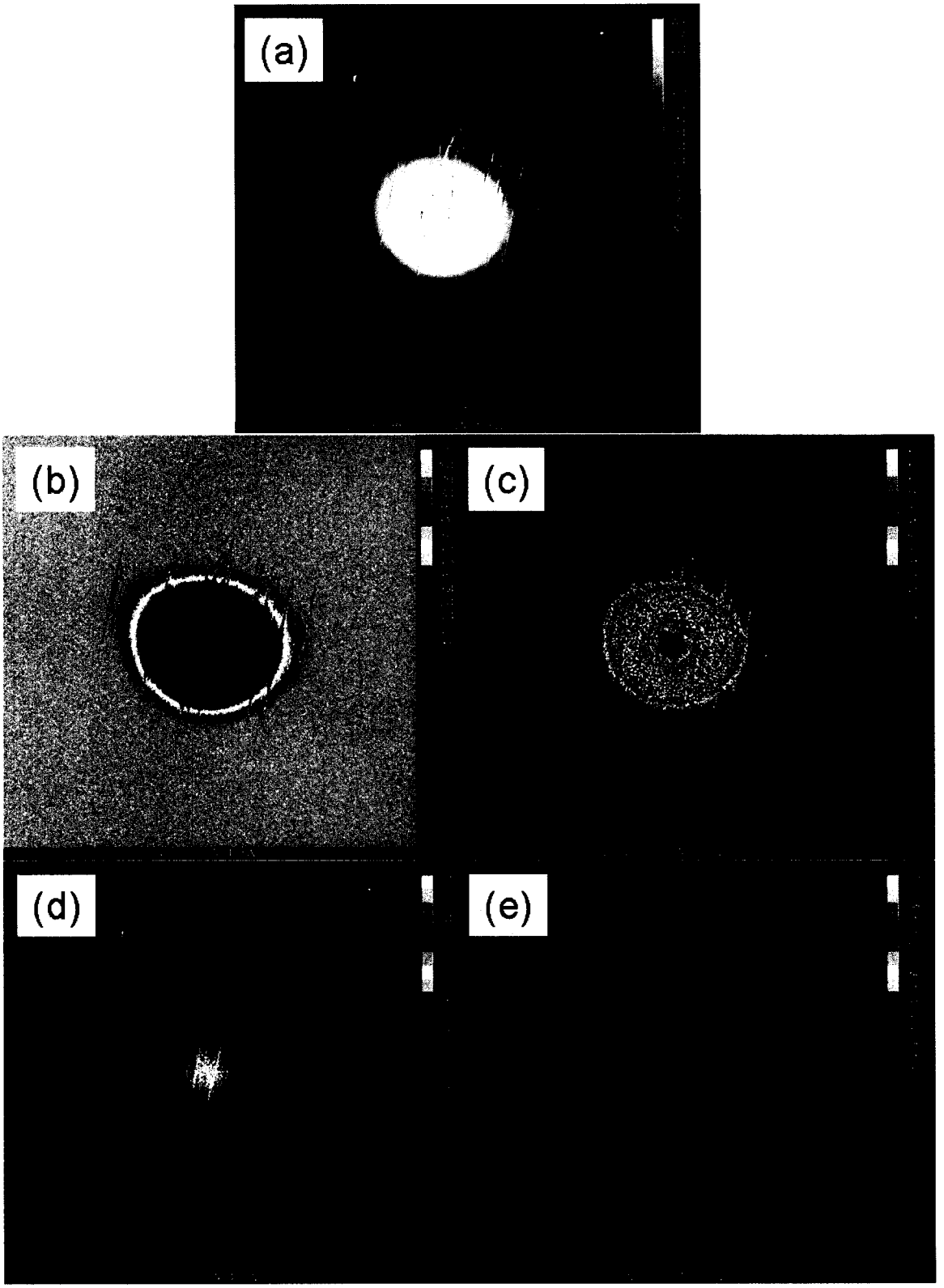

Figure 4-4: EPMA chemical analyses of the H-DLC coating, (a) Back scattered image of the crater, map of (b) Carbon (c) Chromium (d) Iron and (e) Argon

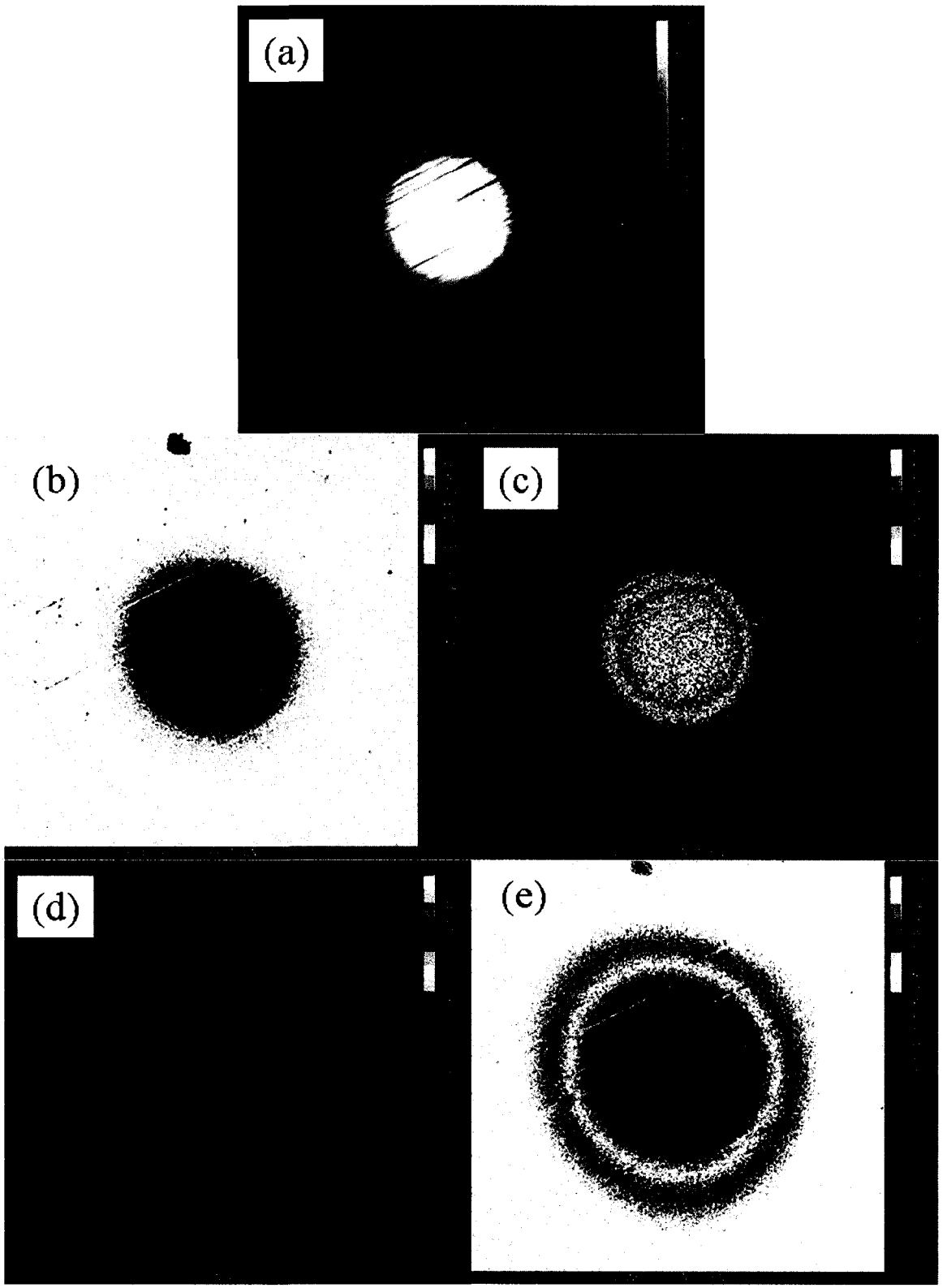

Figure 4-5: EPMA chemical analyses of the NH-DLC coating, (a) Back scattered image of the crater, map of (b) Carbon (c) Chromium (d) Iron and (e) Argon

4.1.3 Mechanical Properties

Hardness and elastic modulus were measured by performing nano-indentation on the coated surface, and calculation procedure is described in Appendix C. Figure 4-6 shows a typical loading and unloading curve of the indentations performed on the H-DLC and NH-DLC coatings. The average of 40 indents performed on the H-DLC coating, result in a hardness average of 11.467 ± 0.835 GPa and an elastic modulus average of 103.319 ± 3.854 GPa. Similarly, for NH-DLC coating the average of 40 indents produced a hardness average of 13.151 ± 1.095 GPa and elastic modulus average of 158.592 ± 6.928 GPa. Calculated hardness and elastic modulus values of the NH-DLC (Graphit-iC) confirm with values from literature [46].

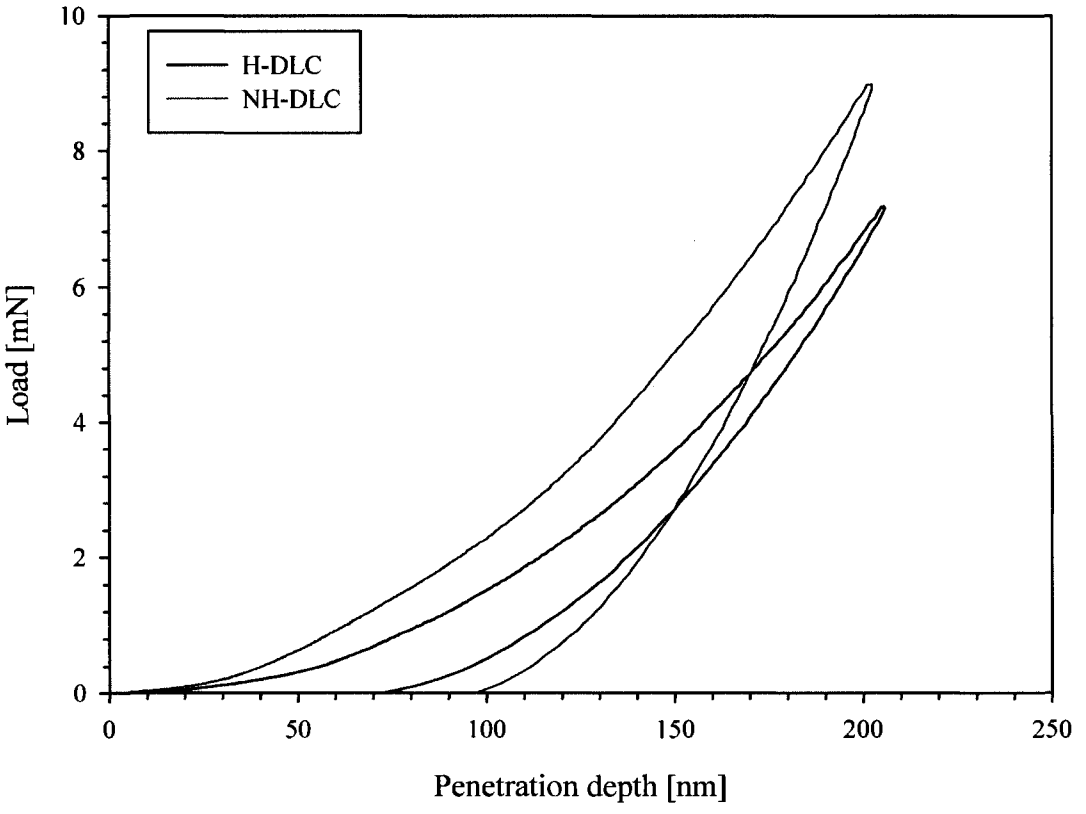

Figure 4-6: Indentation loading and unloading curves for H-DLC and NH-DLC with a Berkovich indentor

4.1.4 Surface Energy

The surface energy was quantified by measuring the contact angle of water and Dexron III oil droplets on the surfaces (Table 4-1). The highest contact angle was observed on the 52100 steel surface at 98.42° (Figure 4-7 (a)), followed by the H-DLC surface at 76.03° (Figure 4-7 (c)) and the lowest angle was observed for the NH-DLC surface at 70.96° as shown in Figure 4-7 (b). Low contact angle according to the surface energy Equation 3-4 represent high surface energy, suggesting that, NH-DLC has the highest surface energy in respect to H-DLC. Implicate that the NH-DLC coating is more reactive when compared to the H-DLC coating, making it more likely to form bonds with water molecules to lower its surface energy.

The results of Dexron III oil, also show that NH-DLC has the lowest contact angle, at 5.90° (Figure 4-8 (b)), indicating high surface energy. The H-DLC surface, it had the highest contact angle at 29.38° (Figure 4-8 (c)), resulting in lowest surface energy. Meanwhile, the 52100 steel surface fell somewhere in between with a 16.94° contact angle as shown in Figure 4-8 (a). Results also confirm that NH-DLC is highly reactive compared to H-DLC, and is more likely to bond with molecules in the oil to lower its surface energy.

Table 4-1: Dihedral angles at room temperature

Surface	Water	Dexron III
52100 Steel	98.42°	16.94°
H-DLC	76.03°	29.38°
NH-DLC	70.96°	5.90°

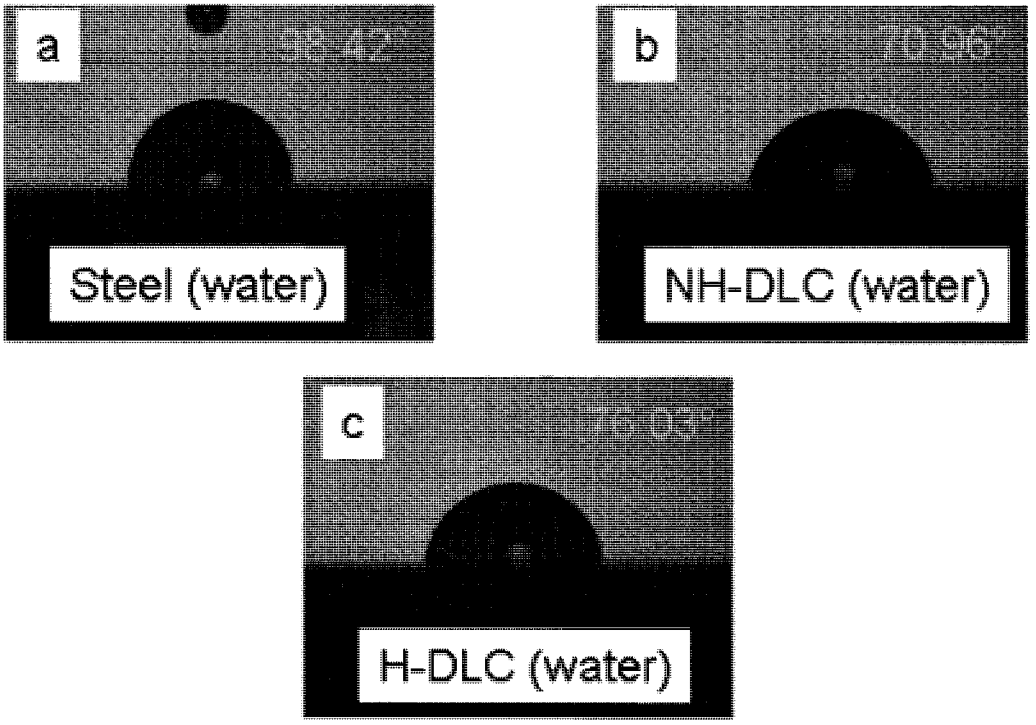

Figure 4-7: Sessile drop results for water droplets on (a) 52100 steel (b) NH-DLC and (c) H-DLC surfaces

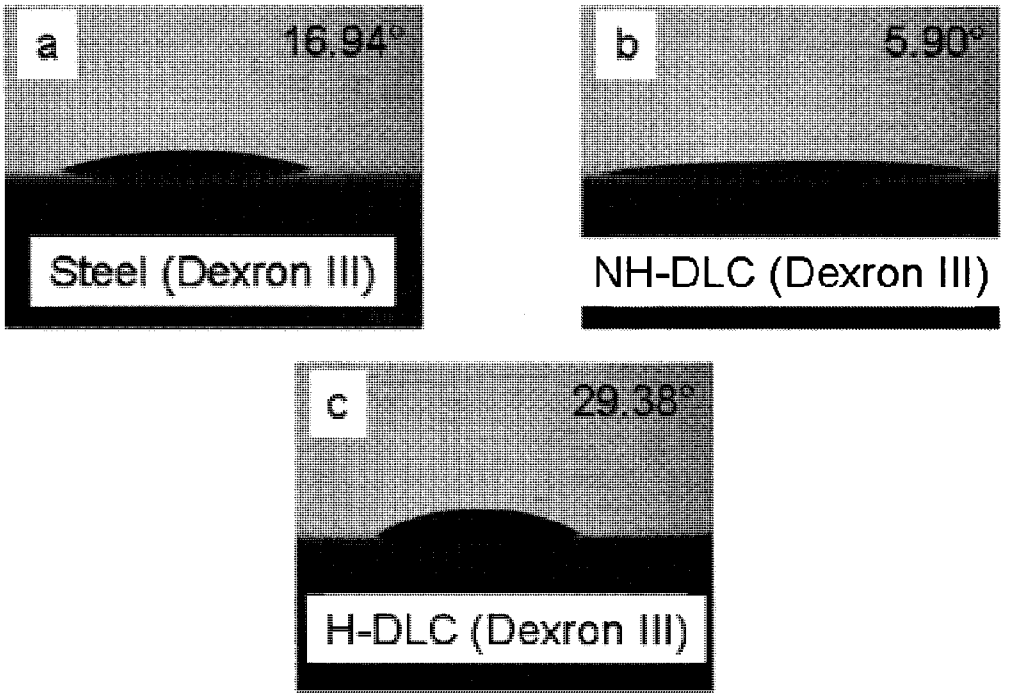

Figure 4-8: Sessile drop results for Dexron III oil droplets on (a) 52100 steel (b) NH-DLC and (c) H-DLC surfaces

4.2 Dry Sliding of 319 Aluminum against DLC Coatings under Various Atmospheric Conditions

4.2.1 NH-DLC and H-DLC Friction in Vacuum

Figure 4-9 illustrates the friction behaviour of 319 Al sliding against NH-DLC and H-DLC with a 5 N load, at a 0.1 m/s speed for 5000 cycles in vacuum at 0.04 Pa ($3x10^{-4}$ torr). The COF of the 319 Al pin sliding against NH-DLC began at 0.45 ± 0.03 for the first 600 cycles, then the friction increased to 0.7 with a high fluctuation of ± 0.2. When the H-DLC coating was tested under the same conditions as the NH-DLC, however, the friction was a very low 0.02 ± 0.01, indicating that the addition of hydrogen to DLC coatings plays a significant role in COF reduction under vacuum.

After the experiments, optical images of the 319 Al pins and the wear tracks were captured. In Figure 4-10 (a), the 319 Al pin ran against NH-DLC is shown to have wore excessively, generating a wear track that is 464.69 μm wide and about 0.6 μm deep, almost half the coating thickness (Figure 4-10 (b)). As for the 319 Al pin that ran against H-DLC, revealed that the tip is covered with material transfer (Figure 4-11 (a)) and a wear track 80 μm wide and about 0.3 μm deep (Figure 4-11 (b)).

Surface profile images of the wear tracks after each experiment illustrate that the NH-DLC coating (Figure 4-12 (a)) is less wear resistant with a wear rate of $1.6x10^{-5}$ mm^3/Nm in vacuum compared to the H-DLC coating's wear rate of $7.6x10^{-7}$ mm^3/Nm (Figure 4-12 (b)). A comparison of Figure 4-12 (a) and (b) it might suggest that H-DLC is the less wear-resistant coating, but since both DLC coatings were tested for different durations, so wear rates give a true indication of wear resistance because they were normalized by distance.

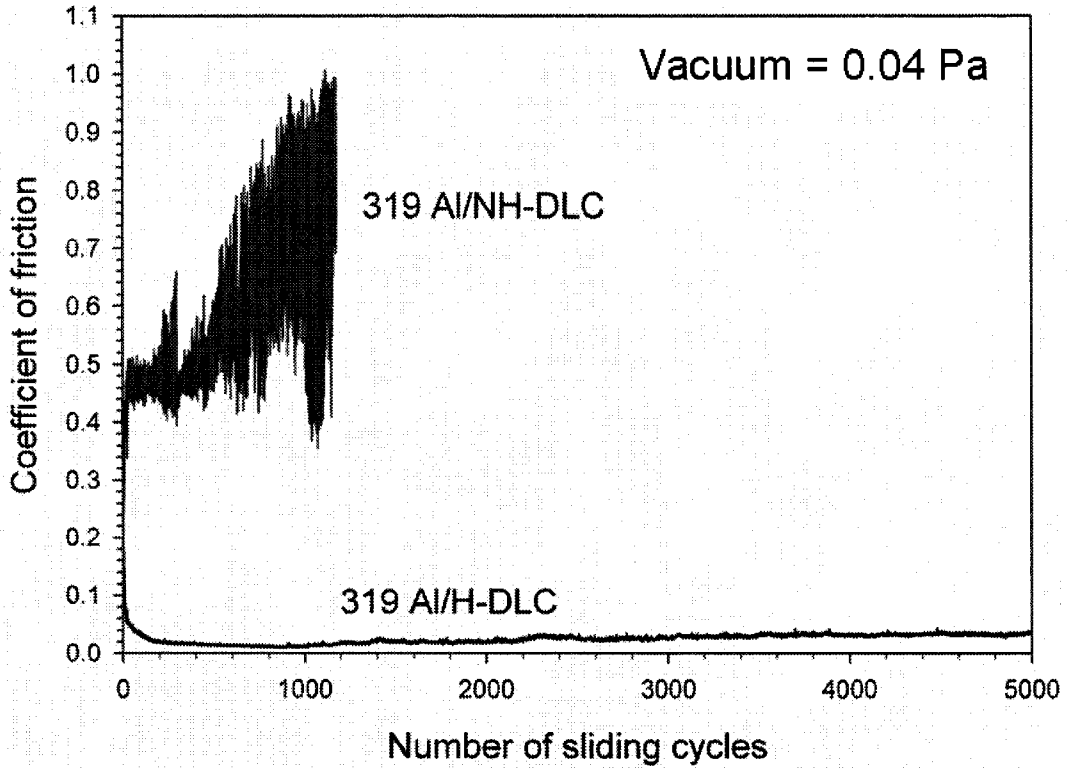

Figure 4-9: 319 Al sliding against H-DLC and NH-DLC at 5 N load and 0.1 m/s linear speed in vacuum (0.04 Pa)

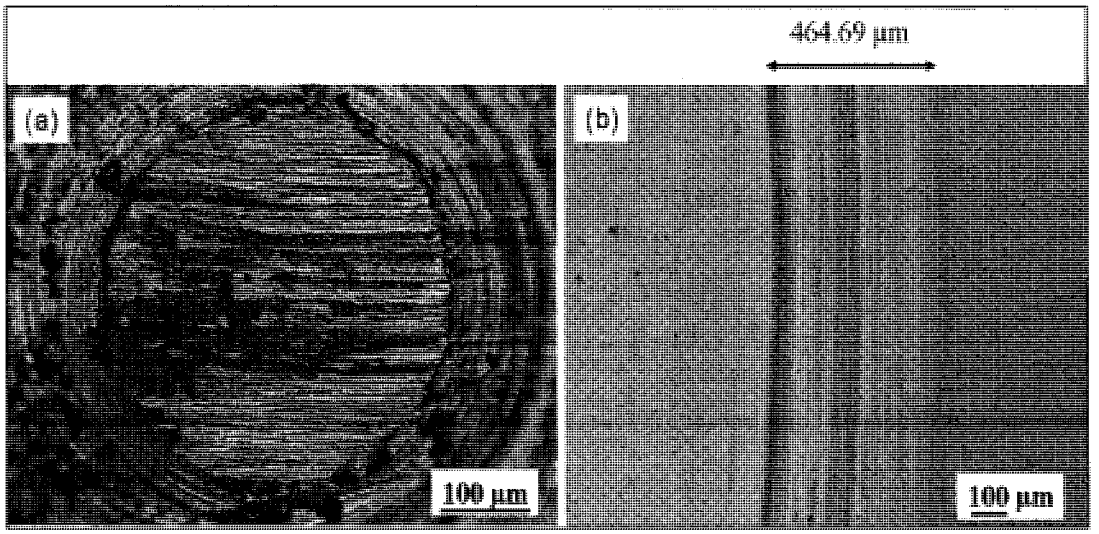

Figure 4-10: Optical microscopy images of (a) 319 Al pin and (b) NH-DLC wear track, after sliding in vacuum for 1200 cycles

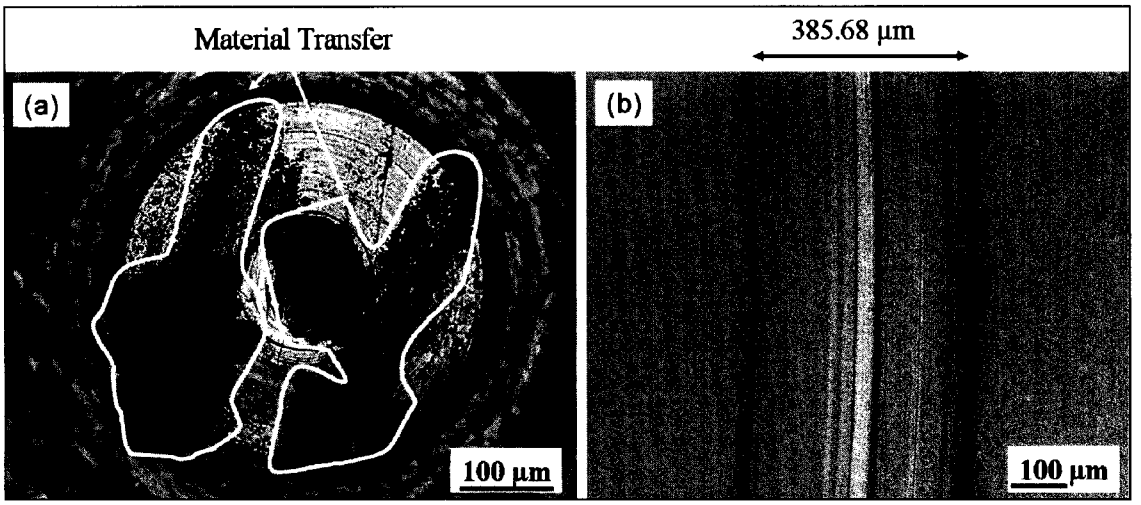

Figure 4-11: Optical microscopy images of (a) 319 Al pin and (b) H-DLC wear track, after sliding in vacuum for 5000 cycles

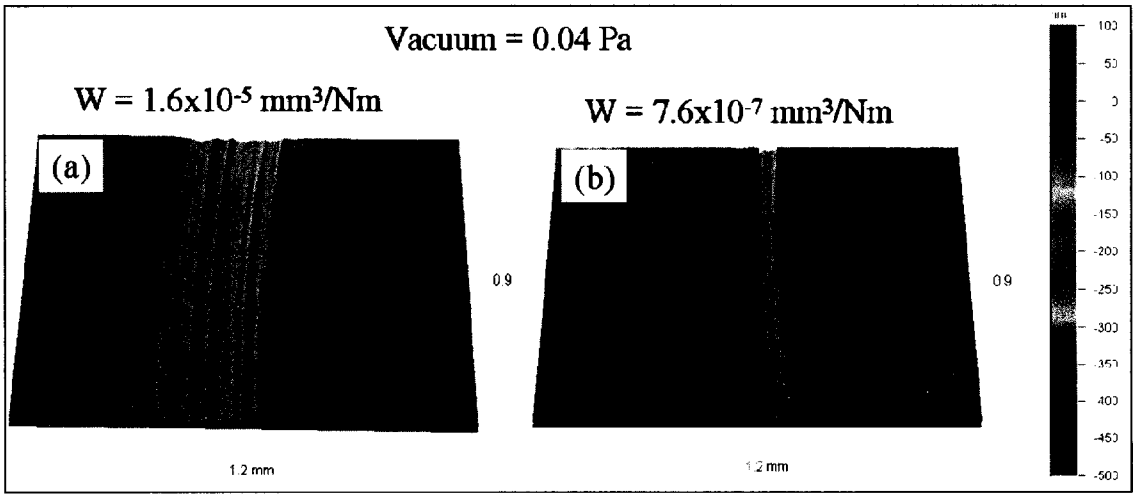

Figure 4-12: Surface profile images of the wear track generated in vacuum for (a) NH-DLC and (b) H-DLC coatings with W as the wear rate, normalized sliding distance

4.2.2 Friction of NH-DLC and H-DLC in Ambient Air

The friction behaviour of NH-DLC and H-DLC in ambient air at 40% RH is completely different than that observed in vacuum. Figure 4-13, shows 319 Al sliding against NH-DLC in ambient air, starting with a run in period lasting 600 cycles with the COF beginning at 0.15 and slightly decreasing to 0.11. After the run in period, the COF increased again, producing a steady-state COF of 0.129 ± 0.015 and at 3000 cycles, the friction slightly decreased to 0.108 ± 0.005. Similar run in behaviour was observed when 319 slid against H-DLC in ambient air (40% RH). The COF initially started at 0.18, then decreased to 0.15 subsequent to the 600 cycles of run in period, with the COF reaching a steady state at 0.21 ± 0.02.

Optical images of the aluminum pin after sliding for 5000 cycles against NH-DLC (Figure 4-14 (a)) reveal that the tip is covered with material transfer and the generated wear track is 411.45 μm wide (Figure 4-14 (b)). Visual inspection of the 319 Al pin, indicated that the material transfer formed by the NH-DLC (Figure 4-14 (a)) covers a relatively larger surface area of the aluminum pin, compared to the material transfer coverage generated on the aluminum counterface by the H-DLC coating (Figure 4-15 (a)). Surface profiles of the wear tracks after the experiments (Figure 4-16), show that the wear rate for the NH-DLC coating is 3.25×10^{-7} mm^3/Nm (Figure 4-16 (a)), which is slightly lower than the wear rate of H-DLC (4.4×10^{-7} mm^3/Nm) shown in Figure 4-16 (b).

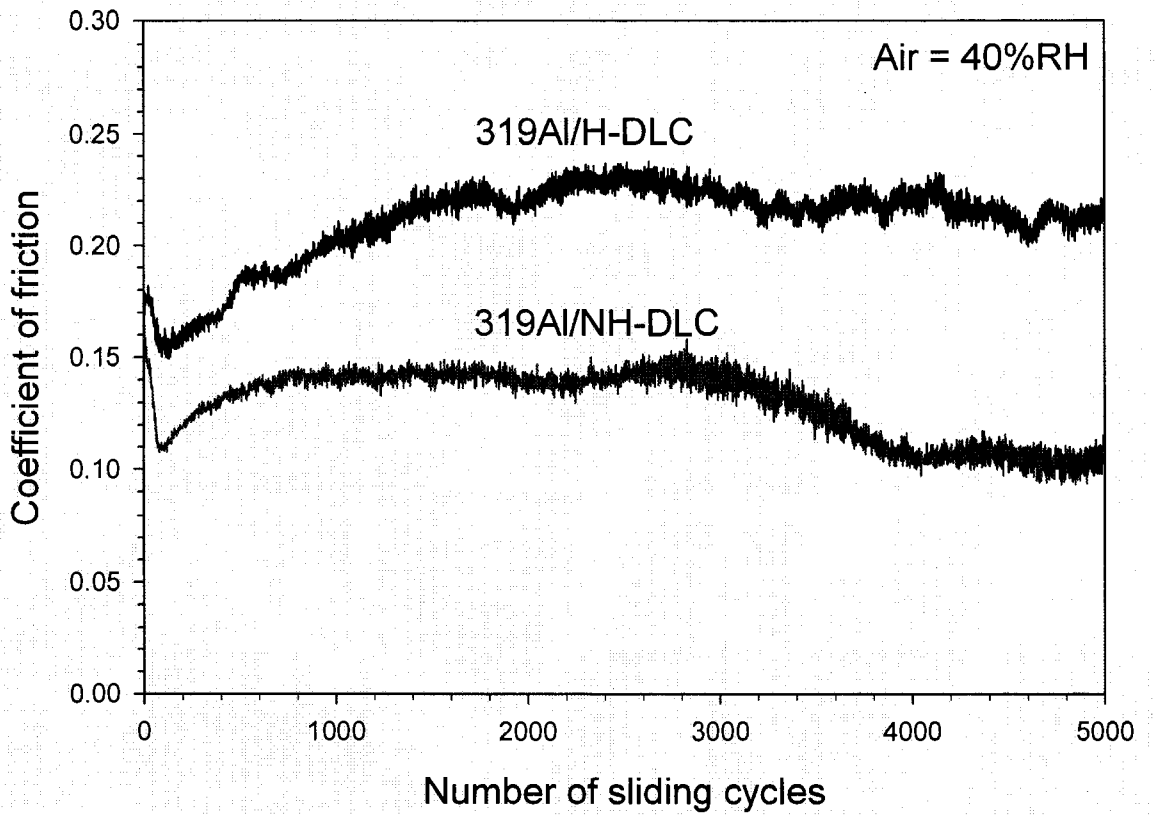

Figure 4-13: 319 Al sliding against H-DLC and NH-DLC at 5 N load and 0.1 m/s linear speed in ambient air with 40% RH

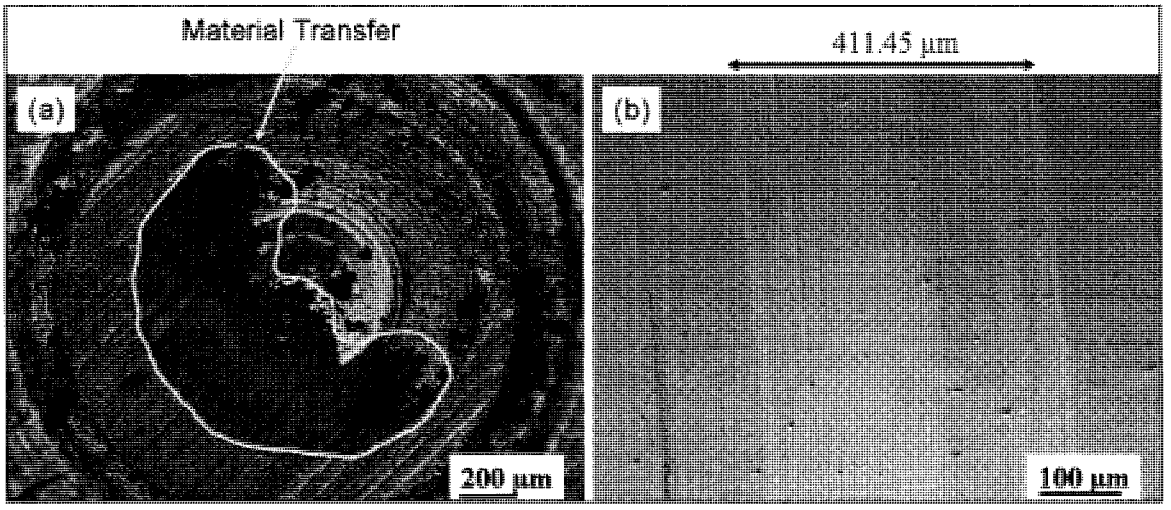

Figure 4-14: Optical microscopy images of (a) 319 Al pin and (b) NH-DLC wear track, after sliding in ambient air for 5000 cycles

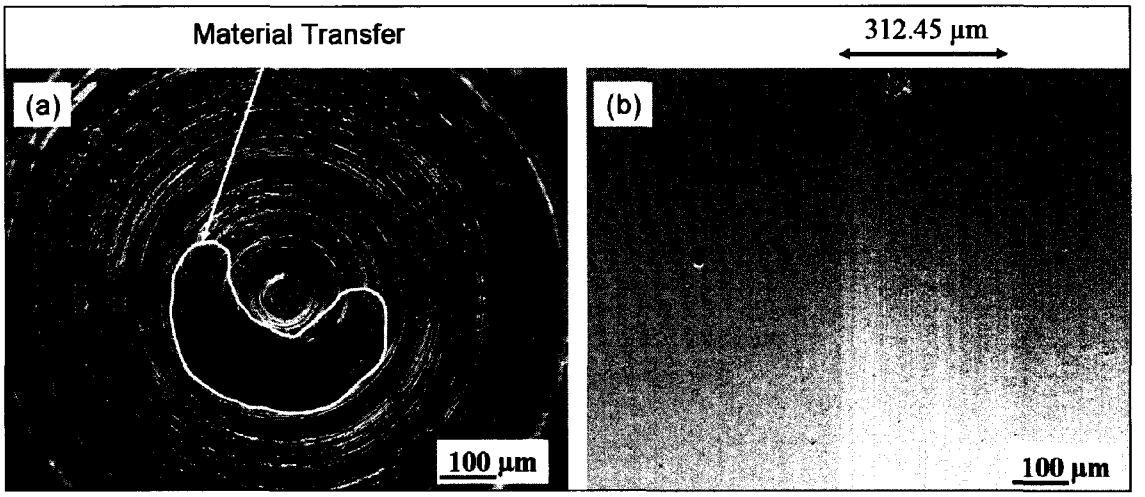

Figure 4-15: Optical microscopy images of (a) 319 Al pin and (b) H-DLC wear track, after sliding in ambient air for 5000 cycles

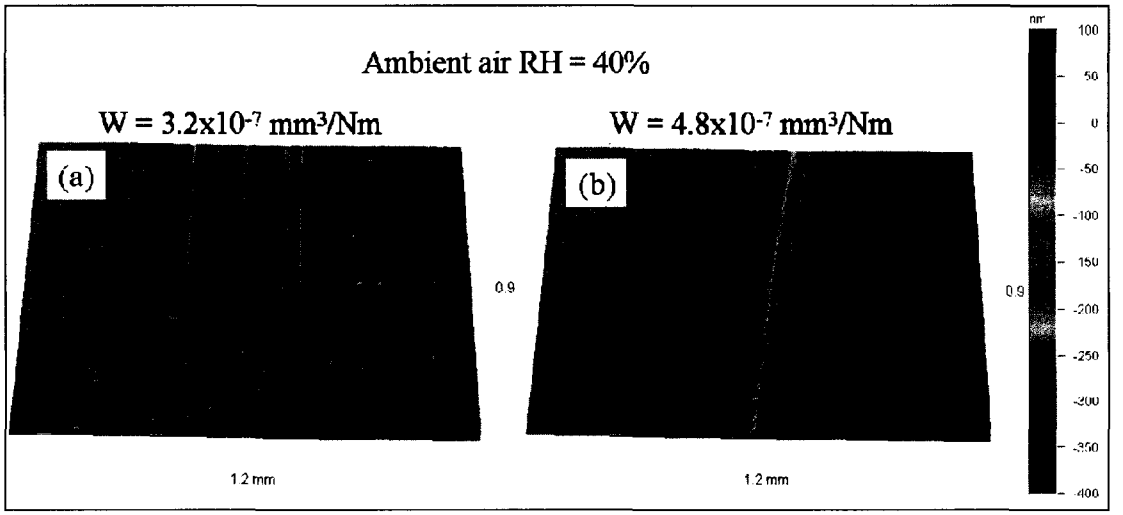

Figure 4-16: Surface profile images of the wear track generated in ambient air for (a) NH-DLC and (b) H-DLC coatings with W as the wear rate, normalized by sliding distance

4.2.3 Friction of 319 Al against NH-DLC at Various Humidity Levels

The experiments conducted in Sections 4.2.1 and 4.2.2, illustrates how friction can be manipulated by changing the testing atmosphere. Consequently, one might wonder what would happen if the humidity was changed, as it might in a real application, where operating atmosphere is constantly changing, for instance in the summer time humidity increase up to 50% RH, while in winter time humidity drops to less than 20% RH. This real-world challenge prompted us to explore the effect of humidity on the friction behaviour of 319 Al sliding against an NH-DLC coating was explored. Pin-on-disc wear tests were performed by sliding the mating surfaces at various humidity levels (22%, 40% and 77% RH) with a 5 N load, at 0.1 m/s for 5000 cycles. Figure 4-17, illustrates how relative humidity has a positive effect on the NH-DLC coating's COF. As the relative humidity increased from 22% to 40% to 77% RH the COF of 319 Al against NH-DLC decreased from 0.19 ± 0.05 to 0.12 ± 0.02 to 0.09 ± 0.01 respectively, this observation confirms with literature [28] and [8].

Optical images of the 319 Al pin after each humidity test (Figure 4-18), illustrate that aluminum pins tested at 22% and 40% RH (Figure 4-18 (a) and (b)) reveal material transfer on the tip, while at 77% RH (Figure 4-18 (c)), no clear evidence of material transfer can be seen in optical microscopy images. The composition of this material transfer, or how it was formed, is currently unknown. Consequently, these aluminum pins were analyzed at a higher magnification using SEM. Micrographs of the aluminum pin tested against NH-DLC at 22% RH (Figure 4-19 (a), (b) and (c)) also reveal material transfer covering the aluminum tip. In Figure 4-19 (d), the pin was tilted to 78°, demonstrating how the material transfer formed a layer covering the contact surface. EDS

was also conducted on the transfer layer as indicated in Figure 4-19 (c), which illustrates that the transfer layer consists of mainly of carbon that can only be generated from the NH-DLC coating. Other peaks, such as aluminum, silicon, copper and oxygen, were also identified. The aluminum, silicon and copper are from the 319 Al pin underneath the carbon transfer layer, while the oxygen is a result of aluminum oxide on the pin.

Material transfer is again confirmed by micrographs of the 319 Al pin tested against NH-DLC at 40% RH, transfer material is again confirmed (Figure 4-21 (a) and (b)). Figure 4-21 (c) illustrates that the material transfer forms stacked layers on the tip of the 319 Al pin. Figure 4-22 (a), (b) and (c) display one of these layers delaminating in a separate area of the pin. A closer look at the layer in Figure 4-22 (d) shows to be about 0.75 μm thick. EDS of the layer (Figure 4-23) captured from Figure 4-22 (c), confirms that these transfer layers consists of carbon with aluminum, silicon, copper and oxygen peaks resulting from 319 Al underneath the carbon transfer layers.

Micrographs of the 319 Al pin tested against NH-DLC at 77% RH, micrographs (Figure 4-24 (a) and (b)) give clear evidence of a carbon transfer layer forming on the tip of the aluminum counterface, despite the lack of proof from the optical image (Figure 4-18 (c)). EDS of this transfer layer shown in Figure 4-25 verifies the presence of carbon, which is transferred from the NH-DLC coating. Micrographs of the NH-DLC coating after the experiment at 77% RH also shows that the wear track is covered with debris (Figure 4-26). EDS analyses (Figure 4-27) reveal that the debris consists of carbon, oxygen, copper, aluminum and silicon. As for other peaks like argon, it is from the coating as confirmed by the EMPA analysis and chlorine is from the water, which was evapourated inside the chamber to increase the humidity.

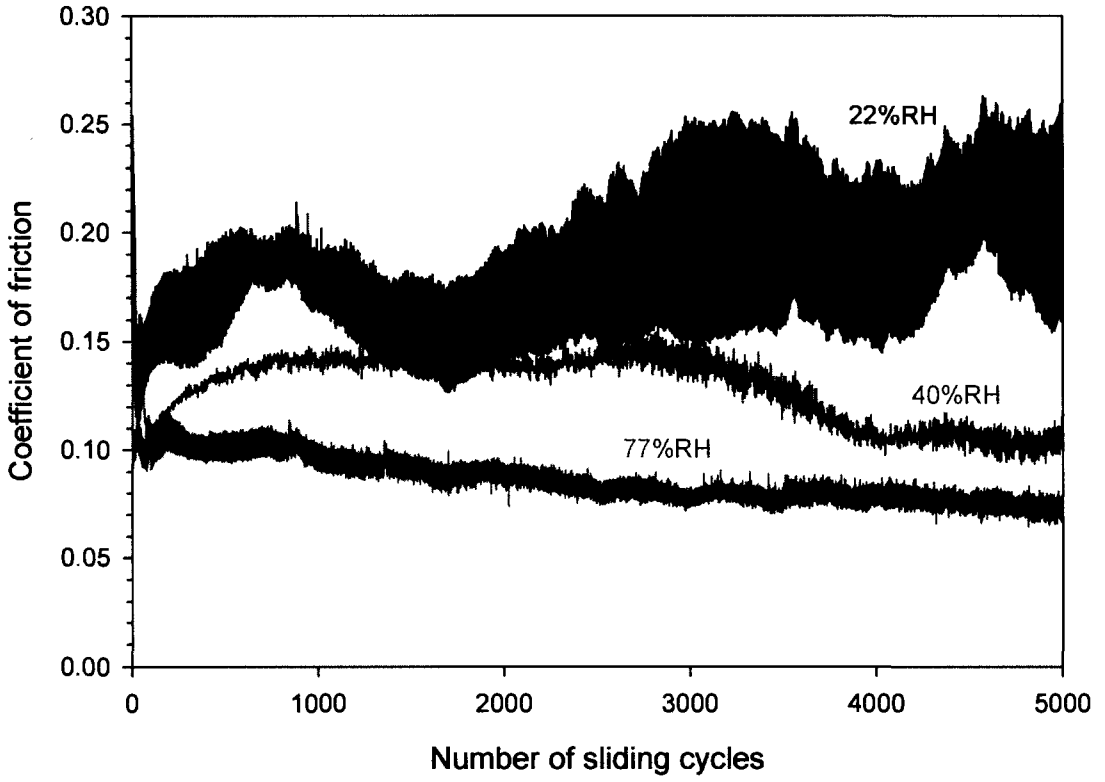

Figure 4-17: Influence of 22%, 40% and 77% RH on the COF of 319 Al sliding against NH-DLC at 5 N load and 0.1 m/s sliding speed for 5000 sliding cycles

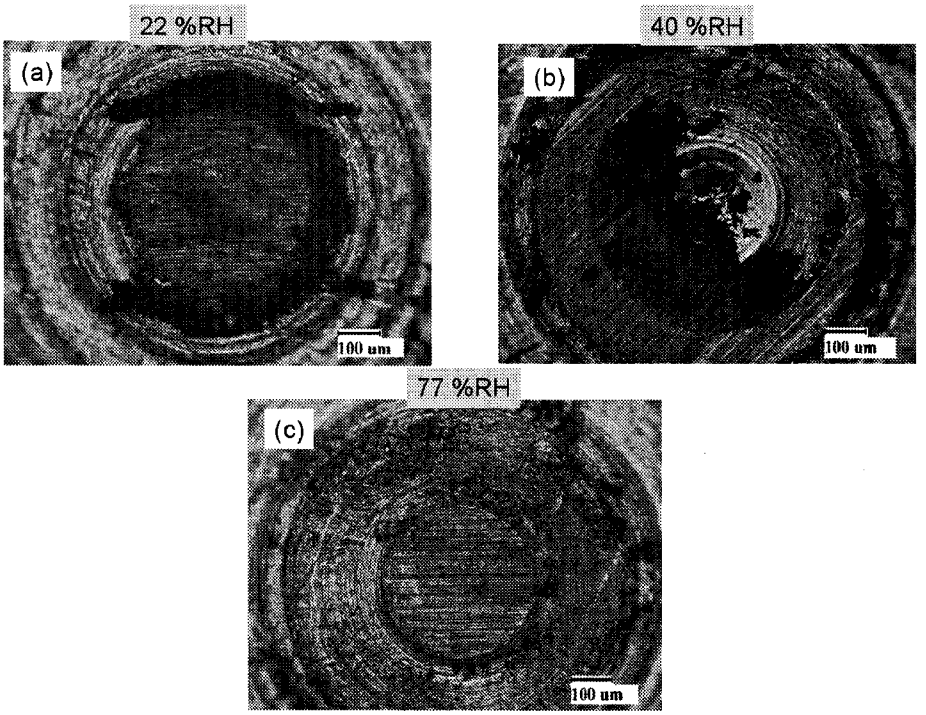

Figure 4-18: Optical microscopy images of 319 Al pin after sliding against NH-DLC for 5000 cycles in air with (a) 22% RH (b) 40% RH and (c) 77% RH

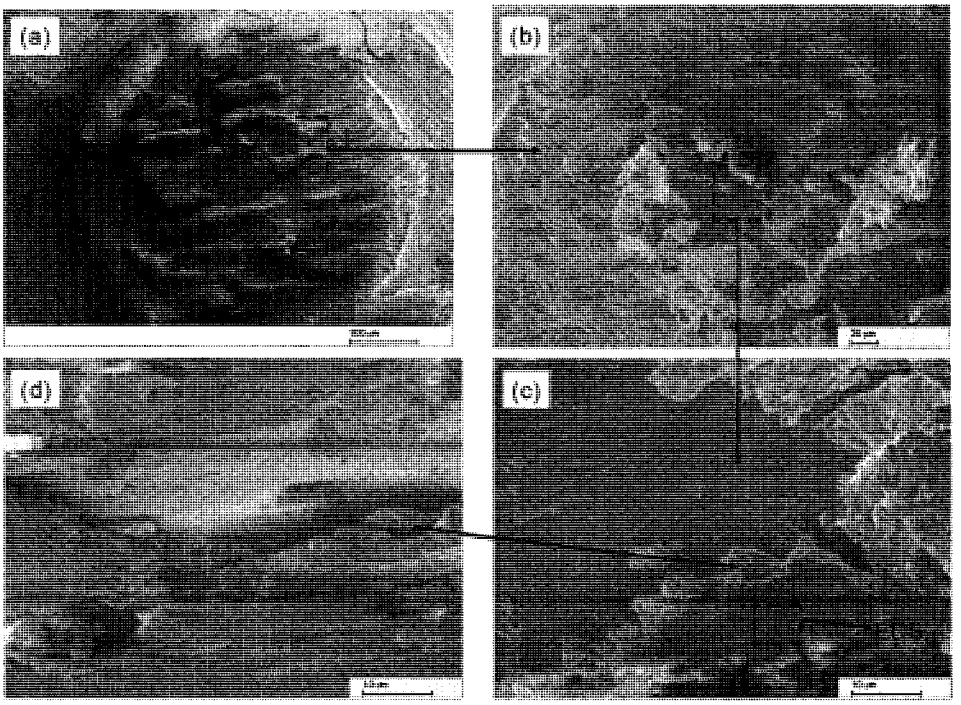

Figure 4-19: Micrographs of 319 Al pin after sliding against NH-DLC for 5000 cycles in air at 22% RH (a) top view of the aluminum pin with material transfer on the tip, (b) closer image of the material transfer, (c) pin tilted at 45 ° angle and (d) side view of the material transfer from 78 ° angle

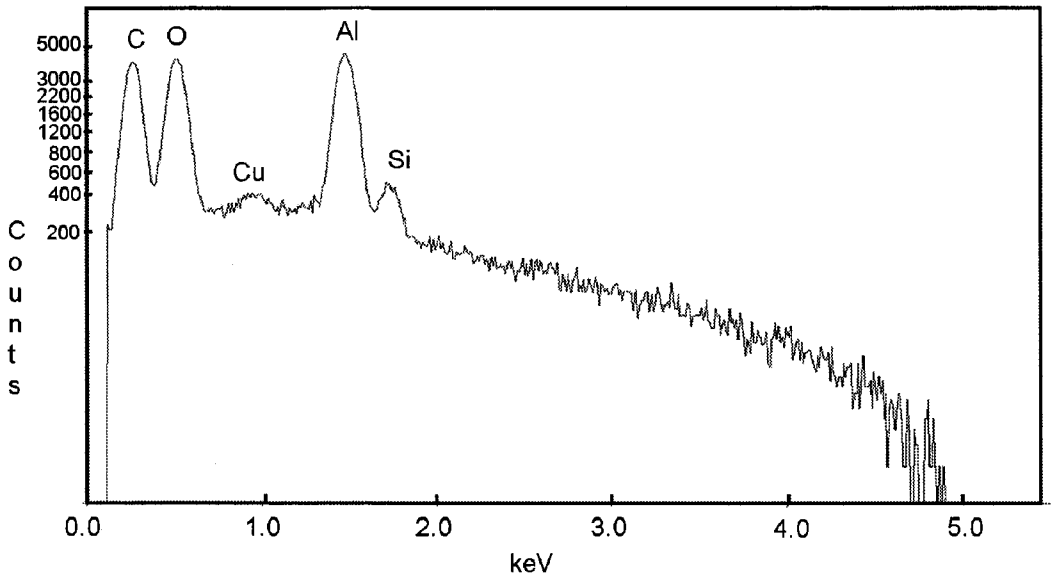

Figure 4-20: EDS analyses taken from Figure 4-19 (c) of the material transfer formed on the tip of the 319 Al after slid against NH-DLC at 22% RH for 5000 sliding cycles

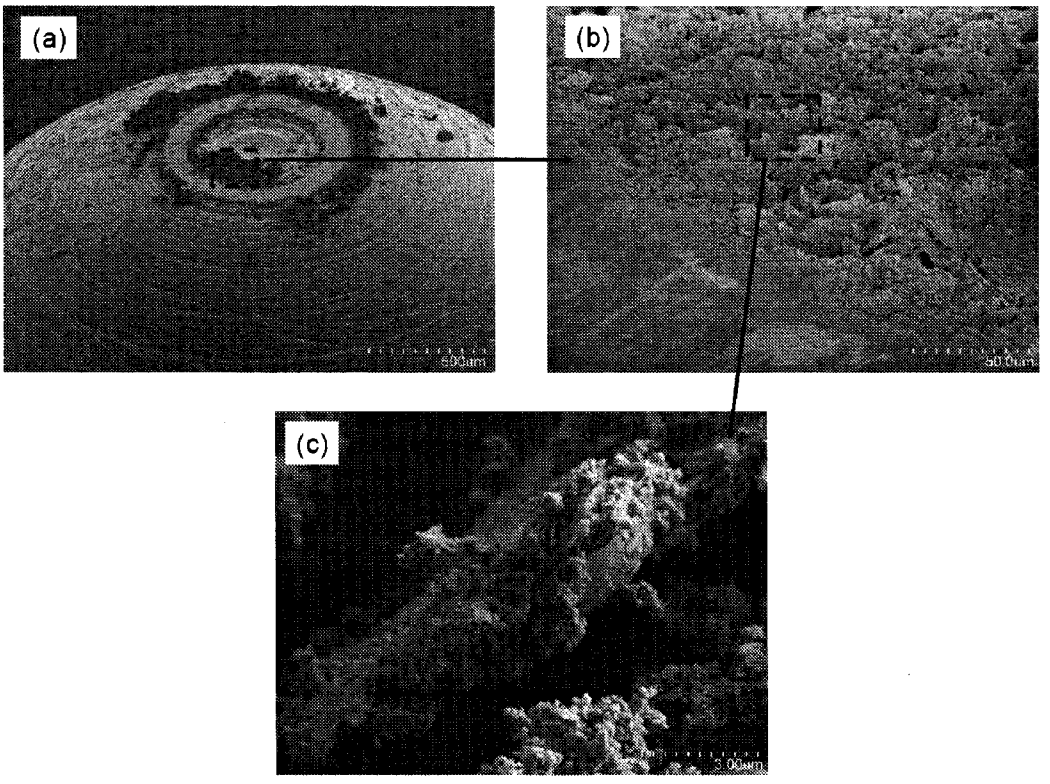

Figure 4-21: Micrographs of 319 Al pin after sliding against NH-DLC for 5000 cycles in air at 40% RH (a) side view of the aluminum pin with material transfer on the tip, (b) higher magnification of the material transfer and (c) higher magnification of the transfer layers

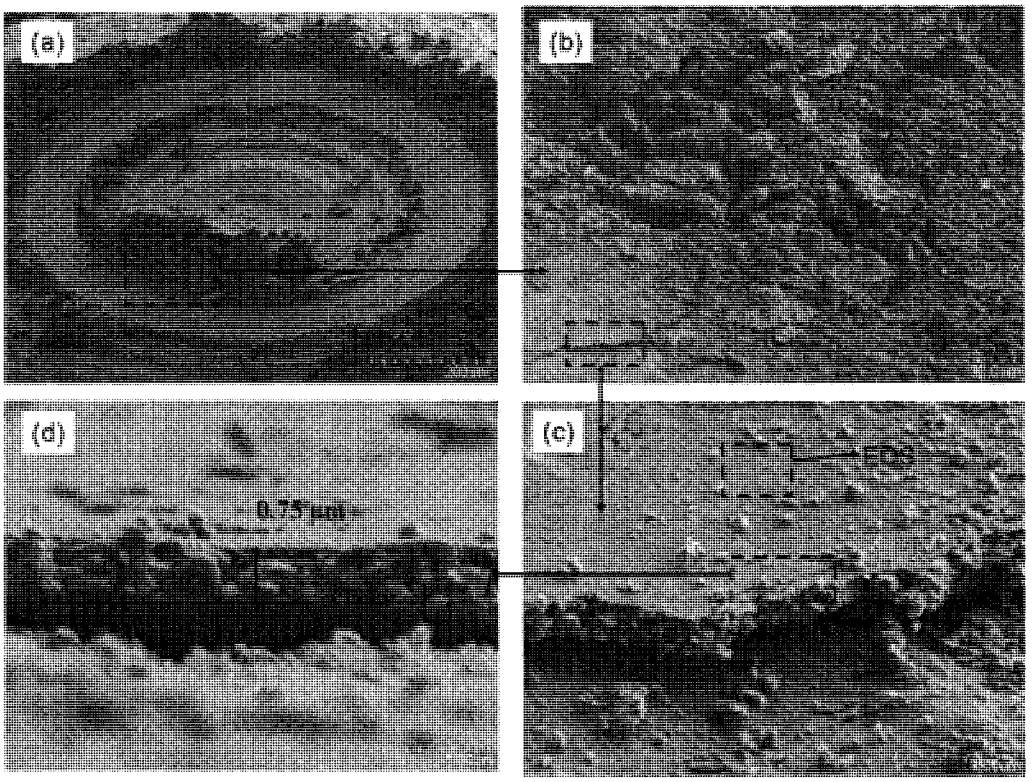

Figure 4-22: Micrographs of 319 Al pin after sliding against NH-DLC for 5000 cycles in air at 40% RH (a) top view of the aluminum pin with material transfer on the tip, (b) closer image of the material transfer and (c) view of the transfer layer (d) higher magnification of the transfer layer.

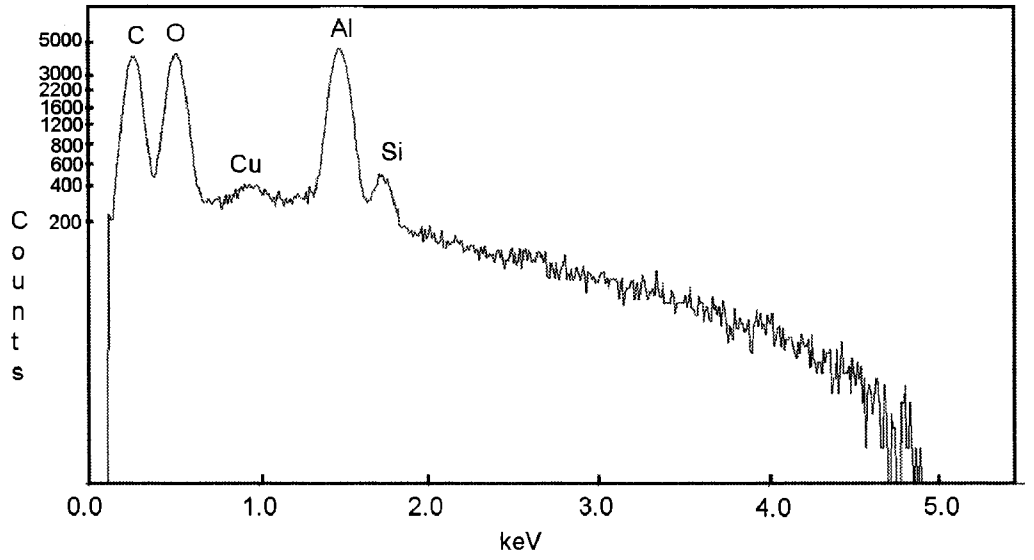

Figure 4-23: EDS analyses taken from Figure 4-22 (c) of the material transfer formed on the tip of the 319 Al after slid against NH-DLC at 40% RH for 5000 sliding cycles

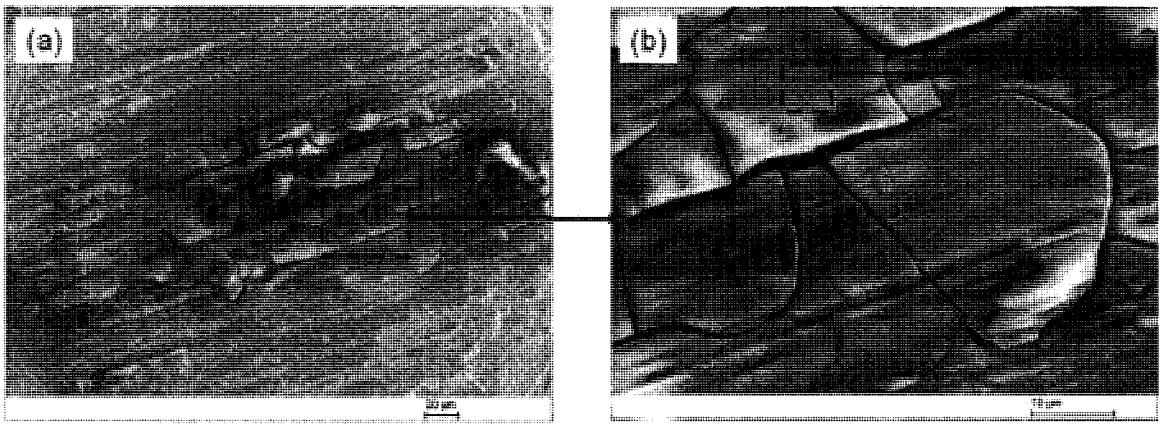

Figure 4-24: Micrographs of 319 Al pin after sliding against NH-DLC for 5000 cycles in air at 77% RH (a) top view of the aluminum pin with carbon transfer layer on the tip and (b) higher magnification of the material transfer

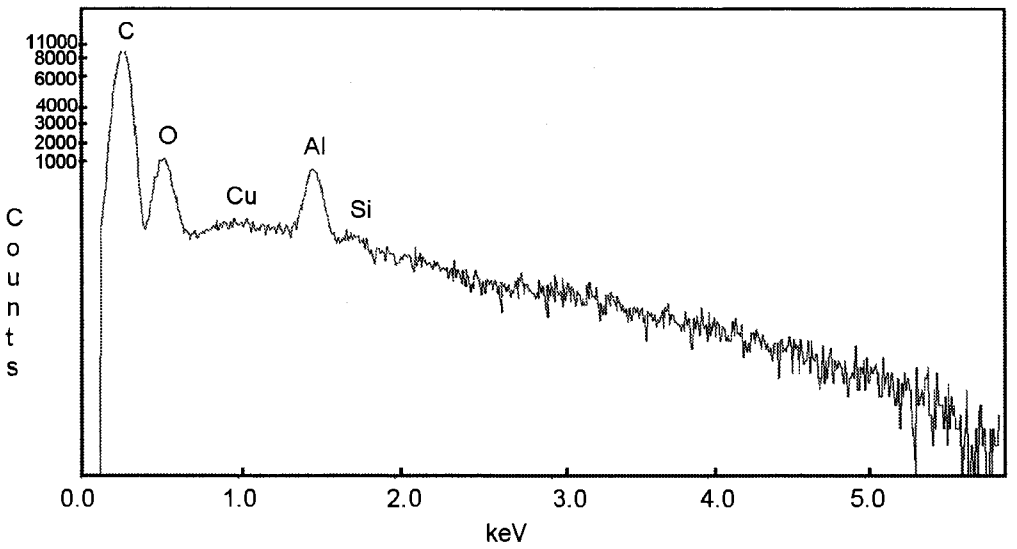

Figure 4-25: EDS analyses taken from Figure 4-24 (b) of the material transfer formed on the tip of the 319 Al after slid against NH-DLC at 77% RH for 5000 sliding cycles

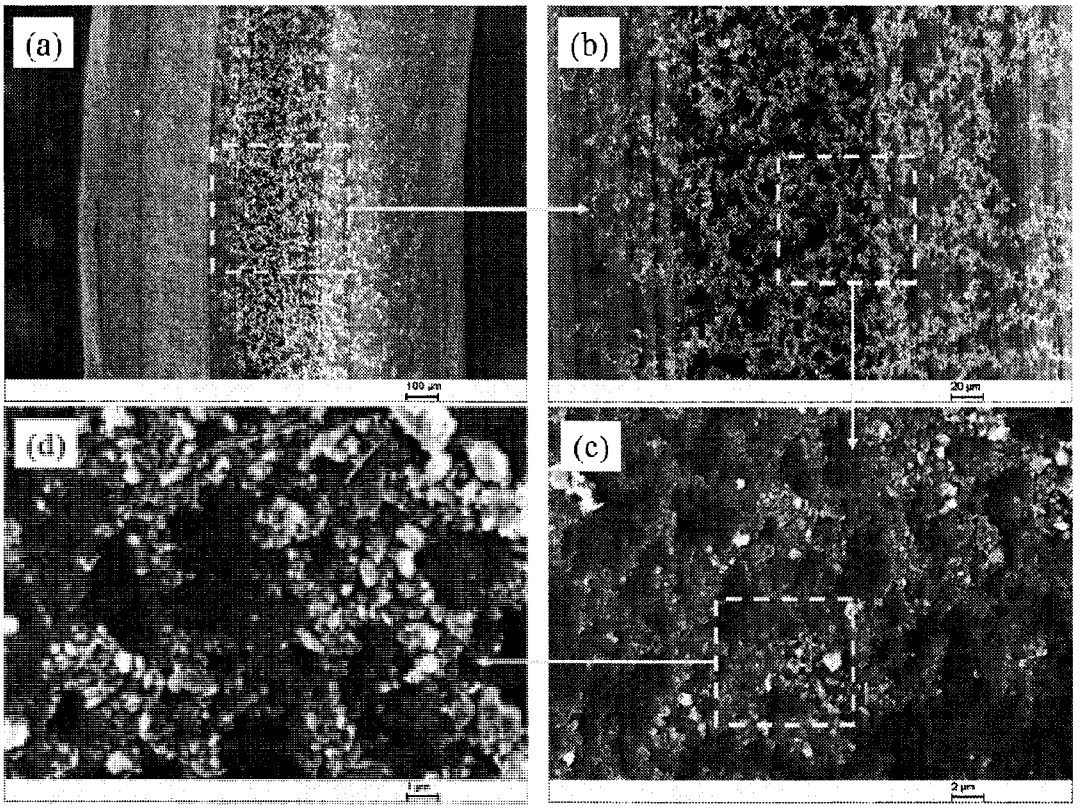

Figure 4-26: Micrographs of the NH-DLC wear track after sliding for 5000 cycles in air at 77% RH (a) wear track (b), (c) and (d) are higher magnifications showing the debris inside the wear track

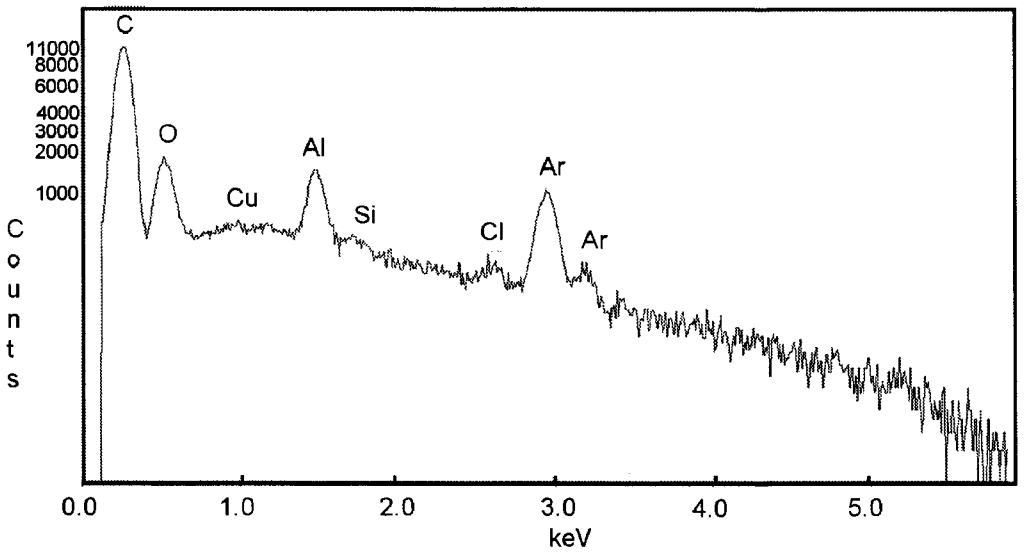

Figure 4-27: EDS analyses of the debris found inside the NH-DLC wear track after sliding in 77% RH atmosphere for 5000 sliding cycles

4.2.4 Effect of Initial Run-in in Ambient Air on the COF in Vacuum

As observed earlier in Section 4.2.1, the COF of NH-DLC was relatively high (0.7 ± 0.2) compared to H-DLC with a COF (0.02 ± 0.01) in vacuum. In addition to the difference in the hydrogen content, it was observed that NH-DLC did not form carbon transfer layers, while H-DLC did. However, in Sections 4.2.2 and 4.2.3, carbon transfer layers were formed by the NH-DLC on the 319 Al pin in ambient and produced a COF of 1.29 ± 0.15. Thus, it is apparent that carbon transfer layers lead to COF reduction. To validate this statement, carbon transfer layers must be present on the counter surface sliding against NH-DLC in vacuum and show the COF decrease to values below 0.7 ± 0.2. Consequently, Konca *et al.* [7] and [28], who originated the idea, tested 319 Al against NH-DLC in ambient air initially to form the carbon transfer layers, and then evacuate the test chamber to vacuum while the test is running to observe how the presence of carbon transfer would affect the friction in vacuum.

The same experiment was conducted in this study, with 319 Al sliding against NH-DLC coating at 0.1 m/s speed, 5 N load and an initial running-in period in ambient air (25% RH) for 13000 cycles, followed by 5000 sliding cycles in vacuum. Figure 4-28, presents the test results in ambient air (25% RH) after 300 cycles of run in period, at which point a steady state COF of 0.11 ± 0.02 was reached. As the chamber pressure decreased to 0.133 Pa (vacuum), the COF dropped to 0.03 ± 0.02. At 13000 cycles, the COF shifted between 0.15 and 0.06 due to a pressure fluctuation prompted by the valves switching from mechanical to turbo pump evacuation. After 3000 sliding cycles at a low friction regime (LFR) with a COF of 0.03 ± 0.02, the COF spiked to 0.75, which is typical for NH-DLC in vacuum if tested without initial running-in in ambient air.

The residual gas analyzer (RGA) was switched on at 14000 cycles, when pressure inside the chamber dropped below 0.133 Pa, where the RGA is operational to identify the gas species present inside the vacuum chamber. Analyses results shown in Figure 4-29 indicate that the chamber mainly consists of moisture, hydrogen and nitrogen with partial pressures of $3x10^{-3}$, $3x10^{-4}$ and $1x10^{-4}$ Pa, respectively. Other species were also present, such as carbon dioxide and oxygen, but at low partial pressure ($< 2x10^{-5}$ Pa).

The surface profile image of the pin contact surface after sliding against NH-DLC for 18000 cycles (Figure 4-30 (a)), suggests that the aluminum pin was worn off, which produced a large wear scar (1.2 x 1 mm). As for the wear track, the surface profilometry images shown in Figure 4-30 (b), also demonstrate that the coating was worn off. The wear track measured 0.931 mm wide with non-uniform scars (peaks and valleys) and a maximum depth of 2.5 μm, much deeper than the coating thickness (1.6 μm). Micrographs of the aluminum tip after the 18000 cycles (Figure 4-31 (a)) shows no evidence of transfer layers, while the EDS shown in Figure 4-32 obtained from inside the wear scar (Figure 4-31 (b)), indicate the presence of aluminum, silicon and oxygen, which is from the 319 Al pin. Micrographs of the wear track (Figure 4-33 (a) and (b)) also illustrate the presence of material transfer inside the wear track and the EDS of the material transfer inside the wear track (Figure 4-34) confirms that the carbon coating was penetrated, reaching to the chromium interlayer which lead to a high COF.

The LFR behaviour in vacuum after initial running-in in ambient air was also observed for 52100 steel counterface running against NH-DLC. Figure 4-35 illustrates that in air, the COF was 0.1 ± 0.03 and once the chamber was evacuated, the COF dropped to 0.02 ± 0.02. Again, the low friction regime did not last for long. After 6000

cycles, the COF spiked to 0.9. Micrographs of the 52100 steel ball after the experiment (Figure 4-36 (a) and (b)), presents no evidence of material transfer, only small carbon debris particles confirmed by EDS (Figure 4-37). In addition, micrographs of the wear track (Figure 4-38) shows patches inside the wear track. EDS (Figure 4-39) of these patches picked up chromium and iron peaks, indicating that the patches were areas where the coating is worn out. Consequently, from the results it was shown that the LFR could also be produced by 52100 steel. Furthermore, Konca *et al.* [28], [31] confirmed that the low friction regime produced by other counter surfaces such as WC and Ti running against NH-DLC in ambient air initially then vacuum.

These experiments have shown that the friction of NH-DLC can be reduced under vacuum if it was initially run-in in ambient air, and is entirely dependant on the counterface material. However, no clear evidence of what is behind the LFR. For that reason, the same experiment was conducted again with 319 Al sliding against NH-DLC. However, the test was stopped right after the chamber was evacuated in the middle of the LFR, when the COF dropped to 0.03 ± 0.01 (Figure 4-40). Running 319 Al pin against NH-DLC initially in ambient air at 25% RH, lead to a COF of 0.18 ± 0.05. After 1700 sliding cycles in ambient air the chamber was evacuated, causing the COF to drop down to 0.03 ± 0.01, then the test was stopped at 2100 cycles to analyze the pin surface. RGA analyses of the vacuum chamber between 1900 and 2000 cycles (Figure 4-41) illustrate that partial pressures of water, nitrogen, oxygen and hydrogen were constant at $4x10^{-3}$, $2x10^{-3}$, $2x10^{-4}$ and $3x10^{-4}$ Pa respectively.

The surface profile of the pin tip at the LFR (Figure 4-42 (a)), demonstrate that the wear scar is not uniform but has elevated areas that indicate material transfer. The

wear track in this regime is 0.1987 mm wide and 0.54 μm deep (Figure 4-42 (b)), suggest that the NH-DLC coating is still intact. Micrographs of the pin surface, confirms the presence of material transfer during the LFR (Figure 4-43 (a)). Furthermore, (Figure 4-43 (c) and (d)) indicate that the material transfer forms a layered structure. A cross section of theses layers (Figure 4-43 (d)) indicate that they are in the order of 2.25 μm thick. This type of material transfer layers were seen to form in ambient air, as described in Section 4.2.3 and EDS confirmed that they consist of mainly carbon. However, this time the material transfer layers were analyzed by Fourier-Transform Infrared spectroscopy (FTIR) to give more insight about the chemistry of these layers. FTIR analyses presented in Figure 4-44 confirm that they consists of carbon, what is also interesting is that hydroxyl (OH) and hydrocarbons (C-H) were detected. The significance of these species will be described in the discussion.

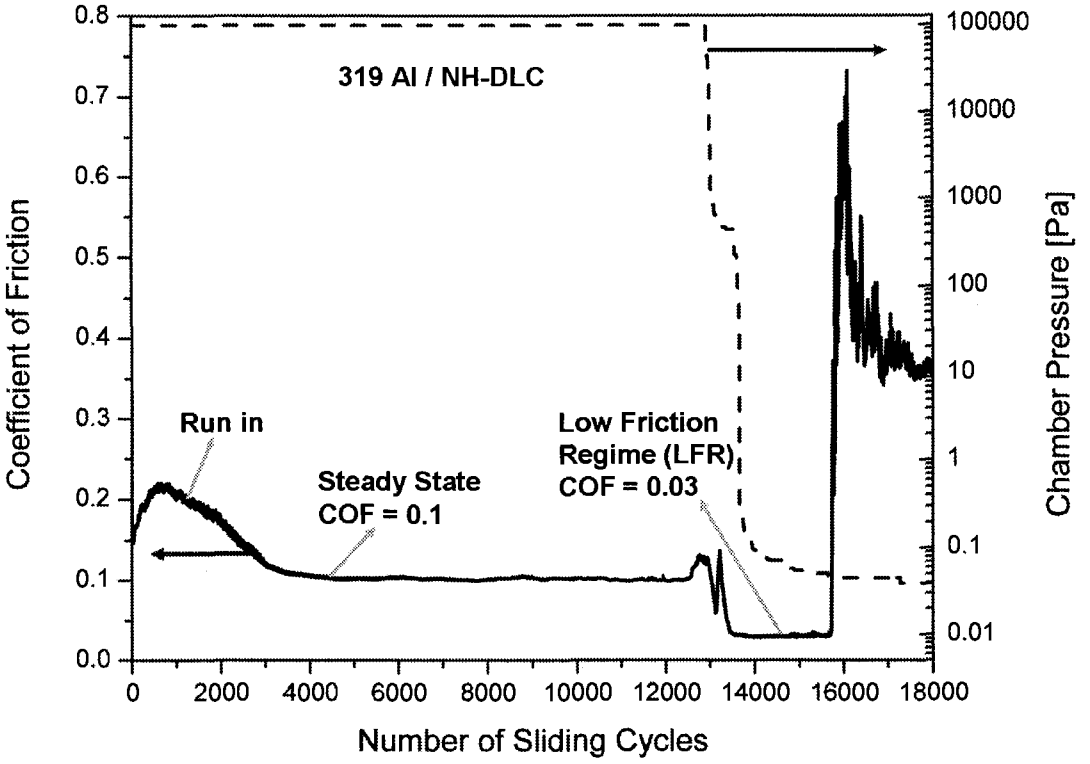

Figure 4-28: Pin-on-disc wear test of 319 Al sliding against NH-DLC at 5 N and 0.1 m/s sliding speed: effect of initial ambient air running-in period on the COF in vacuum

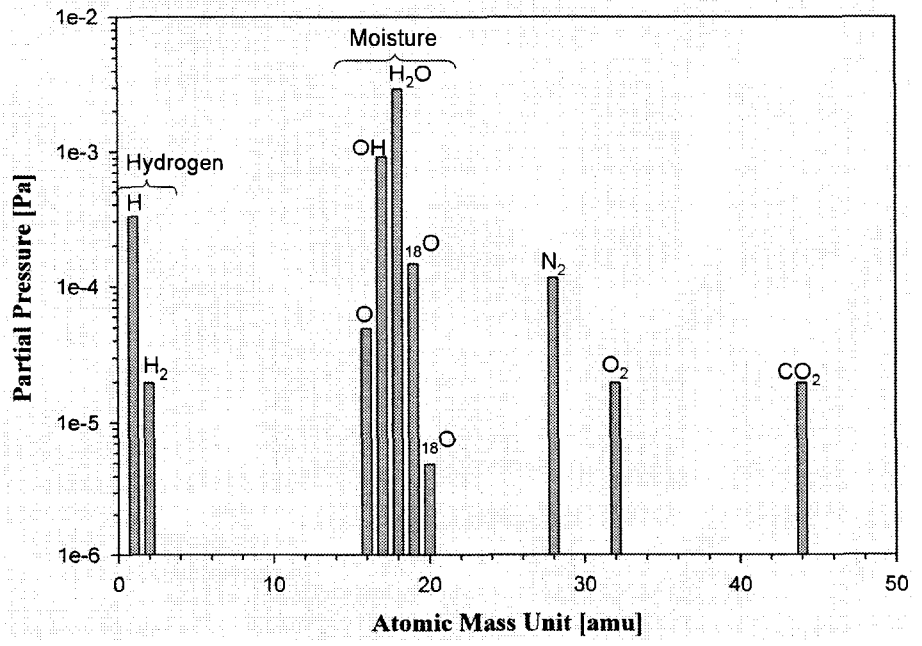

Figure 4-29: RGA analyses of gas species inside the test chamber during the low friction regime

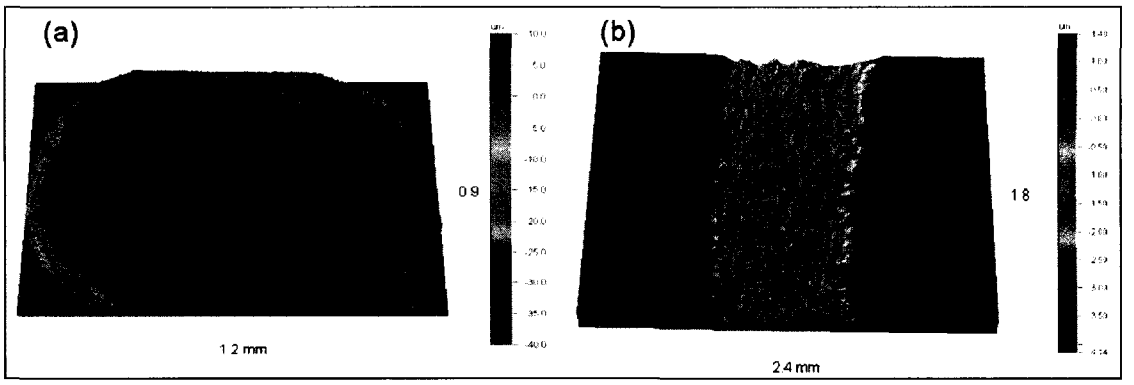

Figure 4-30: Surface profile of the (a) 319 Al pin and (b) wear track after 18000 cycles

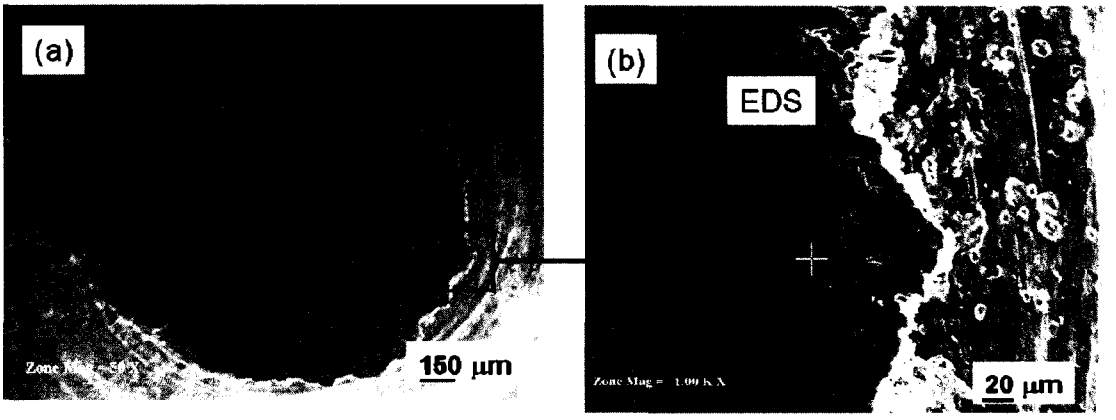

Figure 4-31: Micrographs of the (a) 319 Al pin tip (b) edge of wear scar of 319 Al pin after 18000 cycles

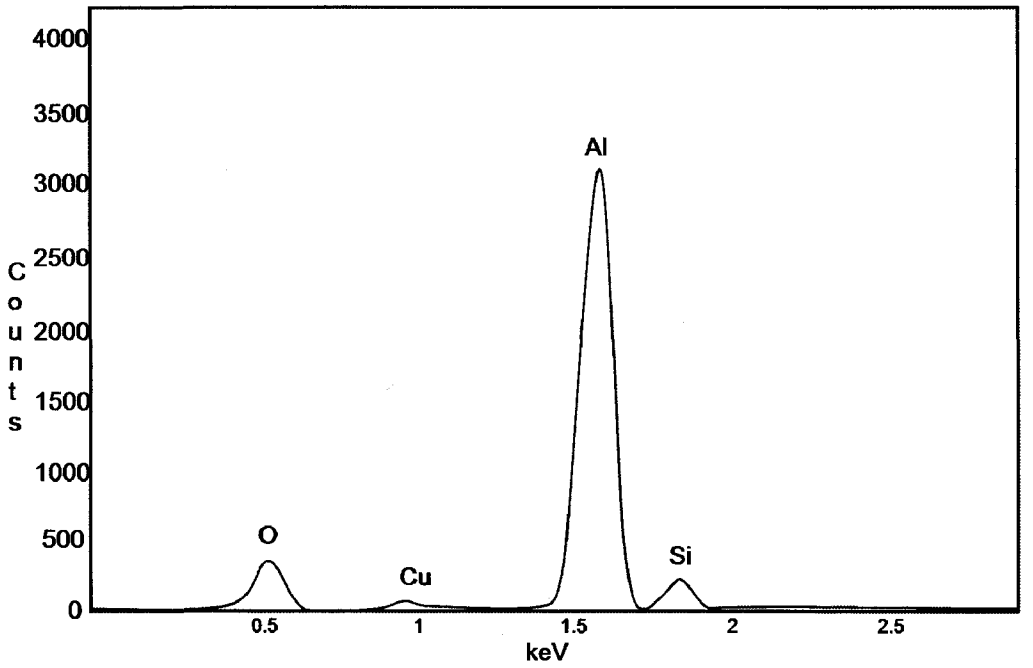

Figure 4-32: EDS analyses of the Al pin worn surface shown in Figure 4-29 (b), after sliding for 18000 cycles

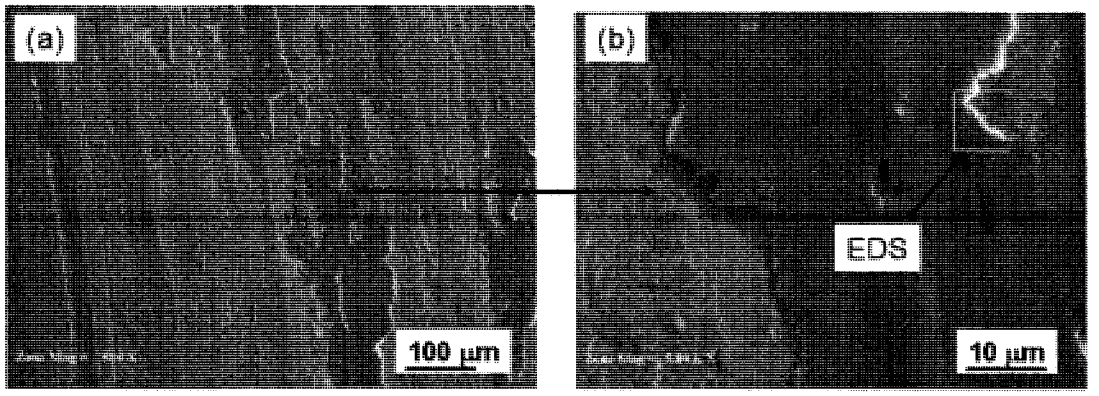

Figure 4-33: Micrographs of (a) wear track of NH-DLC (b) material transfer on the wear track after 18000 cycles

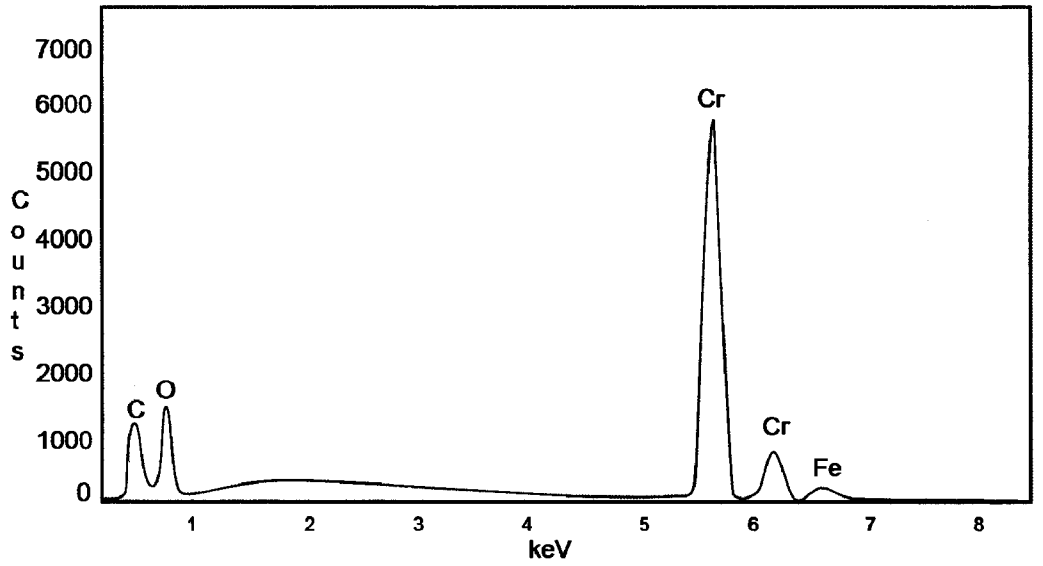

Figure 4-34: EDS analyses of the NH-DLC wear track shown in Figure 4-31 (d) after sliding for 18000 cycles

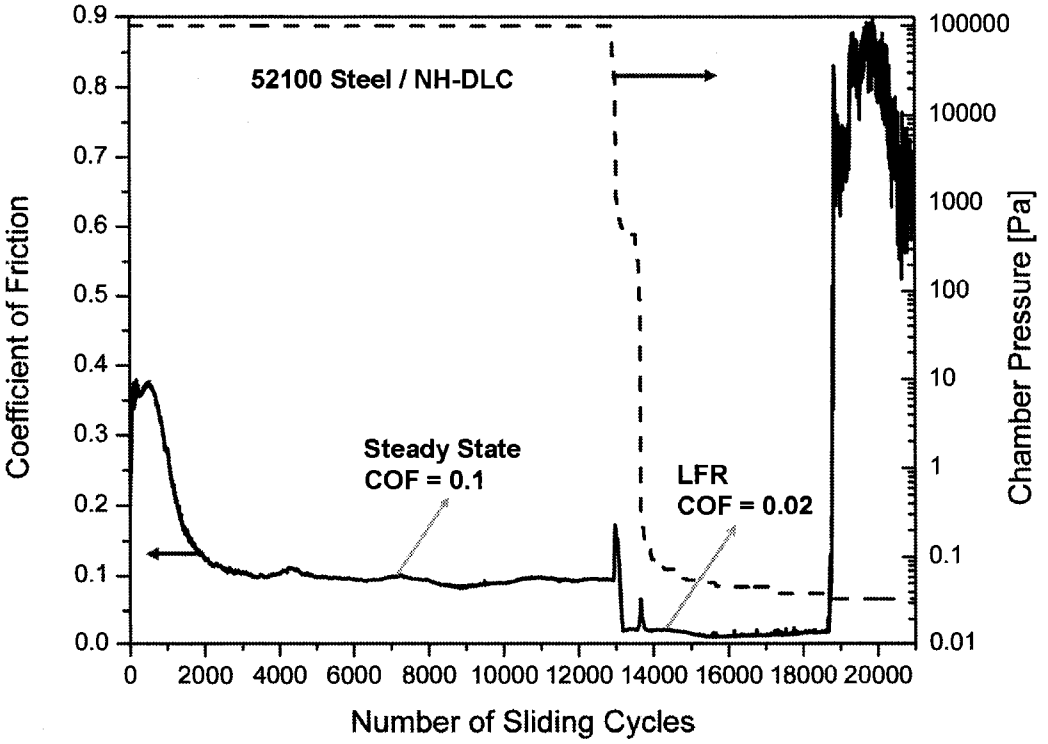

Figure 4-35: Effect of carbon transfer on the COF in vacuum for 52100 steel sliding against NH-DLC at 5 N load and 0.1 m/s sliding speed

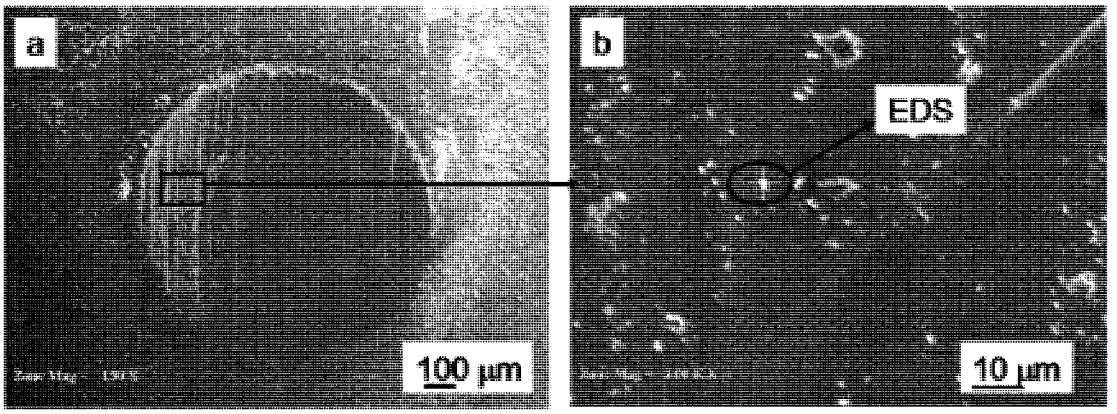

Figure 4-36: Micrographs of the (a) 52100 steel ball wear scar (b) debris inside the ball wear scar, after the experiment

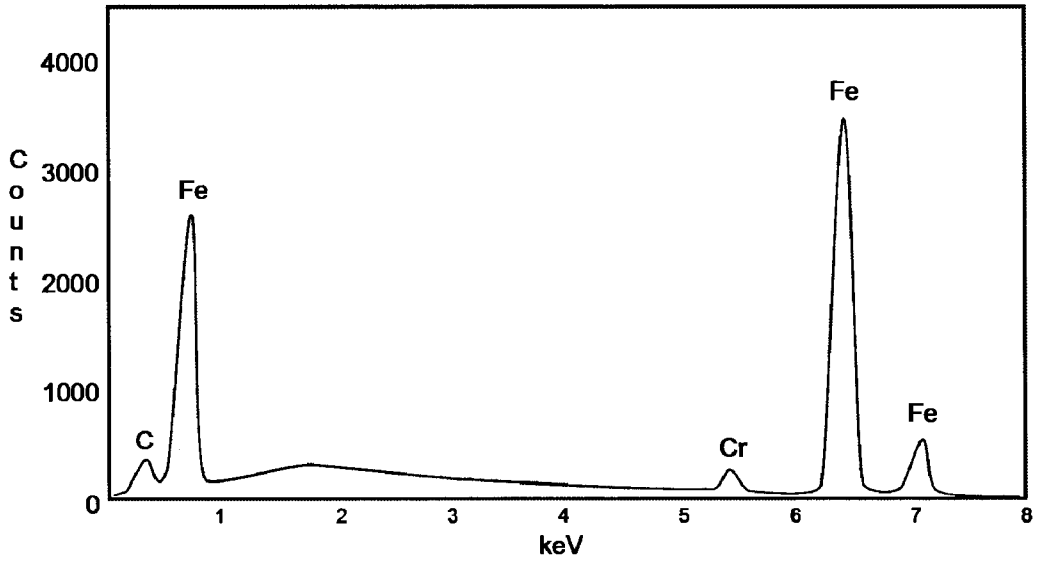

Figure 4-37: EDS analyses of the wear debris particles on the ball wear scar, obtained from Figure 4-36 (b)

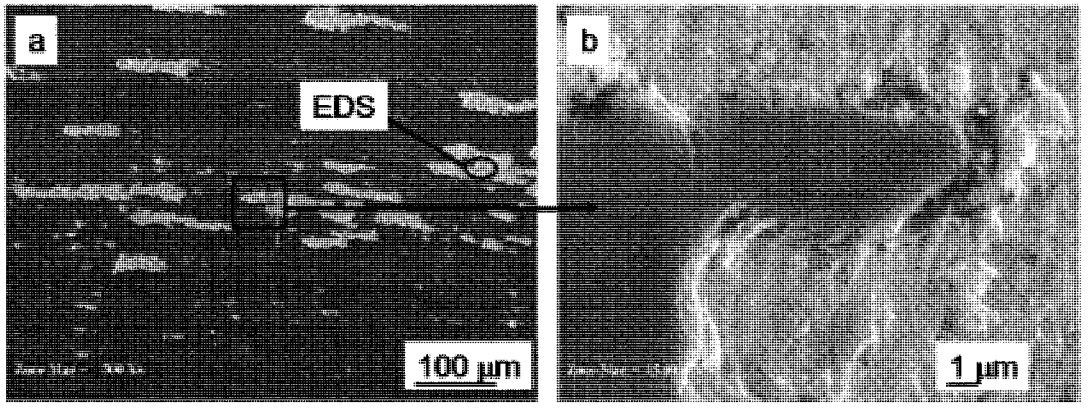

Figure 4-38: Micrographs of the (a) NH-DLC wear track (b) worn out coating, after the experiment

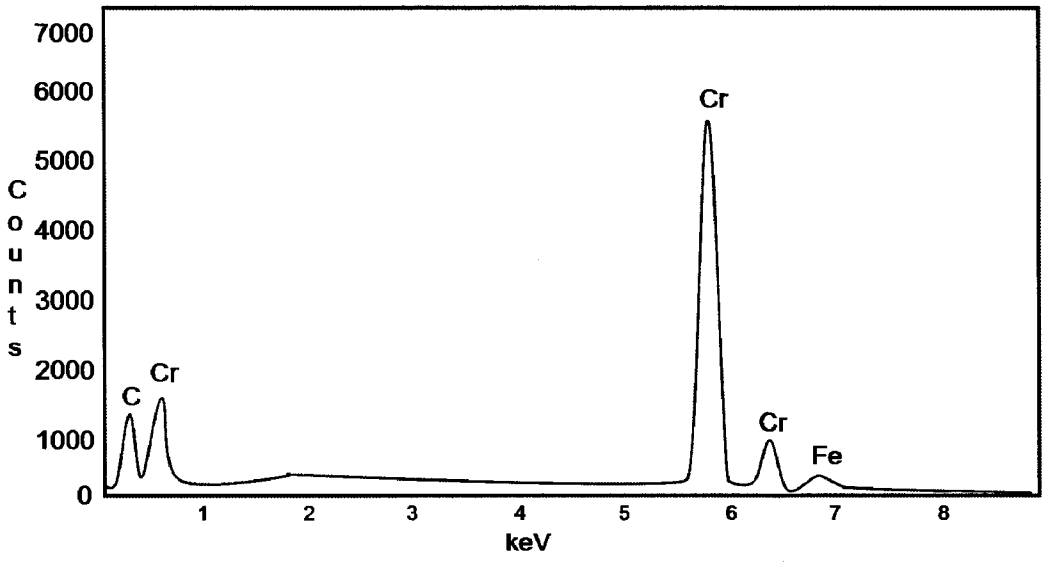

Figure 4-39: EDS analyses of the NH-DLC wear track patches obtained from Figure 4-38(a)

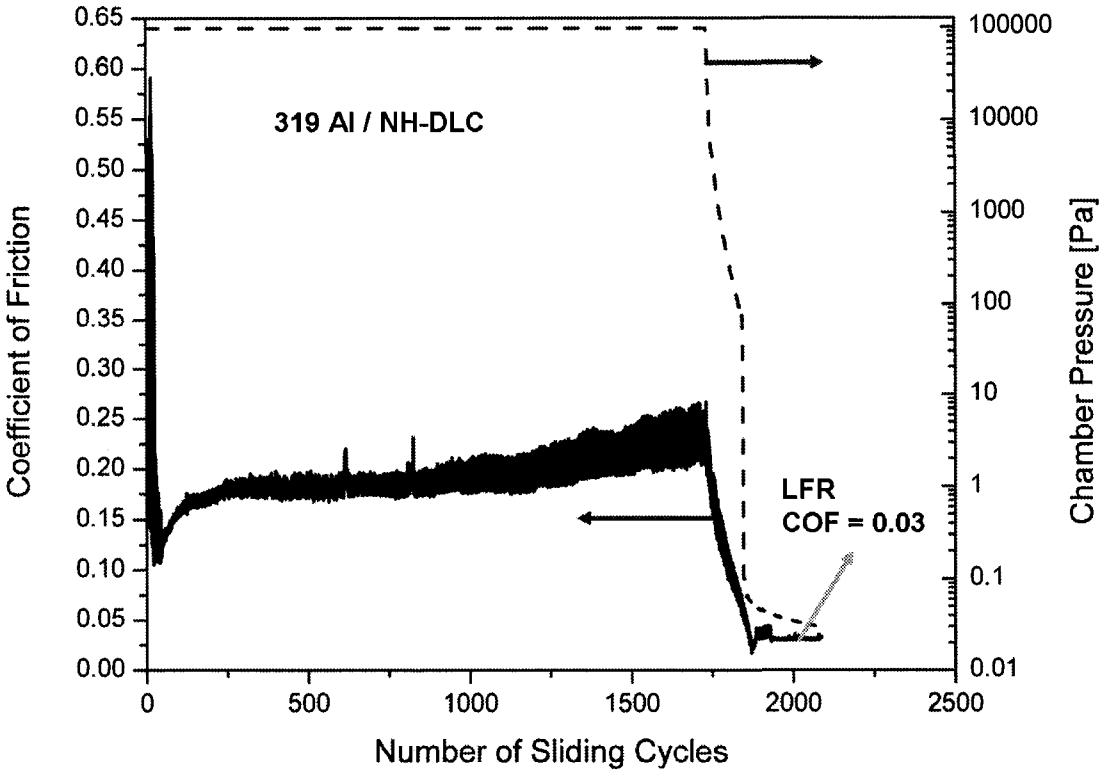

Figure 4-40: Effect of carbon transfer on the COF in vacuum for 319 Al sliding against NH-DLC at 5 N and 0.1 m/s sliding speed

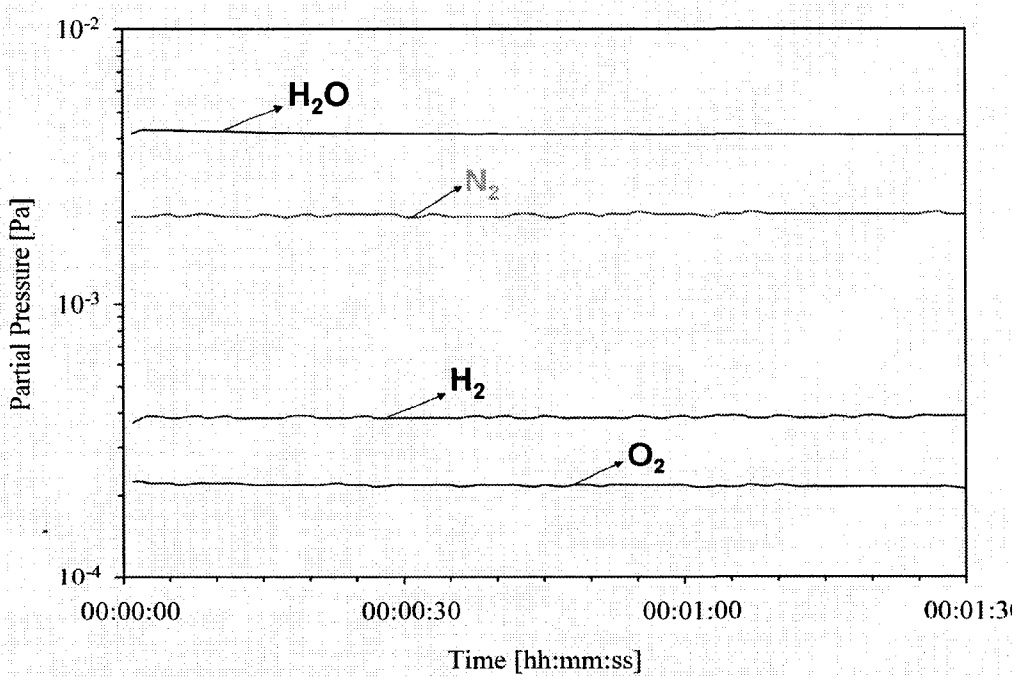

Figure 4-41: RGA spectra of water, nitrogen, oxygen and hydrogen partial pressures during the low friction regime after sliding in ambient air. RGA was turned on from 1900 to 2000 cycles

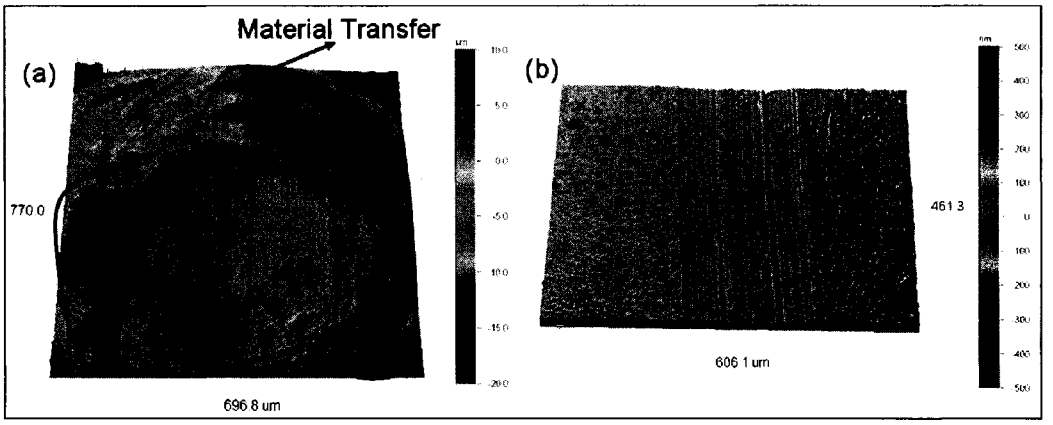

Figure 4-42: Surface profile of the (a) 319 Al pin and (b) wear track during the low friction regime

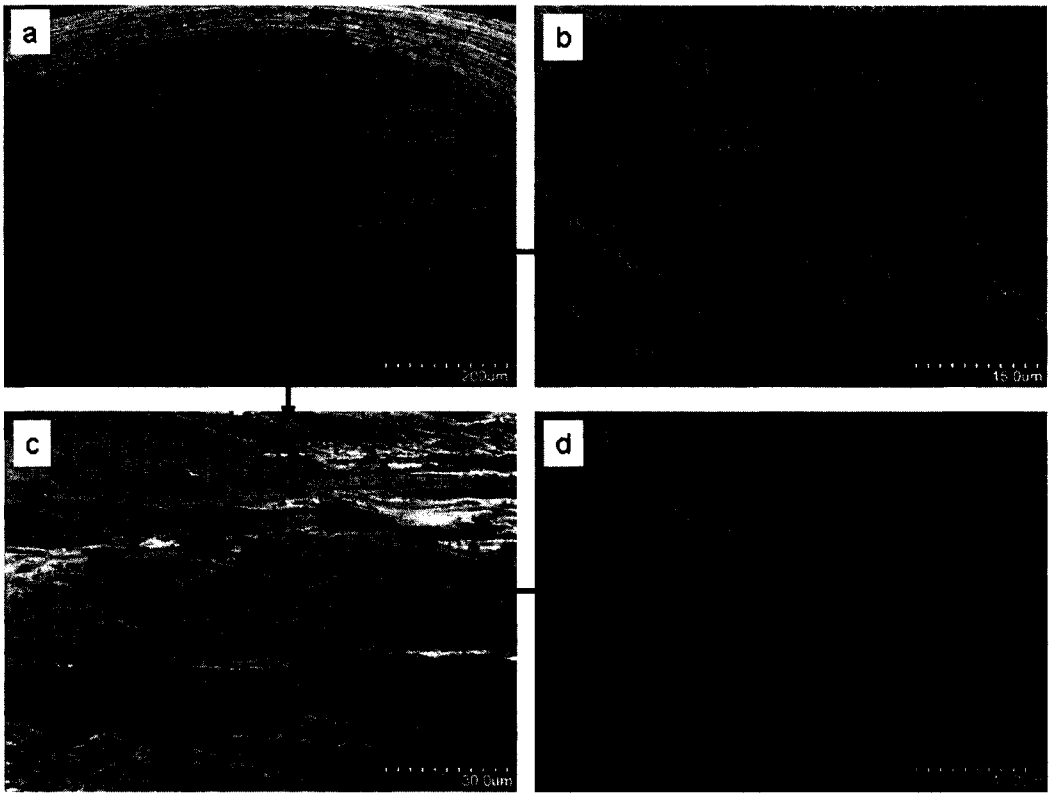

Figure 4-43: Micrographs of the 319 Al pin wear scar during the low friction regime (a) tilted 60° (b) Carbon transfer layers tilted 60° (c) Carbon transfer layers on the 319 Al pin tilted 80° (d) cross section of the Carbon transfer layers on the 319 Al pin tilted 90°

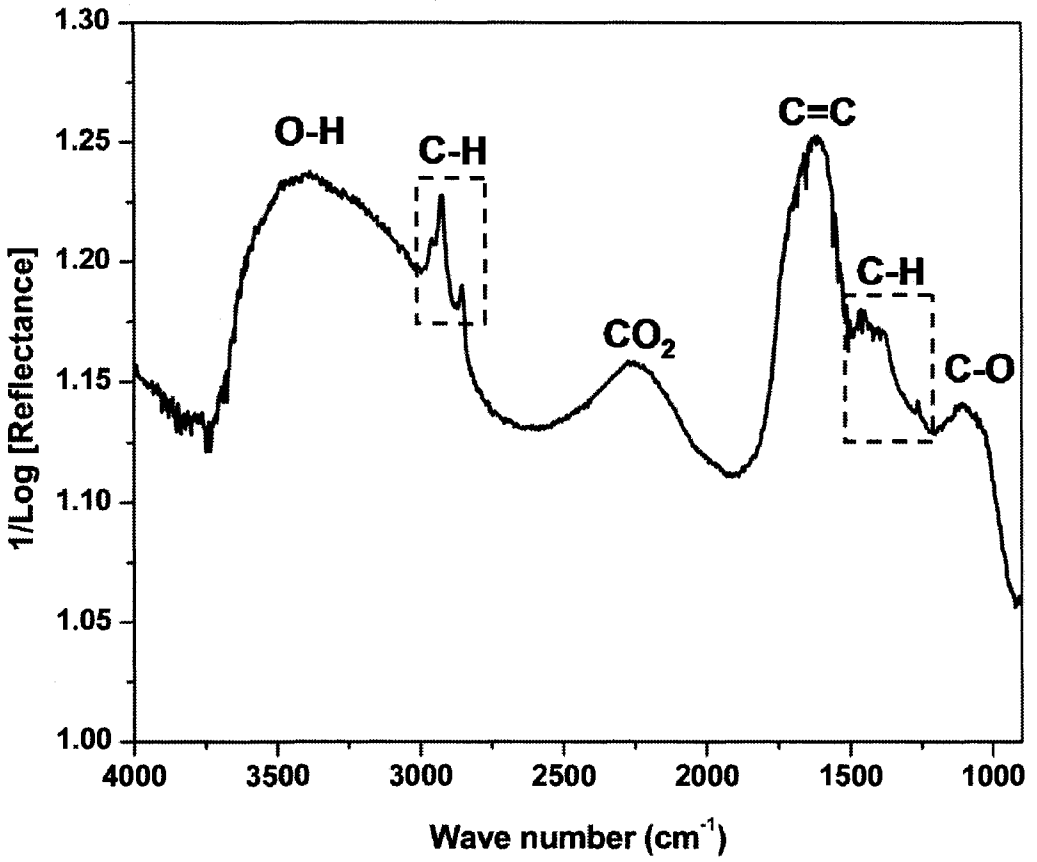

Figure 4-44: FTIR analyses of the Carbon transfer on the 319 Al pin after running-in in ambient air

4.2.5 Effect of Running-in Gas Species on Friction in Vacuum

At this point, it is clear that the presence of carbon transfer layers reduces the COF of NH-DLC as shown in Section 4.2.4. However, it is not known how and why carbon transfer layers, which lead to low friction regime. Thus, dry sliding experiments were performed using 319 Al pins sliding against NH-DLC coatings with initial testing period in dry air, dry nitrogen and dry oxygen. Then the chamber was evacuated while continuing the friction rest. The purpose of these tests was to observe the effects of initial run in gas species such as dry air, dry nitrogen and dry oxygen, on the transfer layer formation and friction behaviour in vacuum.

4.2.5.1 Effect of Initial Running-in in Dry Air on COF in Vacuum

When 319 Al was initially tested against NH-DLC in dry air initially, it was observed that the COF started at 0.1 ± 0.01 and increased to 0.7 ± 0.2. After 500 cycles the COF reached a steady value of 0.55 ± 0.1 (Figure 4-45). Which was expected of NH-DLC due to the absence of moisture in the atmosphere as observed in Section 4.2.3, proven to be an important factor in reducing the COF of NH-DLC. As the chamber pressure was reduced to reach vacuum, the COF dropped to 0.04 ± 0.02. The RGA was turned on at 2000 cycles (under vacuum), to identify the partial pressure of gas species inside the chamber (Figure 4-46), particularly moisture, nitrogen, oxygen and hydrogen. The spectra presents the partial pressures as a function of time during the LFR and it is shown that the partial pressures of oxygen drifted with time, while water, nitrogen and hydrogen partial pressures remained steady inside the chamber at $5x10^{-3}$, $6x10^{-5}$ and $6x10^{-5}$ inside the chamber through out the analysis period of 4000 cycles.

Optical images of the aluminum pin after 6000 cycles shown in Figure 4-47 (a) illustrate the presence of material transfer on the pin contact surface. In addition, Figure 4-47 (b) displays the NH-DLC wear track with no evidence of adhesion on the surface. Micrographs of the pin after the test (Figure 4-48 (a)) confirms the presence of material transfer on the tip. Figure 4-48 (b) and (c) illustrate that the material transfer is in layer formation. Furthermore, EDS verifies that the material transfer layers consists of carbon (Figure 4-49). Besides EDS, the carbon transfer layers on the 319 Al pin were analyzed using FTIR spectroscopy. Results shown in Figure 4-50, confirm that the layers consist of hydrocarbons, hydroxyl and carbonyl groups. Consequently, test results and analyses of the aluminum pin support the findings in Section 4.2.4, that the formation of carbon transfer layers on the countersurface serves to reduce the COF of NH-DLC in vacuum.

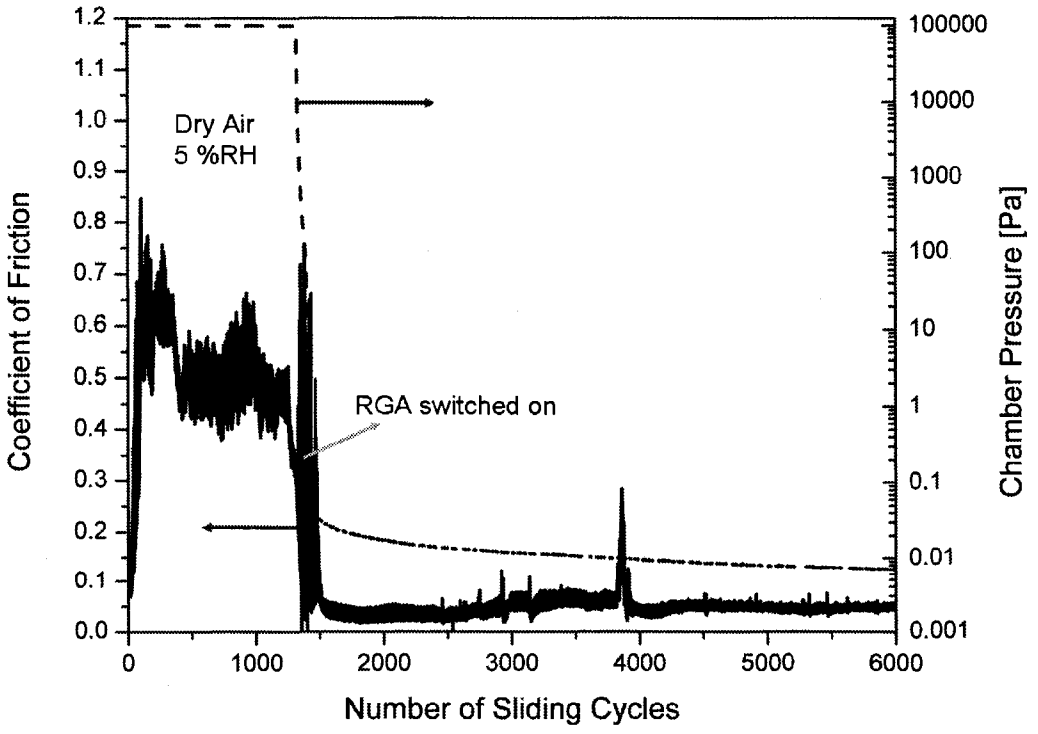

Figure 4-45: Influence of vacuum on the COF after an initial run in period in dry air for 319 Al sliding against NH-DLC at 5N load and 0.1 m/s speed

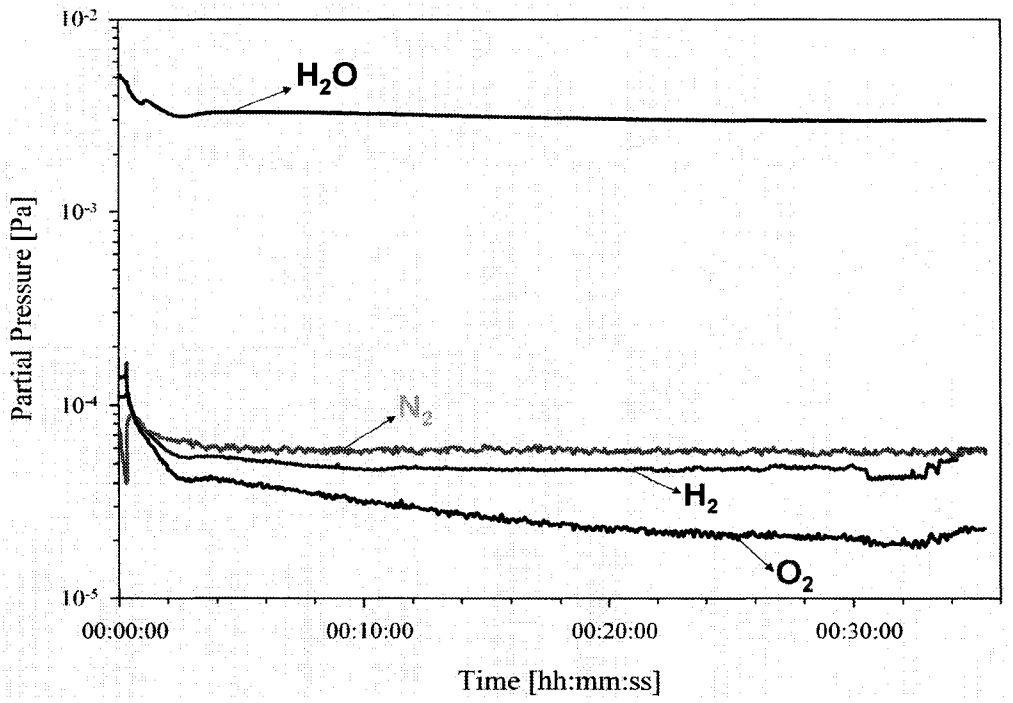

Figure 4-46: RGA spectra of water, nitrogen, oxygen and hydrogen partial pressures during the low friction regime after sliding in dry air. RGA was turned on from 2000 to 6000 cycles

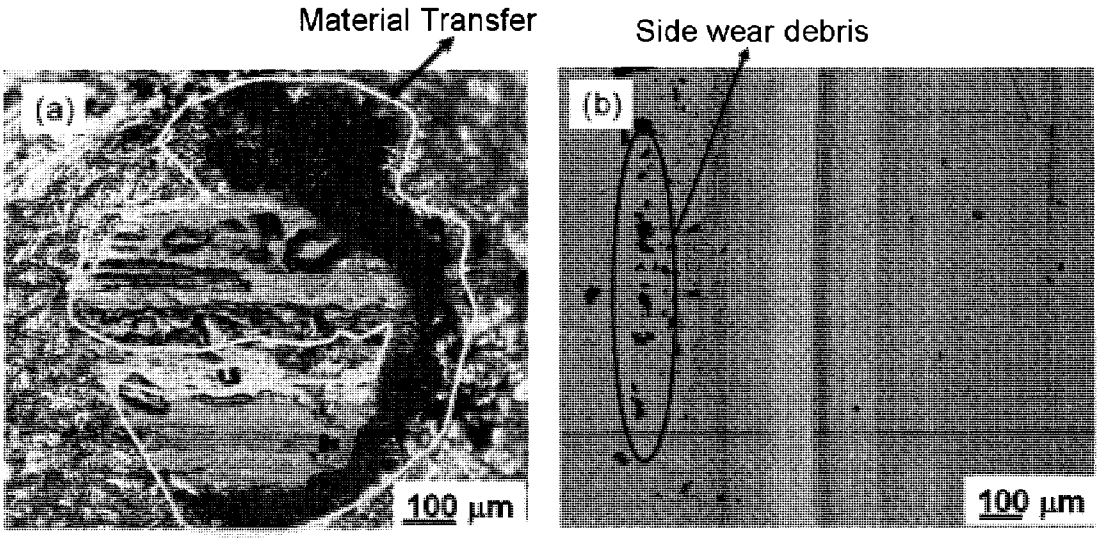

Figure 4-47: Optical image of (a) 319 Al pin surface (b) NH-DLC wear track after 1400 cycles running in dry air and 4600 laps in vacuum

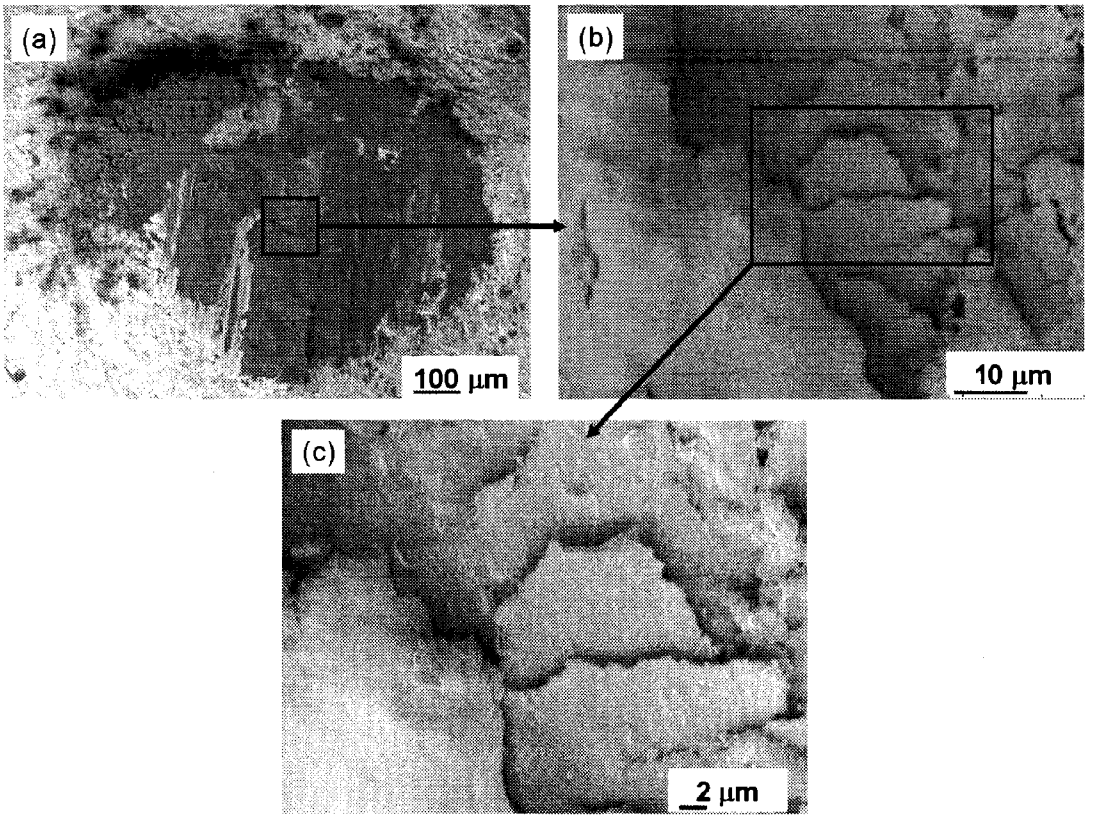

Figure 4-48: Micrographs of 319 Al pin after dry sliding from dry air to vacuum (a) pin contact surface (b) Carbon transfer layers (c) higher magnification of the carbon transfer layers

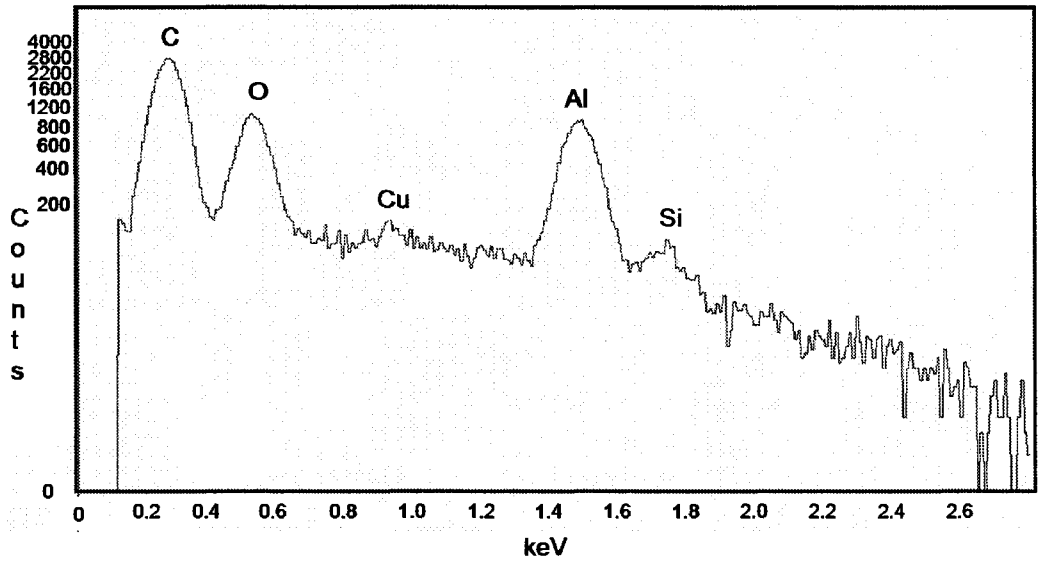

Figure 4-49: EDS spectra of the dry air to vacuum pin contact surface, obtained from area in Figure 4-48(c)

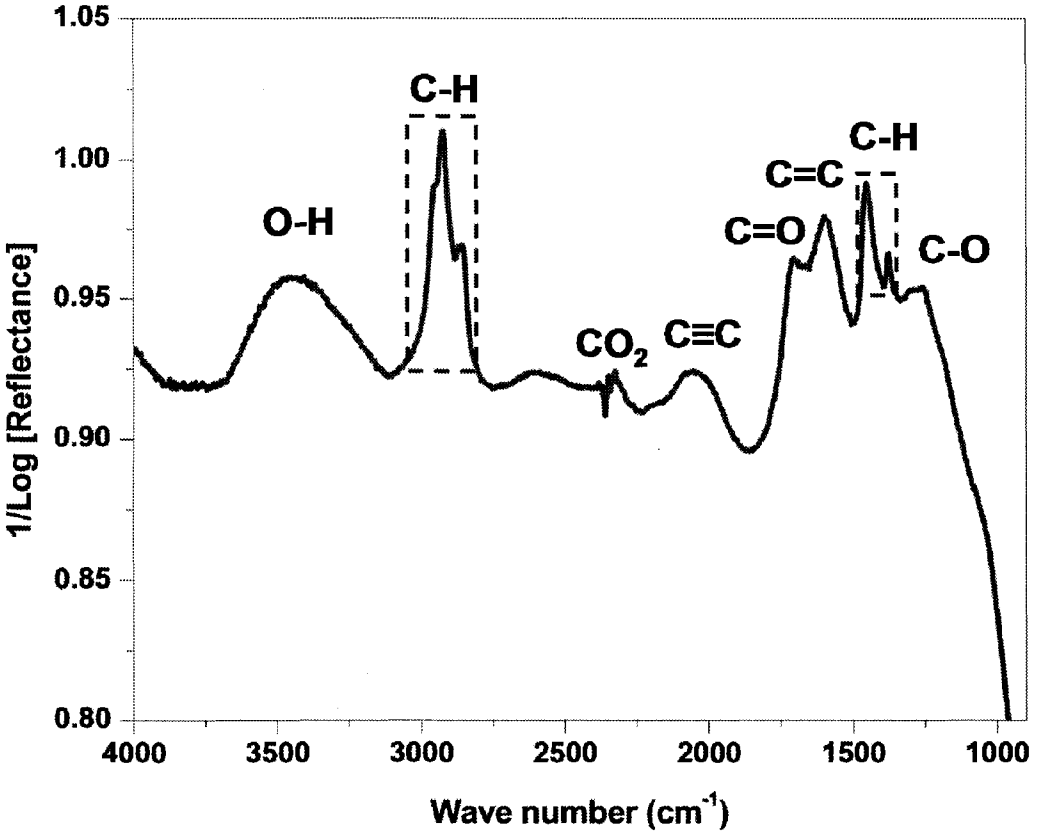

Figure 4-50: FTIR analyses of the Carbon transfer on the 319 Al pin after dry air to vacuum experiment

4.2.5.2 Effect of Initial Running-in in Dry Nitrogen on COF in Vacuum

Unlike air-to-vacuum, and dry air-to-vacuum, the COF did not drop in the transition from dry nitrogen to vacuum. Results from a 319 Al pin sliding against NH-DLC tested first in dry nitrogen revealed that the COF started at 0.2 and climbed to 0.1 after 140 cycles (Figure 4-51). The COF reached a steady value of 0.9 ± 0.1, which is similar to the COF produced under vacuum shown in Section 4.2.1 (Figure 4-9). When the chamber was evacuated at 1600 cycles, the friction did not drop to a LFR, suggesting that carbon transfer layers did not form. RGA analyses of the gas species inside the vacuum chamber (Figure 4-52) do not show any significant deviation in the partial pressure of water, oxygen and hydrogen compared to the partial pressures of dry air to vacuum observed in the previous section's experiment.

The optical image of the 319 Al pin after the experiment (Figure 4-53 (a)) gives no indication of material transfer to the tip, while images of the wear track (Figure 4-53 (b)) demonstrates material transfer inside the wear track. A micrograph of the pin contact surface (Figure 4-54 (a)) confirms the absence of material transfer and a micrograph of the wear track illustrates adhered layers inside the track (Figure 4-54 (b)). EDS analyses (Figure 4-55) indicate that the adhered layer consists of aluminum and silicon, which suggest that it is from the 319 Al counterface. The FTIR analyses shown in Figure 4-56, did not pick up any spectra. The only peak identified belongs to carbon dioxide, which is picked up from the surrounding atmosphere during FTIR analyses and indicates a lack of lubricious carbon species on the pin sliding surface. Therefore, from dry nitrogen to vacuum experiment indicates that nitrogen does not promote carbon transfer layers on the countersurface, explaining the absence of LFR.

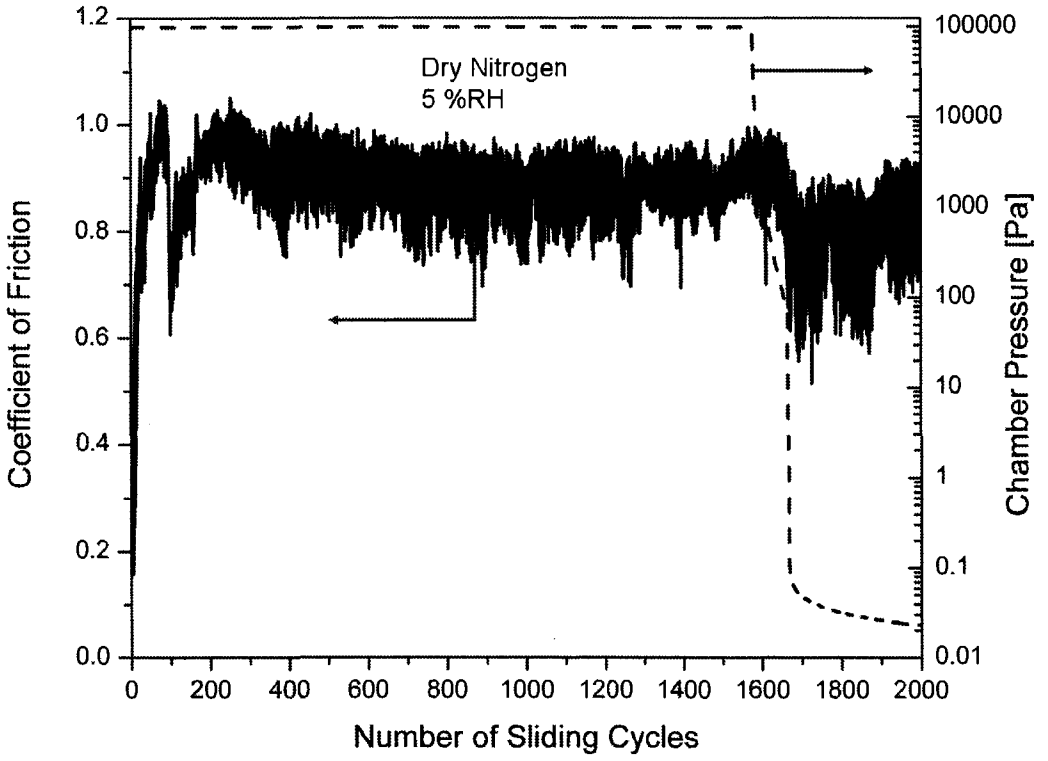

Figure 4-51: Influence of vacuum on the COF after an initial run in period in dry nitrogen for 319 Al sliding against NH-DLC at 5N load and 0.1 m/s speed

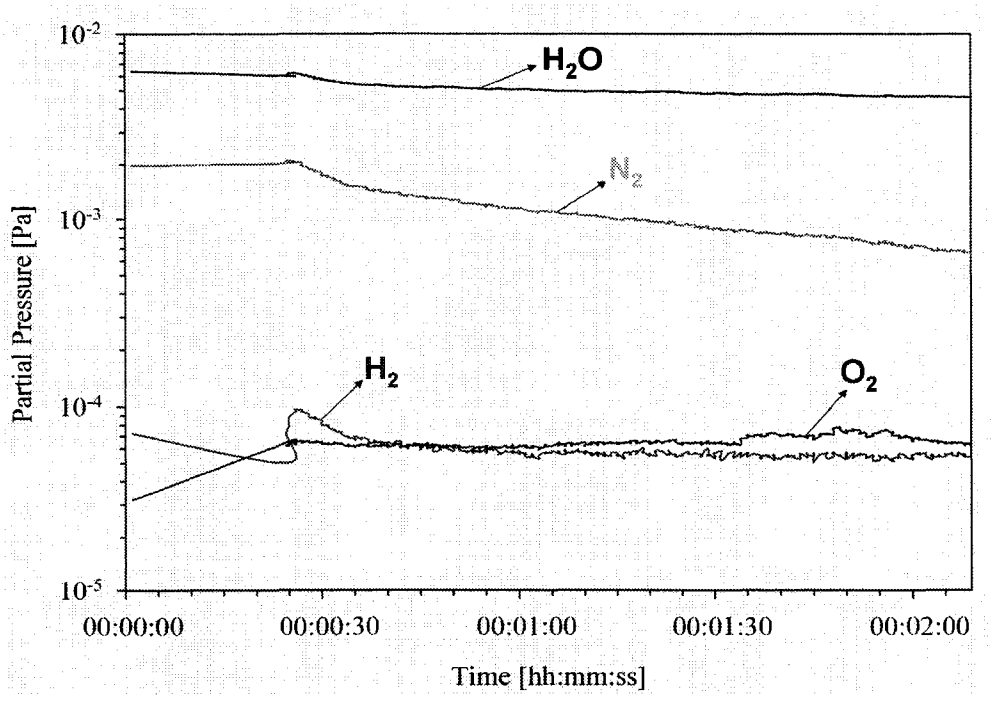

Figure 4-52: RGA analyses of the water, nitrogen, oxygen and hydrogen partial pressures inside the vacuum chamber after sliding in dry nitrogen. RGA was turned on from 1700 to 1900 cycles

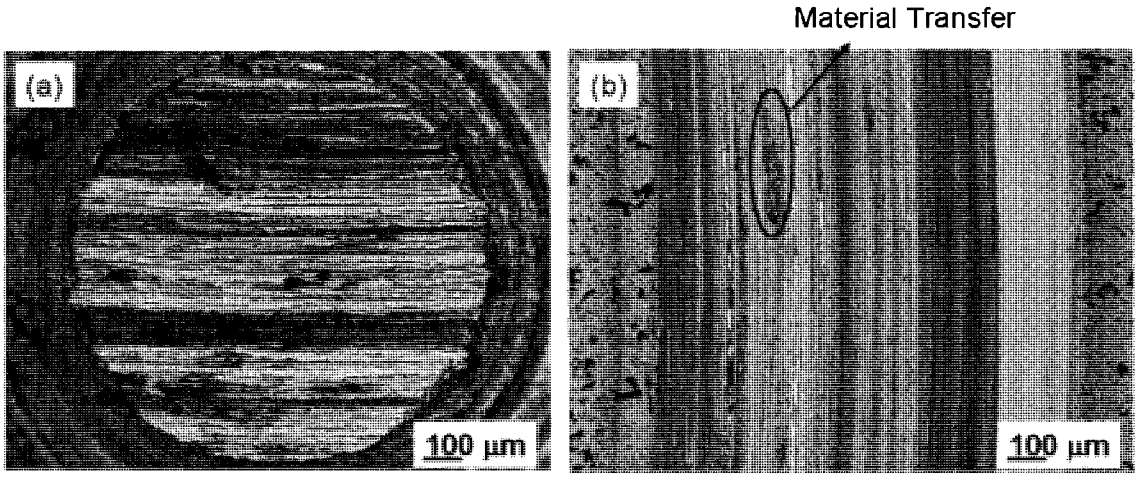

Figure 4-53: Optical image of (a) 319 Al pin surface (b) NH-DLC wear track after 1550 laps running-in in dry nitrogen and 1350 laps in vacuum

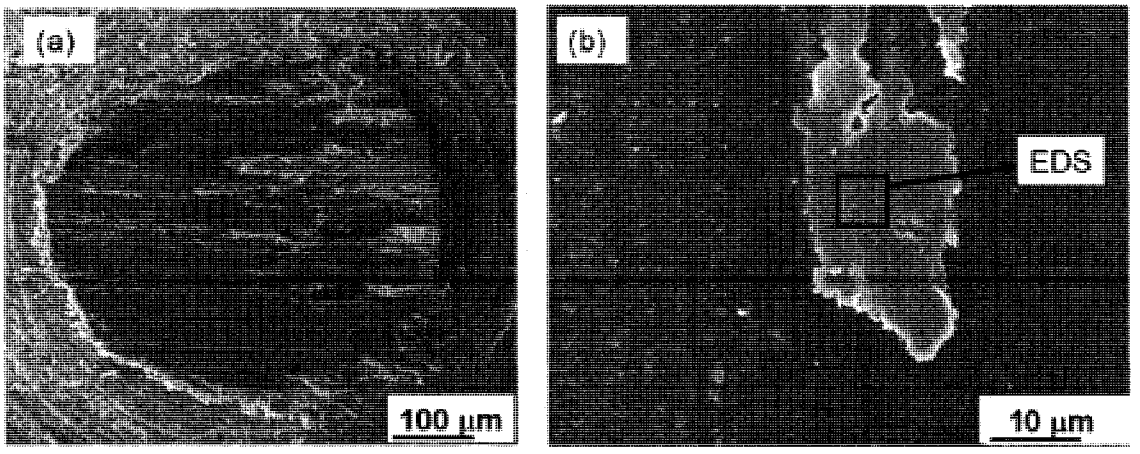

Figure 4-54: Micrographs of the (a) 319 Al pin and (b) NH-DLC track after dry nitrogen to vacuum test

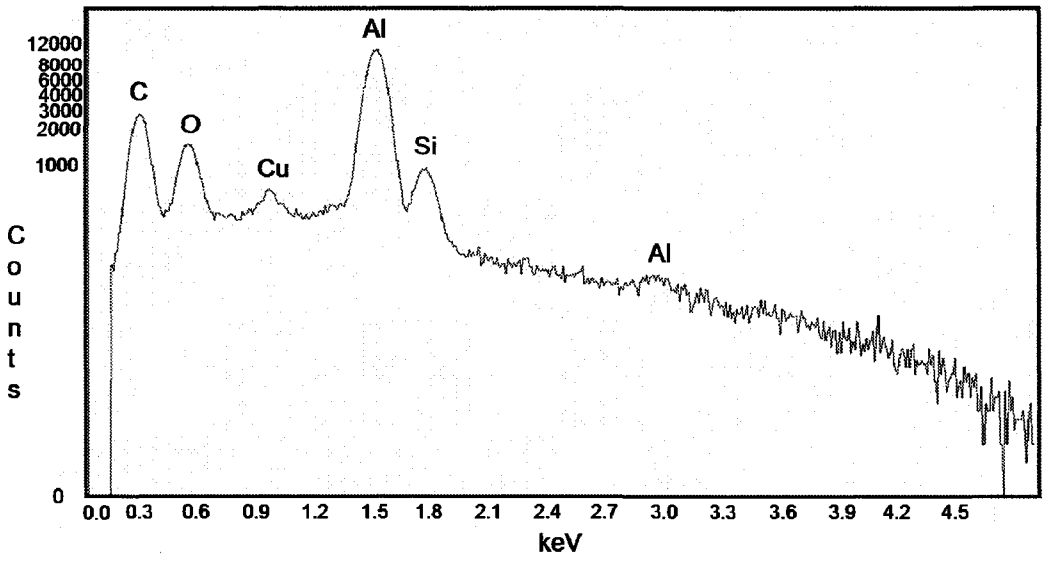

Figure 4-55: EDS spectra of the dry nitrogen to vacuum wear track, obtained from designated area in Figure 4-54 (b)

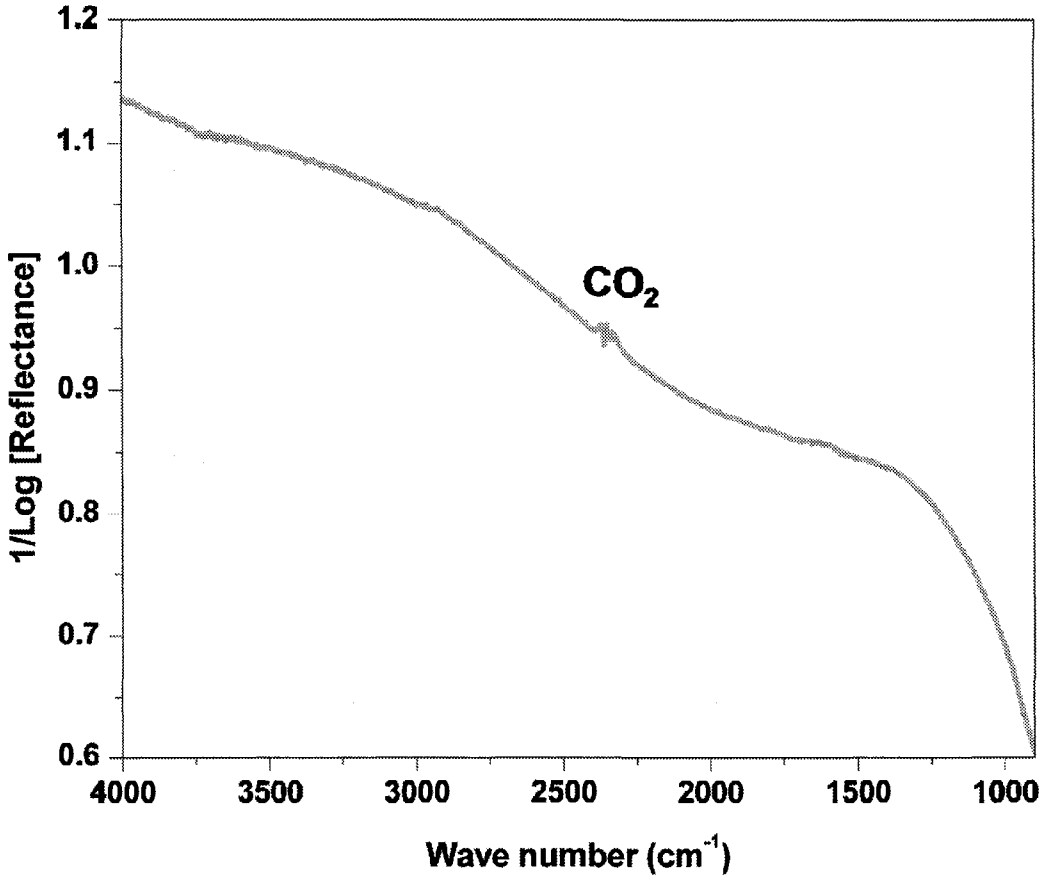

Figure 4-56: FTIR analyses of the Carbon transfer on the 319 Al pin after dry nitrogen to vacuum experiment

4.2.5.3 Effect of Initial Running-in in Dry Oxygen on COF in Vacuum

Initial testing of 319 Al against NH-DLC in an oxygen atmosphere lead to a COF of 0.42 ± 0.15 (Figure 4-57). Similar to dry nitrogen to vacuum experiment, friction generated after the initial run in dry oxygen did not produce a LFR. The initial sliding period in dry oxygen produced a fluctuating COF that started with a friction of 0.2 for the first 1000 cycles and increased to 0.45 ± 0.1 within 200 cycles. The COF dropped slightly at 1100 cycles to 0.35 ± 0.05, and then dropped again to 0.25 ± 0.05, but when the chamber was evacuated at 2100 cycles the COF increased to 0.75 ± 0.2, indicating that carbon transfer layers did not form, which explains the absence of LFR in vacuum. The partial pressure of gases inside the vacuum chamber shown in Figure 4-58 did not vary from what was observed in previous experiments either, as presented in Sections 4.2.5.1 and 4.2.5.2. It follows that the gases inside the vacuum chamber did not influence the LFR, while the presence of carbon transfer layers induced by the presence of air lead directly to a LFR.

An optical image of the 319 Al pin after the experiment (Figure 4-59 (a)) shows no indication of transfer layers, but the wear track (Figure 4-59 (b)) reveals some material adhesion, suggesting aluminum transfer. Similarly, the micrograph of the aluminum pin (Figure 4-60 (a)), gives no sign of transfer layers, while in Figure 4-60 (b) evidence of aluminum transfer inside the wear track is apparent and later confirmed by EDS Figure 4-61). EDS spectra also demonstrate a strong carbon peak as evidence that the NH-DLC coating was not penetrated. Like the dry nitrogen to vacuum experiment, the FTIR spectroscopy results presented in Figure 4-62, did not show any signs of carbon species on the pin surface, only carbon dioxide picked up from the surrounding atmosphere.

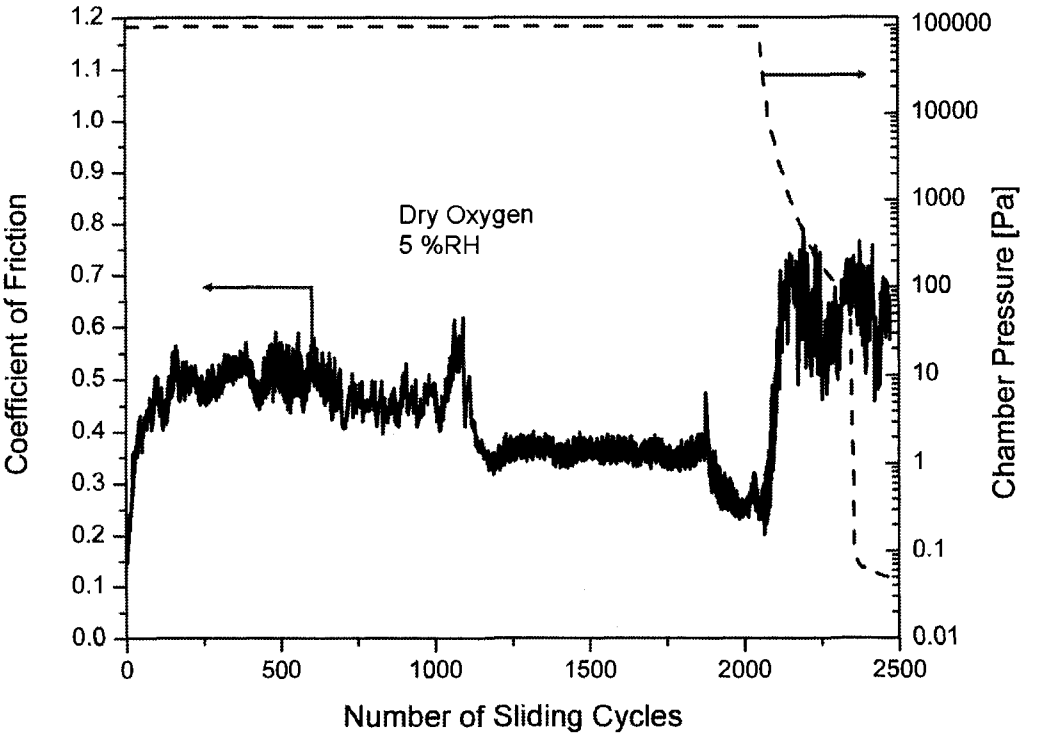

Figure 4-57: Influence of vacuum on the COF after an initial run in period in dry oxygen for 319 Al sliding against NH-DLC at 5N load and 0.1 m/s speed

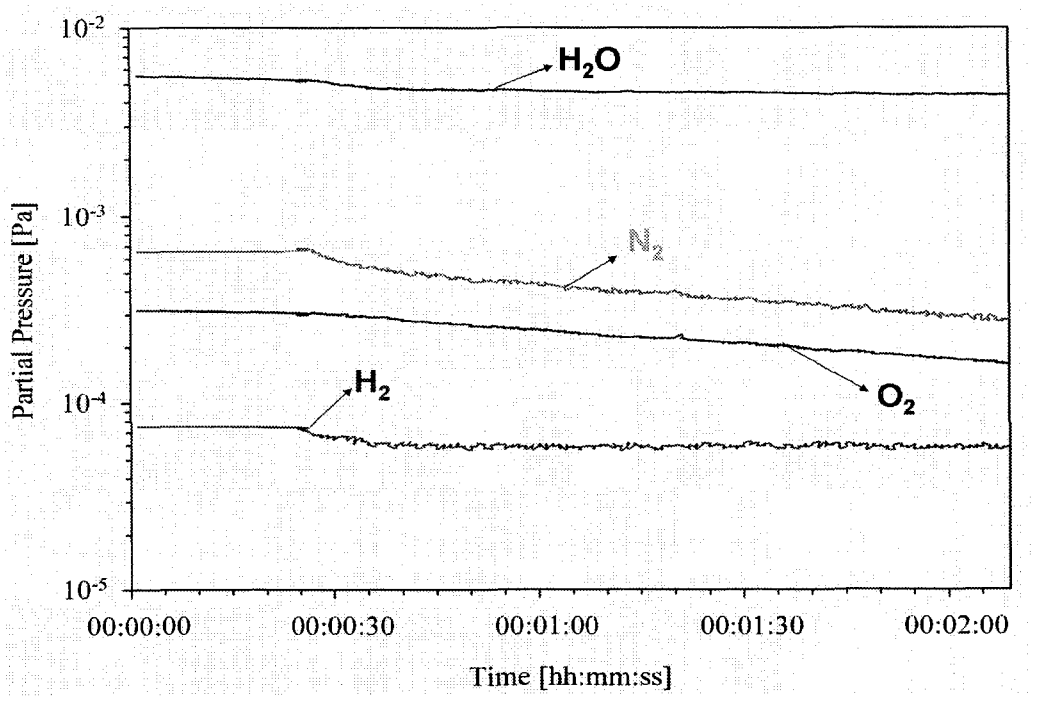

Figure 4-58: RGA analyses of water, nitrogen oxygen and hydrogen partial pressures inside the vacuum chamber after sliding in dry oxygen. RGA was turned on from 2300 to 2400 cycles

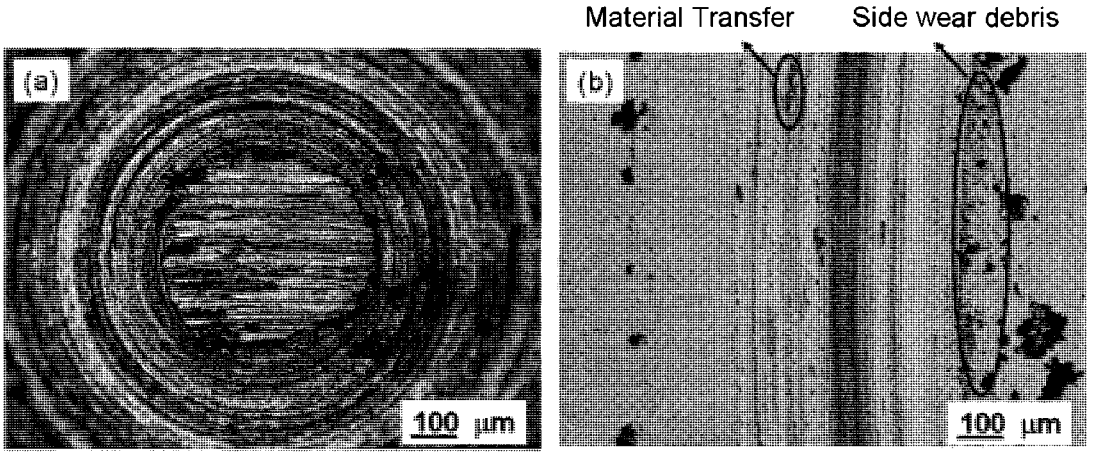

Figure 4-59: Optical image of (a) 319 Al pin surface (b) NH-DLC wear track after 2000 laps running-in in dry oxygen followed by 500 laps in vacuum

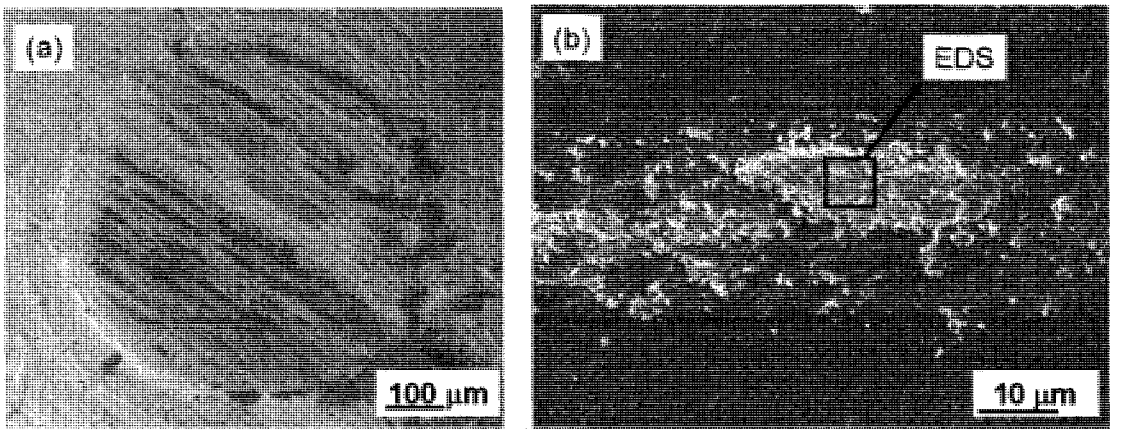

Figure 4-60: Micrographs of the (a) 319 Al pin and (b) NH-DLC track after dry oxygen to vacuum test

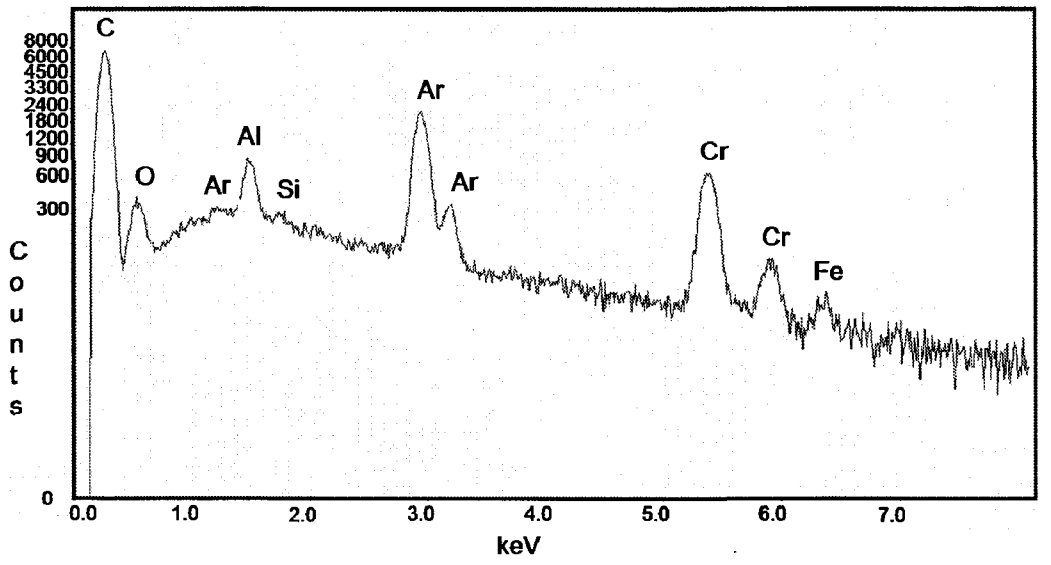

Figure 4-61: EDS spectra of the dry nitrogen to vacuum wear track, obtained from designated area in Figure 4-60(b)

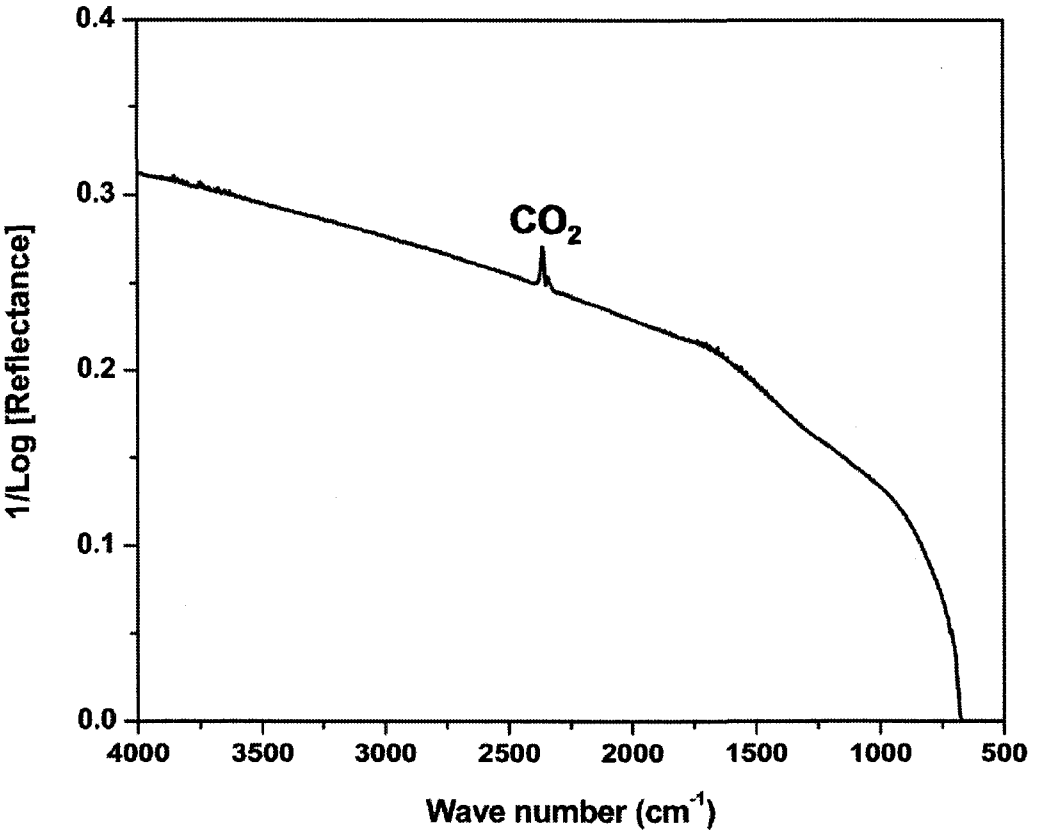

Figure 4-62: FTIR analyses of the Carbon transfer on the 319 Al pin after dry oxygen to vacuum experiment

4.3 Discussion

4.3.1 Friction Behaviour of DLC in Vacuum

Dry sliding in vacuum, the friction behaviour of 319 Al sliding against NH-DLC and H-DLC was seen to be very different. NH-DLC produced a COF of 0.7 ± 0.2 while H-DLC produced a very low COF of 0.02 ± 0.01 (Figure 4-9), despite similar test conditions (5 N load, 0.1 m/s speed and vacuum (0.04 Pa)). However, it was observed that the 319 Al tip was covered by material transfer (Figure 4-11 (a)), that was more likely to be carbon from the H-DLC coating; consequently the contact was altered from Al/H-DLC to C/H-DLC. The NH-DLC coating experiment, the aluminum pin tip was completely worn, with no evidence of material transfer layer was found, only black dust (Figure 4-10 (a)) and a high COF of 0.7 ± 0.2 was produced. In addition to the presence of material transfer, the hydrogen content inside the coating was significantly different. H-DLC contains 40 at% of hydrogen, while NH-DLC only had 1.3 at% of hydrogen. The presence of hydrogen was proven to be a key factor as mentioned in literature [3], [5] hydrogen reduce friction by minimizing surface interactions through reducing the binding energy. Sliding 319 Al against H-DLC resulted in the formation of material transfer to the aluminum pin. As a result, the contact changed from Al/H-DLC to C/H-DLC and the presence of hydrogen lead to low binding energy between C/H-DLC, as calculated by Gardos, to 0.08 eV (COF = 0.02), compared to the 0.4-0.8 eV for C/C layers without hydrogen termination.

As for friction behaviour of 319 sliding against NH-DLC in vacuum, Savage [49] observed the same behaviour in graphite sliding against copper in vacuum. Tests results have shown that the graphite rapidly disintegrated into black dust, producing a COF of

0.8 was produced. The similarity between the tribological behaviour in Savage's results with graphite and those from the current study using NH-DLC illustrates how the NH-DLC coating generates a graphite-like material during sliding that causes similar friction behaviour. Graphite is only lubricious in the presence of water, reducing the atomic interactions between the adjacent stacked hexagonal structures and lubricating the graphitic layers [49], [50]. Thus, the same reasoning can be applied to NH-DLC, attributing the high COF of 0.7, to the collapse of the graphite like structure formed by NH-DLC during sliding and generating black dust.

4.3.2 Friction Behaviour of DLC in Ambient Air

The friction behaviour of both H-DLC and NH-DLC during dry-sliding in ambient air was similar, producing COFs of 0.21 and 0.13, respectively. The 0.08 difference in the COFs for H-DLC and NH-DLC, can be attributed to the difference in the area of material transfer coverage on the aluminum pin observed in the optical images shown in Figure 4-14 (a) and Figure 4-15 (a). The material transfer was proven by literature to be graphite, as Liu and Meletis [48] illustrated TEM analyses and diffraction patterns of the material transfer, showing rings with d-spacing at 0.33 and 0.18 nm, which coincide with (002) and (012) diffractions of graphite. The presence of graphite transfer then modified the contact conditions from Al/DLC to graphite/DLC, which subsequently lead to a lower COF.

The dry-sliding of 319 Al against NH-DLC in an ambient atmosphere at various humidity levels, confirmed the earlier statement regarding NH-DLC's ability to form a graphite-like structure that is lubricious in the presence of water. Results have shown that the COF decreased as the humidity level increased (Figure 4-17), indicating friction

mechanism dependence on water. In addition, the micrographs of the pins after sliding in 22%, 40% and 77% RH presented in Figure 4-19, Figure 4-21, Figure 4-22 and Figure 4-24, which illustrate the presence of carbon transfer layers, stacked similar to a graphite structure. For that reason, it follows that NH-DLC form graphite like layers, which lubricate the sliding interface thus reducing the friction to approximately 0.1 due to presence of water molecules, lubricating the adjacent graphite likes layers.

4.3.3 Why the COF Drops in Vacuum After Initial Running-in in Air

Figure 4-28 shows how 319 Al sliding against NH-DLC produces low friction in vacuum after initial sliding in ambient air. The LFR with a COF of 0.03 ± 0.02 only lasted for 1000 cycles, however, following a high friction regime with a COF of 0.75. Micrographs of the aluminum pin after the high friction regime (Figure 4-31) illustrate that the pin tip was worn off. On the other hand, micrographs of the aluminum during the LFR Figure 4-43, illustrate the presence of carbon layers stacked similarly to a graphite structure. FTIR analyses of these layers revealed the presence of hydrogen (C-H). Section 4.3.1 in the discussion, confirmed that the presence of hydrogen to minimized interactions between the graphite-like layers, which reduce the COF to 0.03 ± 0.02, like the COF produced by H-DLC in vacuum. Other peaks such as (O-H) and (C-O) shown in Figure 4-44, prove the first principle calculation of Qi *et al.* [29] that water dissociate (H_2O = OH + H) as it approaches the carbon surface, bonding with the carbon atom and promoting (O-H) and (C-O) peaks in the FTIR spectra. Therefore, during the initial running-in period in ambient air water dissociated to OH and H and occupied the carbon σ bonds, thus minimizing interactions between the graphite layers and producing a COF of 0.11 ± 0.02. When the chamber pressure dropped, reactive species like oxygen were

evacuated, thus leaving only hydrogen and hydroxyl groups terminating the carbon atoms between the layers. As a result of sliding, the graphite like layers are easily sheared with minimum interactions between adjacent layers due to hydrogen and hydroxyl termination, hence lowering the COF to 0.03± 0.02. This LFR does not last for long, however, due to the depletion or consumption of the lubricious graphite-like layers.

4.3.4 Effect of Initial Running-in Atmosphere on the LFR

It is unclear whether humidity alone is behind the COF drop when the chamber is evacuated, or if some other gas in ambient air is responsible, such as nitrogen or oxygen. Therefore, 319 Al was slid against NH-DLC with an initial running-in in dry air to produce a COF of 0.55 ± 0.1, confirming the importance of water to the sliding graphite layers in ambient air. Once the chamber was evacuated, the COF dropped to 0.05 ± 0.03. FTIR of the pin carbon transfer (Figure 4-50) showed hydroxyl (OH) and carbonate (C-O) peaks, as evidence of water dissociation (H_2O = OH + H). This could only mean that there was enough moisture in the dry air was enough to passivate and lubricate the graphite-like sliding layers.

As for the initial running-in in dry nitrogen and dry oxygen, followed by sliding in vacuum, test results showed no sign of a LFR, which indicates that graphite-like layers were not formed. This is confirmed by micrographs of the aluminum pin Figure 4-54 and Figure 4-60. Furthermore, FTIR analyses of the aluminum tip shown in Figure 4-56 and Figure 4-62, confirm the absence of carbon and hydrogen. The RGA of the chamber during vacuum in both tests reveal no deviation from analyses performed during vacuum with prior initial sliding in dry air and ambient air, confirmation that gas species inside the vacuum chamber are at very low concentrations and do not influence the LFR.

Chapter 4: Part II

Lubricated Sliding

This study investigated the lubricated sliding behaviour of H-DLC and NH-DLC by generating the boundary lubrication (BL) portion of the Stribeck curve for each coating to identify the lubrication regimes and the range of speeds at which BL occur. Then, friction behaviour under BL regime was then further explored by analyzing the counterface before and after sliding, to get an idea what is happening to the couterface. Finally, both H-DLC and NH-DLC were initially tested dry, in ambient air and then Dexron III lubricant was added to observe the possible influence of carbon transfer that were formed in ambient air on the COF in lubricated sliding.

4.4 Stribeck Curve

The boundary and mixed lubrication portion of Stribeck curve was generated. Balls with 6 mm Ø of AISI 52100 steel were tested against H-DLC, NH-DLC coatings as well as uncoated 52100 steel for reference at 0.5, 1.0, 10.0, 100.0, 200.0, 500.0 and 600.0 mm/s for 150 cycles at a 5 N normal load at each speed, as shown in Figure 4-63. The average COF of each test was plotted against the corresponding lambda ratio (λ = oil film thickness / surface roughness), then calculated using the oil film thickness for point contact, Equation A.2 in Appendix A.

Figure 4-64 illustrates the BL regime ($\lambda < 1$) of the Stribeck curve for uncoated 52100 steel, NH-DLC and H-DLC coatings. At λ of approximately 0.3, the COF experiences a regime transition from BL to mixed lubricated (ML). At $\lambda < 0.3$, the COF of the uncoated steel and both DLC coatings followed the same trend, starting with a COF of 0.11 at $\lambda = 0.004$ and as the λ increased to 0.25, the COF gradually decreased to

0.085 (Figure 4-64). The COF in this region ($\lambda < 0.3$) falls within 0.7 and 0.2, which is the typical range for COF under BL [54].

However, at $\lambda > 0.3$, the COF NH-DLC dropped, while H-DLC and steel maintained the steady decrease observed at $\lambda < 0.3$. For example, the COF dropped from 0.085 at $\lambda = 0.25$ to 0.063 at $\lambda = 0.4$ in the presence of the NH-DLC coating, while the COF only dropped from 0.085 at $\lambda = 0.25$, to 0.072 at $\lambda = 0.4$ for uncoated steel and H-DLC. These Stribeck curve results illustrate that the NH-DLC coating has a greater influence on the COF reduction past the transition regime line.

Surface profile of the ball after the 150 cycles at $\lambda = 0.03$ (Figure 4-65) illustrate that the highest amount wear observed on the steel ball which ran against NH-DLC and the least wear observed for the steel ball which ran against H-DLC. The same trend was seen for all lambda ratios (i.e. $\lambda = 1.5$ shown in Figure 4-66). Overall, it was found that wear rates decreased as lambda ratio increased (Figure 4-67). This trend was expected, since higher lambda ratio means thicker oil film from Equation A.2 in Appendix A, which prevents metal/metal contact and lowers wear rate.

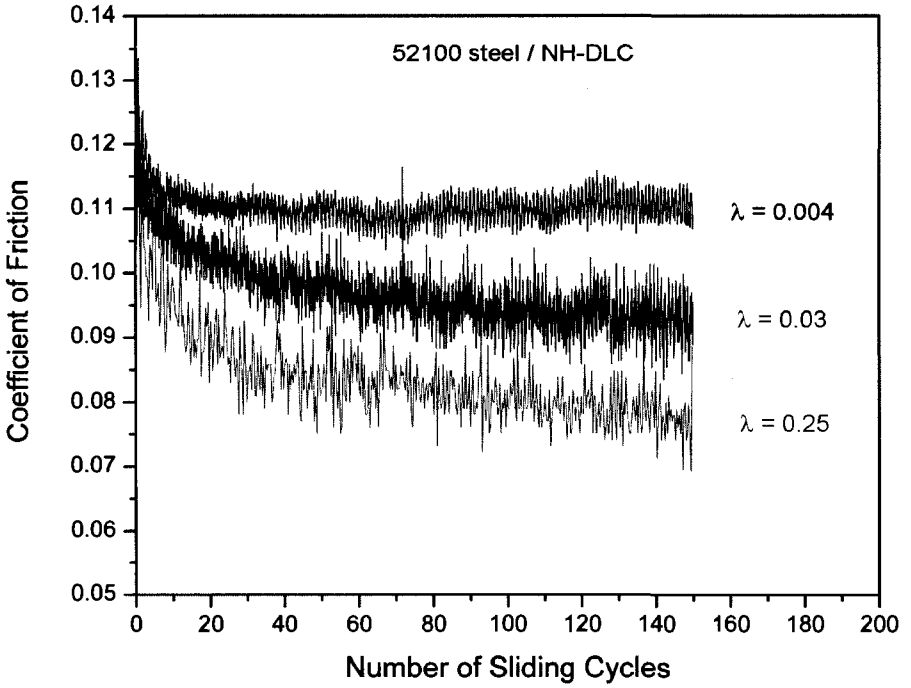

Figure 4-63: Friction results for 52100 steel sliding against NH-DLC, in the presence of Dexron III ATF at 0.5 mm/s, 10 mm/s and 600 mm/s, which coincide with lambda ratio of 0.004, 0.03 and 0.25 respectively

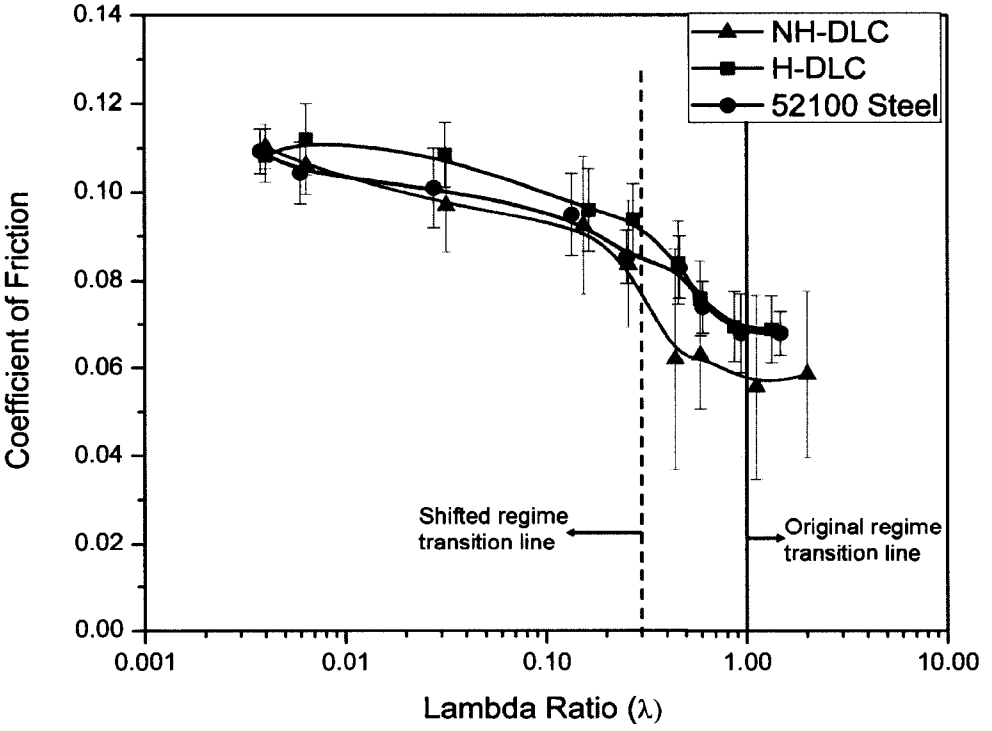

Figure 4-64: Stribeck curve using Dexron III oil for point contact at room temperature, η = 0.0538 Pa-s

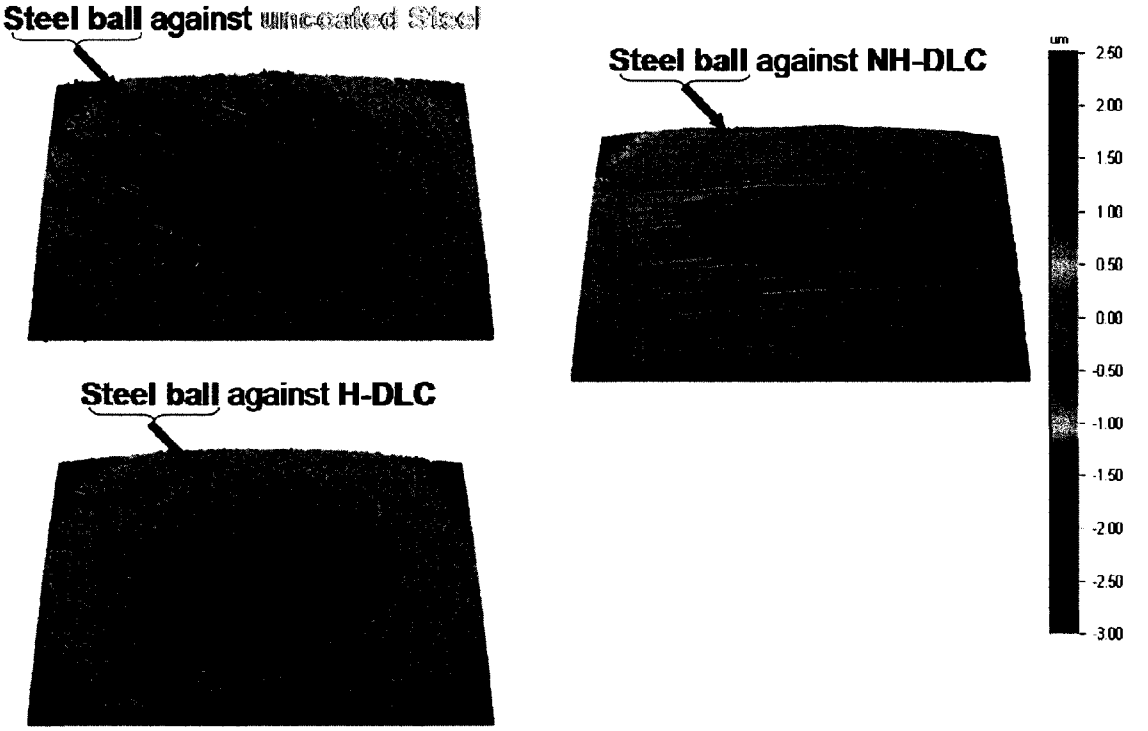

Figure 4-65: Surface profile of the 52100 steel ball wear scar after the wear test at 0. 5 mm/s, which corresponds to λ= 0.03

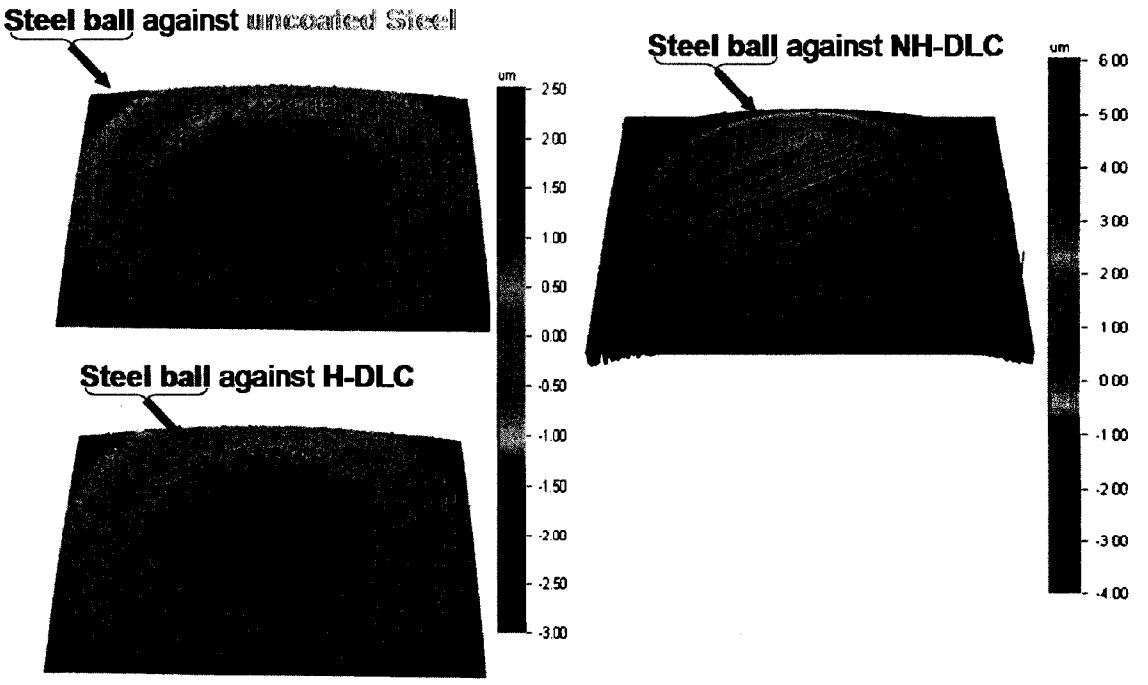

Figure 4-66: Surface profile of the 52100 steel ball wear scar after the wear test at 0. 600 mm/s, which corresponds to λ= 1.5

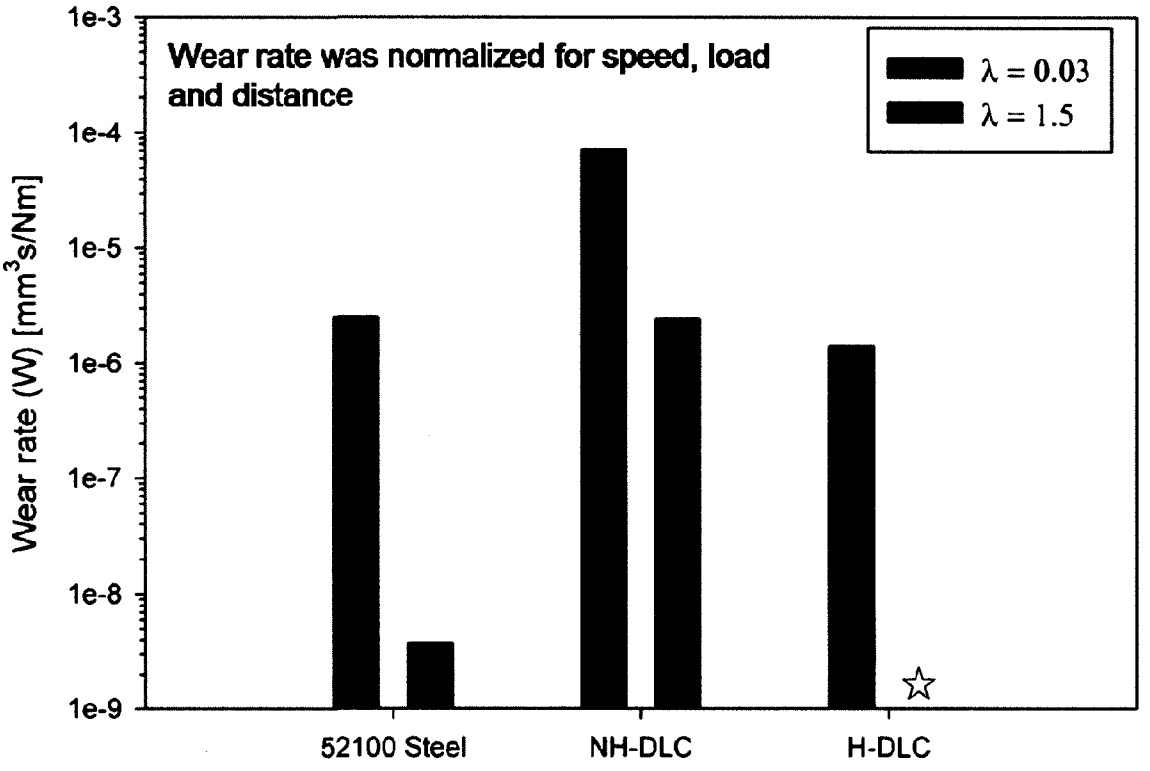

Figure 4-67: Wear rates of the 52100 steel ball after running against 52100, NH-DLC and H-DLC for 150 laps at λ= 0.03 and 1.5,☆ represents an undefined wear rate or the wear rate could not be quantified

4.5 Boundary Lubrication

A 52100 steel ball was tested against DLC coatings for 5000 laps, at 100 mm/s and 5 N load, corresponding to $\lambda = 0.2$. Results presented in Figure 4-68 reveal that H-DLC has a steady COF of 0.11 ± 0.01, meanwhile NH-DLC generated a steady-state COF of 0.07 ± 0.005 after 1000 cycles of run-in period, indicating a change in the lubrication regime.

Optical images (Figure 4-69) of the ball after the wear test show no sign of a tribolayer on either ball, but the steel ball that ran against H-DLC had a scar diameter of 150 μm (Figure 4-69 (a)), which is half of the 300 μm ball scar diameter produced by the NH-DLC (Figure 4-69 (b)).

The hertzian pressure (Appendix C) was calculated initially before sliding (P_i) and after sliding (P_f), presented in Table 4-2. The initial hertzian pressure for 6 mm Ø 52100 steel ball against H-DLC and NH-DLC were 0.85 and 1.02 GPa respectively. After 5000 sliding cycles, the hertzian pressure was calculated to be 0.42 and 0.11 GPa, by calculating the contact area from the ball wear scar diameter shown in Figure 4-69. The calculation reveals that the contact pressure dropped significantly, about one order of magnitude for 52100 steel against NH-DLC, which could be behind the friction drop shown in Figure 4-68.

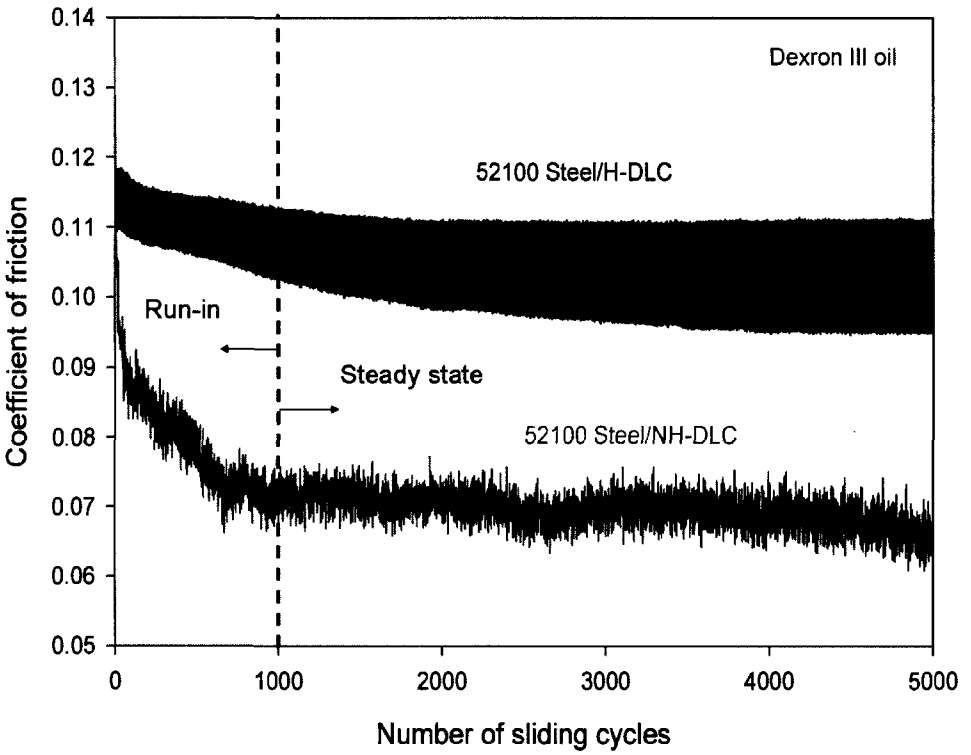

Figure 4-68: Ball-on-disc wear test of AISI 52100 steel ball sliding against H-DLC and NH-DLC at 100 mm/s, 5 N load for 5000 sliding cycles, which correspond to λ = 0.15

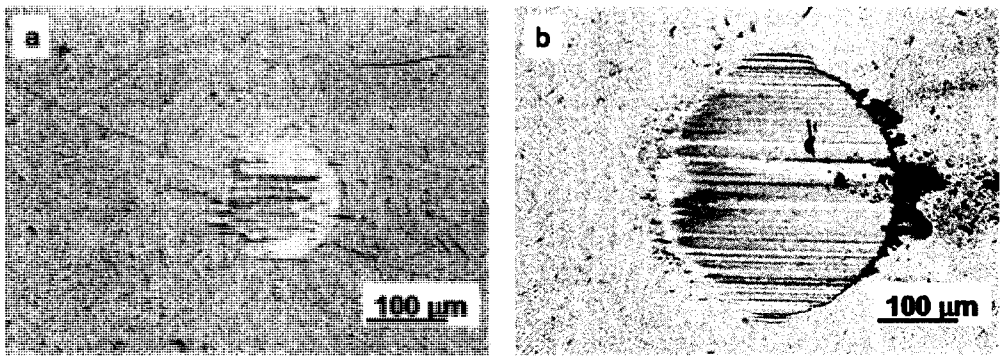

Figure 4-69: Wear scar of the 52100 steel ball after running against (a) H-DLC (b) NH-DLC for 5000 sliding cycles, with 5N load and 100 mm/s speed

Table 4-2: Calculated hertzian contact pressure and contact area before and after sliding in BL

Coating	A_i [m^2] Calculated	A_f [m^2] Measured	P_i [GPa]	P_f [GPa]
52100 steel / H-DLC	8.79×10^{-9}	1.77×10^{-8}	0.85	0.42
52100 steel / NH-DLC	6.65×10^{-9}	7.06×10^{-8}	1.02	0.11

4.6 Effect of Initial Dry Running-in on Lubricated Sliding

A 52100 steel ball was slid against NH-DLC and H-DLC at 100 mm/s at a 5 N load, corresponding to $\lambda = 0.2$. The experiment initially ran dry in ambient air without any fluid or oil, and then Dexron III oil was added. Figure 4-70 shows that the COF of 52100 sliding against NH-DLC starts at 0.15 and climb 0.23. At 2500 cycles, the COF reaches a steady state of 0.16 ± 0.005, then at 3700 cycles, Dexron III was added and the COF immediately responded by dropping to 0.098 ± 0.005. As for 52100 steel sliding against H-DLC, the friction started relatively high at 0.2 and within 500 cycles, it dropped to a low steady state COF of 0.051 ± 0.004. However, once Dexron III was added, the COF immediately increased to 0.1 ± 0.002.

Optical images of the ball wear scar before adding the oil, reveal the presence of carbon transfer on both steel balls slid against H-DLC (Figure 4-71 (a)) and NH-DLC (Figure 4-71 (b)). However, after the lubricated sliding period, the carbon transfer on the balls was washed off those that slid against both H-DLC (Figure 4-72 (a)) and NH-DLC (Figure 4-72 (b)).

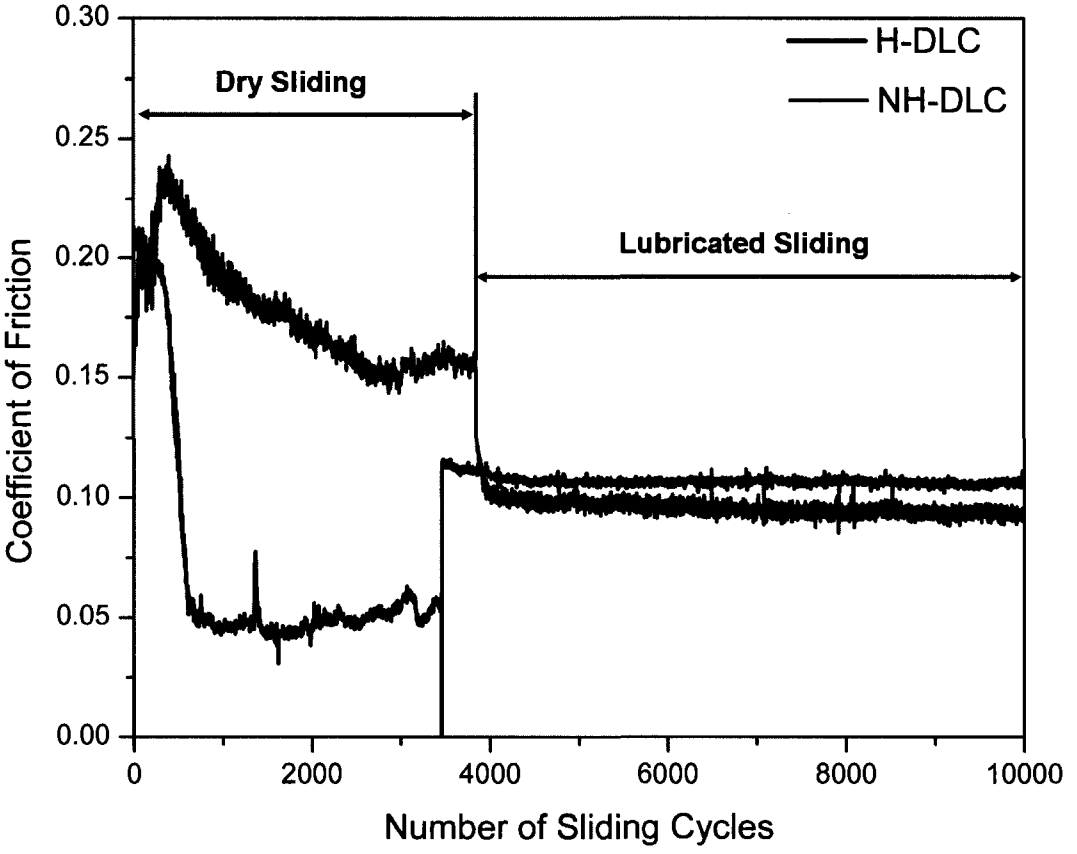

Figure 4-70: Ball-on-disc wear test with initial dry-sliding of steel ball sliding against H-DLC and NH-DLC followed by lubricated-sliding at 100 mm/s, 5N load

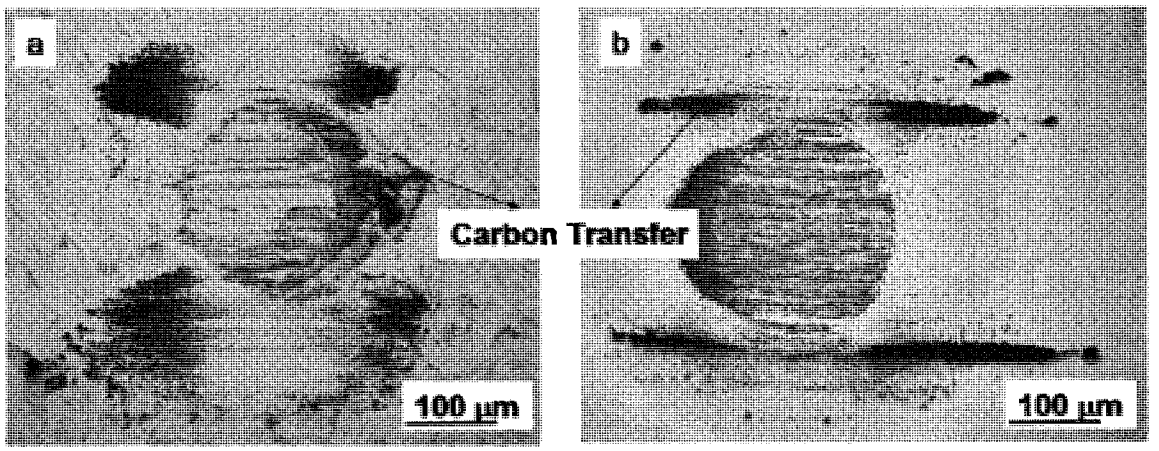

Figure 4-71: 52100 steel ball after dry sliding in air against (a) H-DLC (b) NH-DLC

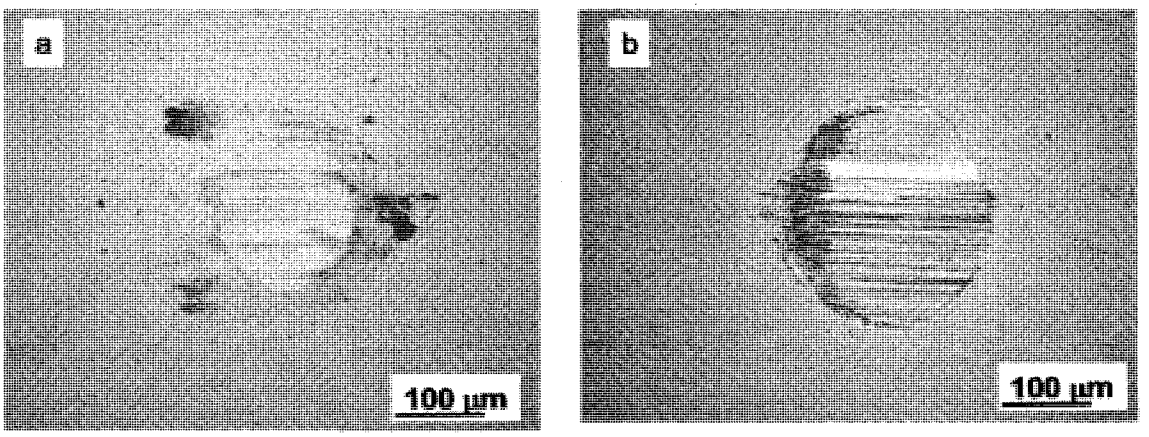

Figure 4-72: 52100 steel ball after lubricated sliding against (a) H-DLC (b) NH-DLC

4.7 Discussion

The generated Stribeck curves displayed in Figure 4-64, illustrate that beyond λ = 0.3, the NH-DLC COF starts to drop, while H-DLC and steel maintain their steadily decreasing slope. This indicates that NH-DLC induced an early transition from BL and ML at λ = 0.3, but this transition was not suppose to occur until λ = 1 suggesting that the NH-DLC coating must have altered the contact conditions. NH-DLC also displayed a significantly worn ball tip compared to the balls that ran against H-DLC and steel (Figure 4-66). The worn ball implys that the NH-DLC coating reduced the contact pressure by increasing the contact area and transforming the point type contact to line type contact. This would explain the early transition from BL to ML and the relatively low COF (0.063) compared that (0.073) produced by H-DLC and uncoated steel at $\lambda > 0.3$.

The type of run-in behaviour observed for NH-DLC in the first 1000 cycles (Figure 4-68), confirms changes in the contact conditions, which is described by Blau [55] as frictional break-in. This type of run-in behaviour is attributed to a reduction in the contact pressure and smoothing of the mating surface, as illustrated by Xu *et al.* [56] in lubricated sliding. These authors tested SiN against itself in water and they observed that during the run-in period, mechanical wear dominated where contact pressure reduction and surface smoothing occurred. After the running-in period, the wear mechanism changed from mechanical to tribochemical dominated wear, reaching a steady-state COF. This type of behaviour was also observed in the current study (Figure 4-68), indicating that the NH-DLC coating lowered the COF under BL by reducing the contact pressure.

This was confirmed, when the steel balls were examined after the experiment, it was observed that the ball sliding against NH-DLC had a wear scar diameter was twice

that of wear scar produced by the H-DLC (Figure 4-69), plausibly because NH-DLC is 3 GPa harder than H-DLC. Consequently, the contact pressure decreased by half for 52100 steel against H-DLC and by one order of magnitude for 52100 steel against NH-DLC Table 4-2. This confirmed the earlier statement that in BL, NH-DLC lowers the contact pressure by wearing the mating surface and changing the lubrication regime. Consequently, the H-DLC coating produced a COF of 0.11, which was higher than the NH-DLC coating with a COF of 0.07.

Experiments with an initial dry run-in followed by lubricated sliding (Figure 4-70), show that oil does not lubricate the low shear carbon transfer formed during the initial dry-sliding. When the Dexron III was introduced after the initial dry-sliding period, with carbon transfer layers on the pin, both H-DLC and NH-DLC coatings produced a COF of 0.1, which is a typical value for uncoated 52100 steel [57]. However, in this study (Figure 4-70) it was observed that in air H-DLC is capable of producing very low COF of 0.05, which is lower than lubricated sliding with COF of 0.1, suggesting that there is potential for H-DLC to replace oils and eliminate BL.

CHAPTER 5

Conclusions

The purpose of this study was to identify the friction mechanisms of DLC coatings in dry sliding and lubricated sliding, specifically in the boundary lubrication regime. The mechanism of dry-sliding was explored by testing 319 Al pins against both NH-DLC and H-DLC coatings under various environments, including vacuum (0.4 Pa), ambient air (40% RH) and humid air (22%, 40% and 77% RH). In addition, the influence of an initial running-in gas on the friction in vacuum (such as dry air, dry nitrogen and dry oxygen atmospheres) was investigated. For lubricated sliding, the boundary lubrication (BL) portion of the Stribeck curve was generated for uncoated 52100 steel, H-DLC and NH-DLC coatings. Then a two phase experiment was conducted, initially in dry running-in followed by, lubricated sliding.

5.1 Tribological Behaviour of DLC in Dry Sliding

5.1.1 Friction in Ambient Air and in Vacuum

1) The friction of the NH-DLC coating (COF = 0.13 ± 0.015) was lower than that of the H-DLC coating (COF = 0.21 ± 0.018) in ambient air at 40% RH, due to the formation of carbon transfer layers on the aluminum counterface. The difference in the COF is attributed to the amount of carbon transfer layers formed on the aluminum pin.
2) The COF of 319 Al sliding against NH-DLC decreased from 0.19 ± 0.05 to 0.12 ± 0.02 and 0.09 ± 0.01 as the humidity increased from 22% to 40% and to 77% RH.

The reduction in the COF observed between 319 Al and NH-DLC as humidity increased was attributed to water dissociation, the formation of -H and –OH molecules, which terminate the free carbon σ bonds on the surface. The formation of lubricious graphite lead to COF reduction. FTIR analyses of the transfer layers confirmed the presence of -H and -OH, confirming water dissociation in the initial sliding in ambient air.

3) 319 Al sliding against H-DLC in vacuum resulted in a very low COF of 0.02 ± 0.0102, while 319 Al sliding against NH-DLC in vacuum lead to a high COF of 0.9 ± 0.2. A possible explanation was that H-DLC is capable of forming carbon transfer on the aluminum counterface, which prevented surface interactions. The lack of carbon transfer on the aluminum pin for NH-DLC, combined with a high surface energy of, induced high surface interactions with the aluminum counterface, that produced a high COF.

5.1.2 Effect of Initial Running-in on Reduction of COF in Vacuum

1) The initial dry-sliding in ambient air lead to a reduction in the COF between 319 Al and NH-DLC sliding surfaces when the chamber pressure was reduced to reach vacuum (0.04 Pa). This behaviour is due to the presence of moisture in the air, which caused lubricious graphite to form on the tip of the aluminum pin. When the chamber was evacuated, these layers were sheared, which lowered the COF from 0.1 in ambient air to 0.02 ± 0.01in vacuum. Once the layers were consumed, the contact changed back to Al/DLC and thus the COF increased to 0.7.

2) Lubricious carbon transfer layers also formed in the presence of dry air. FTIR analyses of the transfer layers that formed in dry air confirmed the presence of H and OH, indicating water dissociation. The COF of 0.5 in dry air was thereby reduced again to a very low value of 0.03.

3) No evidence of carbon transfer layers was found to form in the presence of dry oxygen or dry nitrogen atmospheres, so the aluminum to NH-DLC contact was maintained. Consequently, friction did not decrease when the chamber was evacuated.

5.2 Tribological Behaviour of Lubricated Sliding

1) The NH-DLC coating produced a lower COF of 0.06 compared to H-DLC and uncoated 52100 steel (0.83), promoting an early regime transition, from boundary to mixed lubrication regime at $\lambda = 0.3$.

2) The early regime transition produced by NH-DLC is due to the mechanical wearing of the counterface (52100 steel ball), which lead to an increase in the contact area. This, reduction of the contact pressure and consequently, changing the lubrication regime, leading to a lower COF.

3) It was also observed that dry sliding of H-DLC out perform lubricated sliding by producing a COF of 0.05 in dry and 0.1 in BL condition. Therefore, possible changes could be made for H-DLC to replace ATF and running transmission dry to eliminate BL.

5.3 Suggestions for Future Work

A. Investigate the friction and wear behaviour of DLC coatings while sliding in humid oxygen and humid nitrogen atmospheres. The purpose of these investigations is to identify if either oxygen or nitrogen promote better dissociation of water.

B. Explore the effect of metallic dopants (i.e. Ti, W and WC) and non-metallic dopants (i.e. P, S, N and F) on the tribological behaviour of DLC coatings, to identify which dopant is ideal for dry machining of Al.

C. Examine the behaviour of DLC coatings under lubricated conditions with different oil viscosities and compositions (75W90, 5W30, 10W30) to compare with base stock oil (PAO). These tests will help to clarify whether viscosity affect the friction mechanism under BL.

D. Examine the effects of dopants on the BL regime and identify which dopants work more effectively under BL conditions.

APPENDICES

A. Lubrication Regimes

Lubricants are added to minimize wear by separating the sliding surfaces. The separation depends on the fluid properties (i.e. viscosity) and conditions such as load, speed, roughness and temperature. Lubricants have three regimes: hydrodynamic (HL), elasto-hydrodynamic (EHL) and boundary lubrication (BL). The boundaries between regimes are governed by the λ (Equation A.1), the ratio between film thickness, calculated according to Hamrock and Dowson for elliptical contact [58] (Equation A.2) and the root mean square of the two surface roughnesses (Equation A.3). In the film thickness equation the terms R_x, U, G, W and k represent the radius of curvature of the bearing in the x-direction, dimensionless speed parameter (Equation A.4), dimensionless materials parameters (Equation A.5), dimensionless load parameter (Equation A.6) and the ellipticity parameter (Equation A.7) respectively. The effective elastic modulus is represented by E' (Equation A.8).

$$\lambda = h_{\min} / \sigma^* \qquad \text{A-1}$$

$$h_{\min} = 3.63 R_x U^{0.68} G^{0.49} W^{-0.073} (1 - e^{-0.68k}) \qquad \text{A-2}$$

$$\sigma^{*2} = R_{q1}^2 + R_{q2}^2 \qquad \text{A-3}$$

$$U = \frac{\eta V}{E' R_x} \qquad \text{A-4}$$

$$G = E' \alpha, \qquad \text{A-5}$$

$$W = \frac{F}{E' R_x^2} \qquad \text{A-6}$$

$$k = 1.03\left(\frac{R_x}{R_y}\right)^{0.64} \qquad \text{A-7}$$

$$E' = \frac{2}{\frac{1-v_1}{E_1} + \frac{1-v_2}{E_2}} \qquad \text{A-8}$$

Where η is the oil viscosity, V is the speed, R_x is the radius of curvature of the bearing in the x-direction, E' is the composite elastic modulus, α is the pressure viscosity coefficient, F is the load applied and v is the poisons ratio.

The different regimes can be presented graphically by the Stribeck curve (Figure A-1). Hydrodynamic lubrication is observed when $\lambda > 3$ at low loads, high speeds or in very viscous fluid. Under these conditions, the lubricant is relatively thick and the viscous forces support the normal load. Elasto-hydrodynamic (EHL) or mixed is observed at $1 < \lambda < 3$ due to high-localized pressures leading to a formation of a thin lubricant film, which result in asperity contact. However, asperity contact only leads to elastic deformation because the lubricant carries most of the load.

As for boundary lubrication (BL), usually occurs at high loads and low speeds are applied, leading to very thin next to no lubricant present between the sliding surfaces and direct contact of asperities occur and therefore $\lambda < 1$. This is commonly observed in bearings, piston rings, pumps and transmission [59]. The lubricant in this regime functions in a different way, where oil molecules are adsorbed on the surface to form a hard load-supporting phase and a soft easily sheared phase to reduce friction [60].

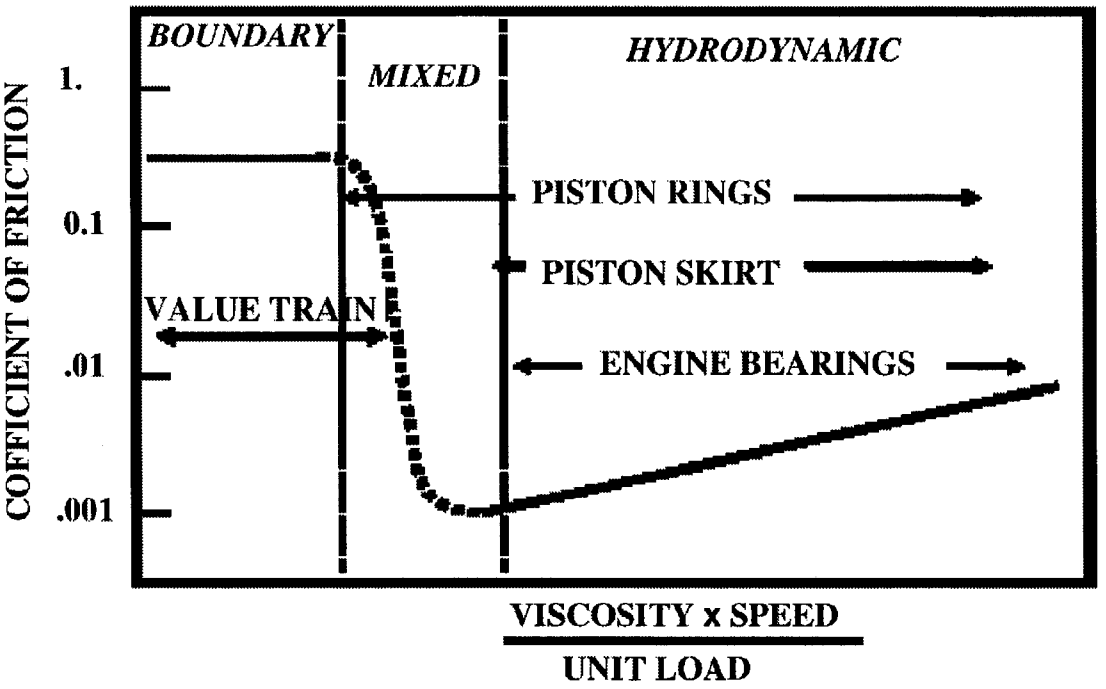

Figure A-1: Stribeck curve [59]

B. Friction Modifiers

Friction modifiers (FM) are additives added to the base oil to eliminate the BL regime, and they are commonly used in automatic transmission fluid (ATF) to insure a smooth shifting between gears. FM are long chains carbon chains (10 or more carbon atoms) with either carboxylic acids, phosphoric acids or amines, amides and imides polar heads at the end [61]. These polar heads adsorb to the metallic surface and provide a buffer zone layer, which prevents metal/metal contact (Figure B-1).

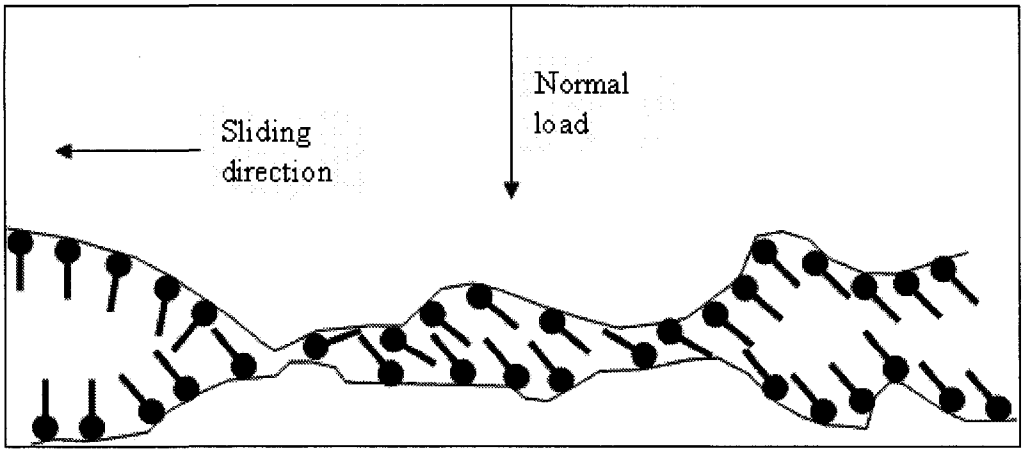

Figure B-1: Adsorbed oil mono-layer on the sliding surfaces [61]

The effective in formation of these protective layers depends on the chemistry of the additives. For example, polar groups with strong polarity have greater tendency to adsorb to the metallic surface and forming stronger and thicker protective layers compared to weaker polarity groups as shown in

In addition, smaller polar head groups promote stronger and more stable films with closely-packed molecules. The polar chains adsorb on the surface, aligning themselves perpendicular to the surface so that the adsorption force was estimated to be around 13 Kcal/mol [61]. Consequently, hydrogen bonding along the sides of the chains

induced cohesive forces between the hydrocarbon tails, promoting the parallel orientation of the adsorbed chains. Adsorptions of polar groups are also greatly influenced by the operating temperature. Higher temperatures lead to de-sorption of the polar head molecules, which weakens the adsorbed protective layer. According to Persson [62] adsorption of the polar group on the surface is affected by the surrounding atmosphere. For example, in humid atmospheres water molecules adsorb on the surface, which hinders polar group adsorption to the surface.

Adsorbed chain length also contributes to film stability and formation. Papay [61] compared different acids with different chain lengths, showing longer chains were observed to form thicker adsorbed layers on the metallic surface (Table B-1).

Table B-1: Adsorption film thickness of acid solutions (0.025% in benzene) [61].

ACID	CHAIN LENGTH (in Carbon Atoms)	FORMULA	MW	FILM THICKNESS, Å	
				at 28 psi	at 2.8 psi
Phenylstearic	~22	C6H5(CH2)17COOH	360	1300	1500
Stearic	18	CH3(CH2)16COOH	284	800	1100
Oleic	18	C8H17CH=CH(CH2)7COOH	282	700	1000
Heptanoic	7	CH3(CH2)5COOH	150	600	800
Benzoic	~5	C6H5COOH	122	400	700
Sebacic	~5	CH2CH2CH2CH2COOH l CH2CH2CH2CH2COOH	202	300	500

C. Surface Hardness and Elastic Modulus Calculation

Surface hardness and the Elastic modulus can be calculated according to Oliver and Pharr's method [39] from the load vs displacement data obtained by Nano-indentation as shown in Figure C-1.

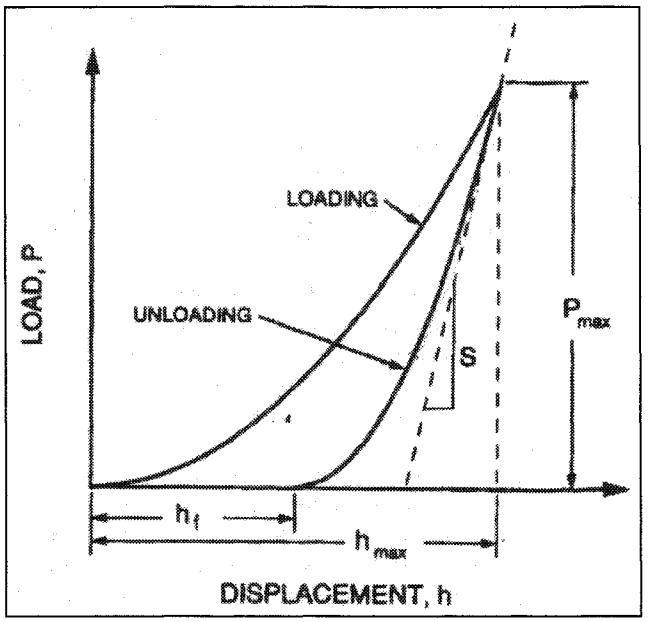

Figure C-1: Schematic presentation of load vs displacement [39]

The stiffness (S) is calculated as the slope of a linear fitting for the upper 1/3 of the unloading region from load vs displacement results. Therefore, the reduced Elastic modulus (E_r) can be computed from the stiffness (Equation C.1), with (P) as the load, (h) as the displacement and (A) as the projected area of the elastic contact.

$$S = \frac{dP}{dh} = \frac{2}{\sqrt{\pi}} E_r \sqrt{A} \qquad \text{C-1}$$

Knowing the Poison's ratio for the specimen ν, the Elastic modulus and the Poison's ratio for the indenter, E_i and ν_i respectively, Elastic modulus of the specimen can be calculated accordingly from Equation C.2.

$$\frac{1}{E_r} = \frac{(1-\nu^2)}{E} + \frac{(1-\nu_i^2)}{E_i} \qquad \text{C-2}$$

Specimen's surface hardness (H) is computed as the ratio between the maximum load (P_{max}) and (A) the projected area of indent (Equation C.3).

$$H = \frac{P_{max}}{A} \qquad \text{C-3}$$

The projected area can be determined from the geometry of the indent. For example, the Berkovich indenter is a three-sided pyramid and therefore, the area is 24.5 h_c^2 from Figure C-2

$$h_c = h_{max} - h_s \qquad \text{C-4}$$

$$h_s = \varepsilon \frac{P_{max}}{S} \qquad \text{C-5}$$

Where ε is a geometrical constant (i.e. for conical indenter ε = 0.72, ε = 1 for flat punch and ε = 0.75 for a Berkovich indenter)

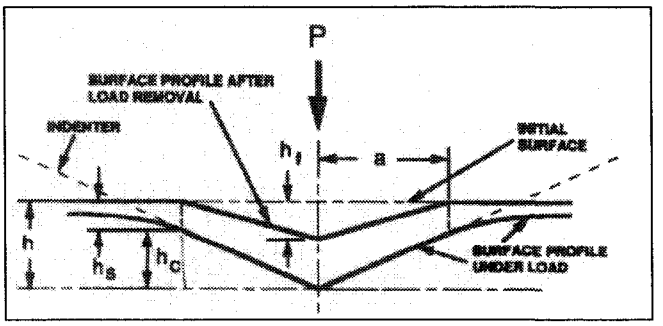

Figure C-2: Schematic drawing of the indent [39]

D. CONTACT PRESSURE

The contact pressure is calculated according to the Hertzian analysis, where two spheres with radii R_1 and R_2 are in contact with applied force F as shown in Figure D-1.

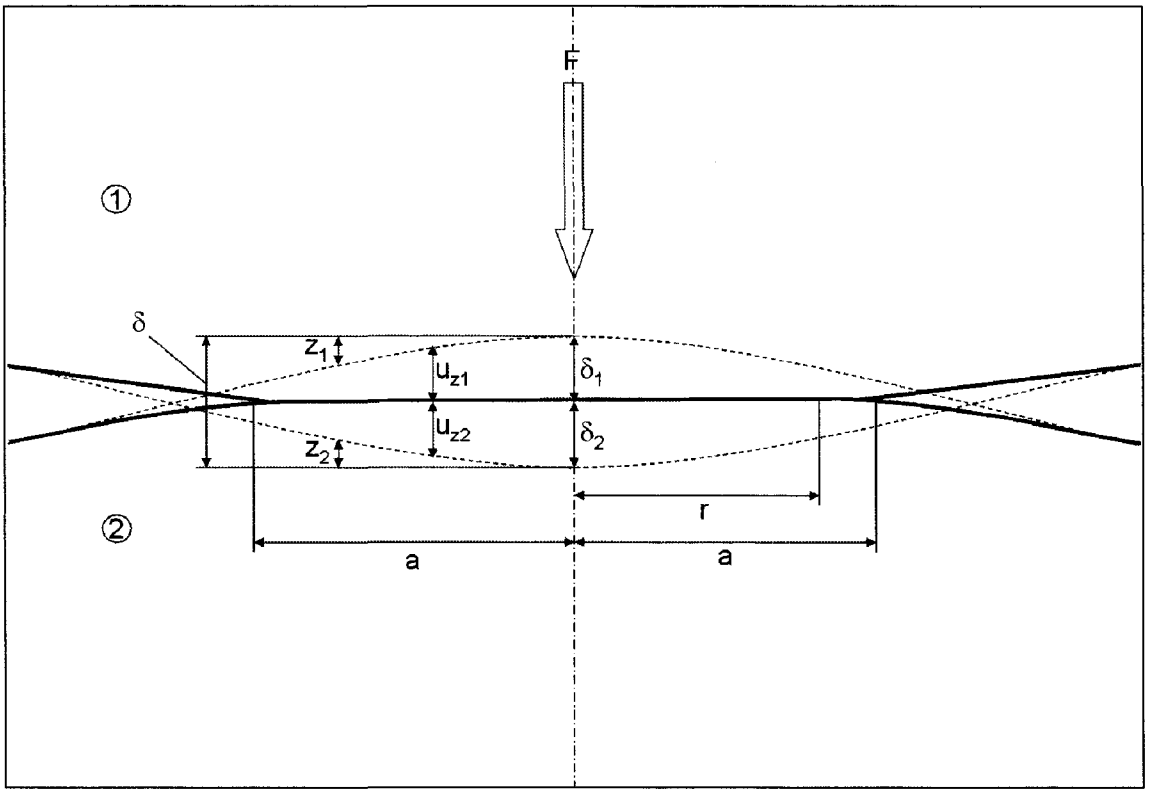

Figure D-1: Schematics of two frictionless spherical solids in contact [63]

The circular contact area between the two spheres has a radius "a" and the contact pressure $p(r)$ is elliptical at radius "r".

$$p(r) = p_{max}\left[1-(r/a)^2\right]^{1/2} \qquad \text{D-1}$$

The pressure is obtained from the force "F", pressure relationship

$$F = \int_0^a p(r).2\pi r dr = \frac{2}{3} p_{max} \pi a^2 \qquad \text{D-2}$$

Therefore, the maximum hertzian pressure is defined as

$$p_{max} = \frac{3F}{2\pi a^2} \quad \text{D-3}$$

Where a can be derived form the elastic deformation, where the displacement is defined as shown in figure

$$u_{z1} + u_{z2} = \delta - z_1 - z_2 = \delta - \frac{r^2}{2R} \quad \text{D-4}$$

The displacement of each sphere can be described by

$$u_n = \frac{1-\nu^2}{E} . \frac{\pi p_{max}}{4a} . (2a^2 - r^2) \quad \text{D-5}$$

Therefore substituting equation D. 5 into D. 4 and solving for the contact radius "a"

$$a = \frac{\pi p_{max} R}{2E^*} \quad \text{D-6}$$

Where R and E^* is the effective curvature and effective modulus respectively

$$\frac{1}{R} = \frac{1}{R_1} + \frac{1}{R_2} \quad \text{D-7}$$

$$\frac{1}{E^*} = \frac{1-\nu_1^2}{E_1} + \frac{1-\nu_2^2}{E_2} \quad \text{D-8}$$

REFERENCES

[1] M. Murakawa, S. Takeuchi "Evaluation of tribological properties of DLC films used in sheet forming of aluminum sheet" Surface and Coating Technology 163-164, 2003, 561-565.

[2] H. Fukuia, J. Okidaa, N. Omoria, H. Moriguchib, K. Tsuda "Cutting performance of DLC coated tools in dry machining aluminum alloys" Surface and Coating Technology 187, 2004, 70-76.

[3] A. Erdemir and C. Donnet, "Tribology of diamond-like carbon films: recent progress and future prospects" Journal of Physics D: Applied Physics 39, 2006, R311-R327.

[4] F. Gao, A. Erdemir and W.T. Tysoe "The tribological properties of low-friction hydrogenated diamond-like carbon measured in ultra high vacuum" Tribology letters 20, 2005, 221-227.

[5] A. Erdemir "Genesis of super low friction and wear in diamond like carbon films" Tribology International 37, 2004, 1005-1012.

[6] R. Hauert, "An overview on the tribological behaviour of diamond-like carbon in technical and medical applications" Tribology International 37, 2004, 991-1003.

[7] E. Konca, Y.T. Chang, Weiner Dasch, A.T. Alpas "Vacuum tribological behavior of the non-hydrogenated diamond like carbon coatings against aluminum: Effect of running-in in ambient air" Wear 259, 2005, 795-799.

[8] E. Liu, Y.F. Ding, L. Li, B. Blanpain, J.P. Celis, "Influence of humidity on the friction of diamond and diamond-like carbon materials" Tibology International 40, 2007, 216-219.

[9] Y. Yun, D.B. Bogy, C.S. Bhatia "Tribochemical study of hydrogenated carbon coatings with different hydrogen content levels in ultra high vacuum" Journal of Tribology 119, 1997, 437-442.

[10] B.J. Hamrock, S.R. Schmid and B.O. Jacobson "Fundamentals of Fluid Film Lubrication" CRC Press, Second Edition, 2004, 4-10.

[11] J. Robertson "Diamond-like amorphous carbon" Materials Science and Engineering 37, 2002, 129-281.

[12] B.E. Mellor "Surface coatings for protection against wear" Woodhead Publishing Limited, Cambridge England, 2006, 88-161.

[13] D.G. Teer "Magnetron Sputter Ion Plating" US patent 5556519, 1996.

[14] Q. Wei, R.J. Narayan, A.K. Sharma, J. Sankar, J. Narayan "Preperaion and mechanical properties of composite diamond-like carbon thin films" J. Vac. Sci. Technol. 17, No. 6, 1999, 3406-3414.

[15] S.B. Iyer, K.S. Harshavardhan, V. Kumar "Buckeling patterns in diamond-like carbon films" Thin Solid Films 256, 1995, 94-100.

[16] M. Ban, T. Hasegawa "Internal stress reduction by incorporation of silicon in diamond-like carbon films" Surface and Coating Technology 162, 2002, 1-5.

[17] P. Wang, X. Wang, T. Xu, W. Liu, j. Zhang "Comparing internal stress in diamond-like carbon films with different structure" Thin Solid Films 515 2007, 6899-6903.

[18] C.L. Chen and D.Y. Hong "Interfacial studies for improving the adhesion of diamond-like carbon films on steel" Applied Surface Science 243, 2005, 296-303.

[19] S. Zhang, X.L. Bui, Y. Fu, B.L Butler, H. Du "Bias-graded deposition of diamond-like carbon for tribological applications" Diamond and Related Materials 13, 2004, 867-871.

[20] W. Zhang, A. Tanaka "Tribological properties of DLC films deposited under various conditions using a plasma-enhanced CVD" Tribology International 37, 2004, 975-982.

[21] C. Donnet and A. Grill "Friction control of diamond-like carbon coatings" Surface and Coatings Technology 94-95, 1997, 456-462.

[22] A. Erdemir "The role of hydrogen in tribological properties of diamond-like carbon films" Surface and Coating Technology 146-147, 2001, 292-297.

[23] C. Donnet "Recent progress on the Tribology of doped diamond-like and carbon alloy coatings: a review" Surface and Coatings Technology 100-101, 1998, 180-186.

[24] (Eds.) C. Donnet and A. Erdemir "Tribology of Diamond-like Carbon Films: Fundamentals and Applications" Springer 2008, 313-331.

[25] J. Fontaine, M. Belin, T. LeMogne, A. Grill "How to restore superlow friction of DLC: the healing effect of hydrogen gas", Tribology International 37, 2004, 867-877.

[26] E. Konca, Y.T. Cheng, A.M. Weiner, J. Dasch and A.T. Alpas "The role of hydrogen atmosphere on the tribological behavior of non-hydrogenated DLC coatings against Aluminum", Tribology Transactions, 50, 2007, 178-186.

[27] C. Donnet, T. Mogne, L. Ponsonnet, M. Belina, A. Grill, Patel and Jahnes "The respective role of oxygen and water vapor on the tribology of hydrogenated diamond-like carbon coatings" Tribology Letters 4, 1998, 259-265.

[28] E. Konca, Y.T. Cheng, A.M. Weiner, J. Dasch and A.T. Alpas, "Effect of test atmosphere on the tribological behavior of the non-hydrogenated diamond-like carbon coatings against 319 aluminum alloy and tungsten carbide", Surface and Coatings Technology 200, 2005, 1783-1791.

[29] Y. Qi, E. Konca, A.T. Alpas "Atmospheric effects on the adhesion and friction between non-hydrogenated diamond-like carbon (DLC) coating and aluminum-A first principle investigation" Surface Science 600, 2006, 2955-2965.

[30] Y. Qi and L.G. Hector Jr. "Adhesion and adhesive transfer at aluminum/diamond interfaces: A first principles study" Physical Review B 69, 2004, 235401.

[31] E. Konca, Y.T. Chang, A.T. Alpas "Dry sliding behaviour of non-hydrogenated DLC coating against Al, Cu and Ti in ambient air and argon" Diamond and related materials 15, 2006, 939-943.

[32] H. Ronkainen, S. Varjus, K. Holmberg "Friction and wear properties in dry, water- and oil-lubricated DLC against alumina and DLC against steel" Wear 222, 1998, 120-128.

[33] M.I. Bouchet "Boundary Lubrication mechanisms of carbon coatings by MoDTC and ZDDP addetives" Tribology International 38, 2005, 257-264.

[34] M. Kalin, J. Vizintin "Differences in the tribological mechanisms when using non-doped, metal-doped (Ti, WC) and non-metal-doped (Si) diamond-like carbon against steel under boundary lubrication, with and without oil additives" Thin Solid Films 515, 2006, 2734-2747.

[35] M. Kalin "A comparison of the tribological behavior of steel/steel, Steel/DLC and DLC/DLC contacts when lubricated with mineral and biodegradable oils" Wear 261, 2006, 22-31.

[36] S.K. Field, M. Jarratt, D.G. Teer "Tribological properties of graphite-like and diamond like carbon coatings" Tribology International 37, 2004, 949-956.

[37] A.L. Kearney ASM Handbook V2 "Properties of Cast Aluminum Alloys" 10th edition ASM international Materials Park, OH, 1992, 597.

[38] D.M. Stefanescu ASM Handbook V1 "Properties and selection: Irons, Steels and high performance alloys" 10th edition ASM international Materials Park, OH, 1992, 255, 1166.

[39] W.C. Oliver and G.M. Parr "An improved technique for determining hardness and elastic modulus using load and displacement sensing indentation experiments", J. Mater. Res. 7, 1992, 1564-1583.

[40] J. Tirira, P. Trocellier "Elastic Recoil Detection Analysis" Journal of Raioanalytical and Nuclear Chemistry 130 No. 2, 1989, 311-319.

[41] B.C. Smith "Fundamentals of Fourier Transform Infrared Spectroscopy" CRC Press, 1996, 15-31.

[42] Z. Alfassi, M. Peisach, A. Alfassi "Elemental analysis by particle accelerators" CRC Press, 1991, 244-245.

[43] Veeco Metrology group "Wyko NT 1100 setup guide", Veeco Instruments Inc., 2002, 1-2.

[44] P.H. Dawson "Quadrouple mass spectrometer and its applications" Springer, 1995, 49-52.

[45] ExxonMobil Lubricants & Specialties "Moil 1 Synthetic ATF", Exxon Mobil Corporation 2007.

[46] E. Konca, Y.T. Cheng, A.M. Weiner, J. Dasch, A.T. Alpas " Elevated temperature tribological behaviour of non-hydrogenated diamond-like carbon coatings against 319 aluminum alloy" Surface and Coating Technology 200, 2006, 3996-4005.

[47] Y. Gogotsi, A. Kailer and K.G. Nickel "Pressure-induced phase transformations in diamond" Journal of Applied Physics 84, 1998, 1299-1304.

[48] Y. Liu, E.I. Meletis "Evidence of graphitization of diamond-like carbon films during sliding wear" Journal of Material Science 32, 1997, 3491-3495.

[49] R.H. Savage "Graphite Lubrication" Journal of Applied Physics 19, Number 1, 1947, 1-10.

[50] A. Perstin and M. Grunze "Water as a lubricant for graphite: A computer simulation study" The Journal of Chemical Physics 125, 2006, 114707.

[51] C. Donnet, J. Fontain, A. Grill and T.L. Mogne "The role of hydrogen on the friction mechanism of diamond-like carbon films" Tribology Letters 9, 2000, No. 3-4, 137-142.

[52] M.N. Gardos "Synthetic Diamond: Emerging CVD Science and Technology", Edited by K. E. Spear and J. Dismukes, Wiley, New York, 1994, 484.

[53] B.K. Yen "Influence COF water vapour and oxygen on the Tribology of carbon materials with sp2 valence configuration" Wear 192, 1996, 208-215.

[54] B.J. Hamrock, Schmid, Jacobson "Fundamentals of fluid film lubrication" CRC Press 2nd edition, 2004, 9.

[55] P.J. Blau "On the nature of running-in" Tribology International 38, 2005, 1007-1012.

[56] J. Xu, K. Kato, T. Hirayama, "The transition of wear mode during the running-in process of silicon nitride sliding in water" Wear 205, 1997, 55-63.

[57] I.C. Faraon, D.J. Schipper "Stribeck curve for starved line contacts" Journal of Tribology 129, 2007, 181-187.

[58] B.J. Hamrock, D. Dowson, "Ball Bearing Lubrication: The Elastohydrodynamics of Elliptical Contacts" John Wiley & Sons, Inc., New York 1981, 207.

[59] S. Tung "Automotive Tribology overview of current advances and challenges for the future" Tribology International 37, 2004, 517-536.

[60] S.M. Hsu, R.S. Gates "Boundary lubricating films: formation and lubrication mechanism" Tribology International 38, 2005, 305-312.

[61] A.G. Papay "Oil Soluble Friction Reducers- Theory & Application" Lubrication Engineering 1983, 419-426.

[62] B.N.J. Persson "Sliding Friction physical Principles and Applications" Springer 1998, 148-150.

[63] K.L. Johnson "Contact Mechanics" Cambridge university Press 1987, 88-93.

VITA AUCTORIS

Name	Ahmed AbouGharam
Place of birth	Cairo, Egypt
Year of birth	1985
Education	Bachelor of Engineering (B. E), Material Science McMaster University, Hamilton, Ontario, Canada 2002-2006
	Masters of Applied Science (M. A. Sc), Engineering Materials University of Windsor, Windsor, Ontario, Canada 2006-2008
Conference Presentation	Society of Tribologists & Lubrication Engineers (STLE) Cleveland, OH, USA May 18-22, 2008